

EUROPEAN ORGANIZATION FOR NUCLEAR RESEARCH

European Laboratory for Particle Physics

CERN - SL DIVISION

CERN SL/96-70 (BI)

**Luminosity and beta function measurement
at the electron-positron collider ring LEP**
Doctoral Thesis

P. Castro-Garcia,
CERN, Geneva, Switzerland

Abstract

The optimization of luminosity needs a fast signal which is provided with the measurement of the rate of small angle Bhabba scattered e^+ and e^- . It is shown that, despite the excess of background particles received at the detectors, luminosity measurements are possible by using appropriate techniques. The results presented include examples of luminosity optimization with the adjustment of the vertical beam separation at interaction points. The correlation between changes in measured beam sizes and changes in luminosity is shown.

In the second part, a new method to obtain precise optics measurements is presented. The procedure to measure the phase advance using 1000-turn orbit measurements of a horizontally or vertically excited beam is described. Beta, alpha and phase advance functions can be obtained exclusively from the phase advances at beam position monitors. This method has been used to measure optics imperfections at LEP. Results of these experiments are compared with simulation results using MAD Measurements of chromaticity and impedance distributions are also reported.

Geneva, Switzerland
November 25, 1996

List of symbols used in this thesis

α	fine structure constant.
α_c	momentum compaction factor.
α_x, α_y	horizontal and vertical alpha functions.
β_x, β_y	horizontal and vertical beta functions.
c	speed of light in vacuum.
C	circumference of the storage ring or closed orbit length.
D_x, D_y	horizontal and vertical dispersion functions.
e	electron charge magnitude.
E	particle (or beam) energy.
$\varepsilon_x, \varepsilon_y$	horizontal and vertical beam emittances.
f_{rev}	revolution frequency.
f_{RF}	electromagnetic field frequency of radio-frequency cavities.
I	beam intensity or beam current.
I_b	bunch intensity.
k_b	number of bunches per beam.
\mathcal{L}	luminosity of the collision between two beams.
m_e	electron mass.
m_{ij}	matrix elements (i: indicates row, j: indicates column).
M	transport matrix.
μ_x, μ_y	horizontal and vertical phase functions.
ξ_x, ξ_y	horizontal and vertical beam-beam tune shift.
p	particle (or beam) momentum.
Q_x, Q_y	horizontal and vertical tunes.
Q'_x, Q'_y	horizontal and vertical chromaticity values.
r_e	classical electron radius.
s	longitudinal coordinate.
X	detector's inner edge horizontal position.
X_{col}	collimator horizontal position.
σ_x, σ_y	horizontal and vertical beam sizes.
x, y	horizontal and vertical coordinates.
x', y'	horizontal and vertical trajectory angles with respect to the s axis.
θ, ϕ	polar angle and azimuthal angle in spherical coordinates.
ϕ_{12}	phase advance from point 1 to point 2.
Ω	solid angle.

The $*$ symbol associated to a beam parameter (σ_x^*, β_x^*) refers to its value at the interaction point.

Contents

Introduction	4
1 Introduction to LEP	6
1.1 CERN: The european laboratory for particle physics	6
1.1.1 The LEP collider	7
1.2 Definition of luminosity	8
1.3 Luminosity and beam size monitoring	10
2 Some fundamental concepts in accelerator physics	12
2.1 Linear beam dynamics	12
2.1.1 Transport matrices	13
2.1.2 Twiss functions	15
3 LEP luminosity monitors	18
3.1 Luminosity measurement method	18
3.2 Detector acceptance for Bhabha scattering	22
3.3 Particle background at the detectors	29
3.4 Results	35
3.4.1 Detector efficiency	35
3.4.2 Detector acceptance measurement as a function of collimator position	38
3.4.3 Measurement of the luminosity statistical error	41
3.4.4 Vernier scan	42
3.4.5 Luminosity acquisition time	45
3.4.6 Radiation damage on silicon detectors	46
4 Phase and beta function measurement	49
4.1 Phase measurement at beam position monitors	49
4.2 Measurement of the Twiss functions	51
4.3 Measurement of the phase and the amplitude of betatron oscillations	54
4.4 Error analysis of phase measurements	58
4.5 Beta function measurement error	65
4.6 Experimental observation of beta-beating at LEP	75
4.6.1 Measurement of beta-beating due to a quadrupole field error	75
4.6.2 Effect of QS0 calibration on vertical beta-beating	75
4.6.3 Sources of opposite beta-beating for e^+ and e^- beams	78
4.7 Measurement of the chromaticity distribution at LEP	84
4.8 Measurement of the impedance distribution at LEP	85

5	Luminosity and beam size measurements at LEP	89
5.1	How does beta-beating affect beam size measurements?	89
5.2	Comparison between luminosity from LEP monitors and from BEUV emittances	91
	Conclusions	93
	Appendices	95
A	Overlap of two Gaussian distributions	95
B	Integral of the Bhabha scattering cross section over a rectangular detector	98
C	Transformation of β and α using the phase advance ϕ_{12}	100
D	Measured alpha function at beam position monitors	102
E	Harmonic analysis of beam oscillations	104
F	Corrections of the phase measured at beam position monitors	107
	Bibliography	109
	Acknowledgements	113

Introduction

At the Large Electron-Positron collider LEP [1], electron and positron beams with an energy of 45.6 GeV collide to produce Z particles, the neutral carriers of the weak force. The Z particle has a very short lifetime and decays into other particles which are detected and identified at the four LEP experiments. The analysis of these "events" provides a measurement of the Z mass and width and of coupling constants of the Standard Model. In the next phase of LEP (LEP 2), beams will be accelerated to an energy of about 90 GeV allowing the creation of pairs of W^\pm particles, the charged partners of the Z particle.

In order to minimize the statistical error on the Z mass and width, a large amount of Z particles has to be produced. The production rate of Z particles is equal to the product of the luminosity of the collision between the electron and the positron beam and the cross section for Z production in e^+e^- collisions. High luminosity is therefore required, not only for the production of Z particles but also for the creation of other particles (like $B\bar{B}$ meson pairs), for the search of new particles, etc.

After some years of operating the LEP collider, the initial luminosity of $4 \cdot 10^{30} \text{ cm}^{-2}\text{s}^{-1}$ obtained in 1989 has been increased to more than $20 \cdot 10^{30} \text{ cm}^{-2}\text{s}^{-1}$ in 1994. A considerable effort is put into the study of different accelerator physics issues in order to understand the actual luminosity limitations and to optimize the performance of the collider. These studies require adequate instruments to measure beam currents, tunes, closed orbit, beam sizes and luminosity.

In this thesis, two techniques for beam measurements at LEP were investigated:

- **Luminosity measurement:** Optimization of luminosity needs a fast signal which is provided with the measurement of small angle Bhabha scattered e^+e^- pairs in detectors installed at 8.3 m at both sides from each interaction point. The rate of Bhabha scattering (of about 60 Hz assuming a luminosity of $10^{31} \text{ cm}^{-2}\text{s}^{-1}$) is directly proportional to the luminosity and allows a measurement within a few seconds with a 5% error. The rate of background particles exceeds the Bhabha rate by two or three orders of magnitude. However, it is shown in this thesis that luminosity measurements are still possible by using appropriate techniques, e.g. calculating the probability of accidental background coincidences. The results presented include examples of luminosity optimization with the adjustment of the vertical beam separation at the interaction point, at LEP usually called Vernier scan.
- **Phase and beta functions measurement:** The properties of the focusing structure of colliders and transport lines are described and calculated using the Twiss functions: beta function, its derivative and phase. The horizontal and the vertical beta functions determine the transverse beam sizes that change around the storage ring. In general, all dynamic beam parameters like dynamic aperture, stability thresholds, closed orbit, luminosity, emittance, etc. depend on the beta and the phase functions. At the design

stage of a storage ring, the Twiss functions are obtained from magnetic fields, position and geometry of the components of the accelerator using simulation programs like MAD (Methodical Accelerator Design) [2]. In a real accelerator, longitudinal misalignment, quadrupole gradient errors and other effects change the Twiss functions. In this thesis, it is shown how precise measurements of the Twiss functions are obtained by exciting coherent betatron oscillations on the beam and sampling these oscillations at the beam position monitors for 1000 turns. This method has been used to measure the beta function change due to quadrupole gradient errors, beam separation schemes and energy loss by synchrotron radiation. Results of these experiments are compared with the beta function obtained using the program MAD. The error of phase measurements has been studied in detail and its contribution to the beta function is calculated and measured. An important result that followed from this study is the measurement of chromaticity distribution [3] and impedance distributions [4]. This was done for the first time ever in an accelerator by measuring the phase function with beams of different energy and current. The results helped to check the chromaticity correction and to identify the sources of impedance in LEP.

Accurate beta function measurements obtained with this method have been used to cross-check measurements by different beam profile monitors installed at LEP [5, 6]. A very good correlation has been found [7] between relative beam size changes observed at the beam profile monitors during physics data taking and changes in the luminosity measured with the LEP luminosity monitors. Based on these two facts, an attempt is made to match the luminosity measurements and luminosity given by

$$\mathcal{L} = \frac{I_{e^+} I_{e^-}}{4\pi e^2 k_b f_{rev} \sigma_x^* \sigma_y^*} \quad (0.1)$$

where I_{e^+} and I_{e^-} are the positron and electron beam currents, e is the electron charge, k_b is the number of bunches per beam, f_{rev} the revolution frequency and the beam sizes σ_x^* and σ_y^* at the interaction point are given by

$$\sigma_x^* = \sqrt{\frac{\beta_x^*}{\beta_x}} \sigma_x \quad \sigma_y^* = \sqrt{\frac{\beta_y^*}{\beta_y}} \sigma_y$$

where σ_x and σ_y are the beam sizes measured with beam profile monitors (assuming zero dispersion), β_x^* and β_y^* are the values of the horizontal and vertical beta functions at the interaction point and β_x and β_y are the values of the horizontal and vertical beta functions at the measurement point of the beam size.

Chapter 1 introduces the LEP storage ring, includes the definition of luminosity and discusses the beam-beam interaction as the fundamental limit of the luminosity and the techniques used at LEP to further increase the luminosity. The introduction to basic concepts of accelerator physics required for this thesis (like the equation of motion of charged particles in linear magnetic fields, transport matrices and Twiss functions) is given in chapter 2. The LEP luminosity monitoring system is described and results are shown in chapter 3. The method to measure the phase of betatron oscillations at beam position monitors in order to obtain the phase and the beta functions is presented in chapter 4. In chapter 5, the correlation between the luminosity measured with LEP monitors and the luminosity calculated from measured beam intensities and beam sizes using the luminosity expression of eq. (0.1) is shown. Finally, the conclusions are presented.

Chapter 1

Introduction to LEP

In the search of new particles at higher energies, colliders are the most efficient way of using the kinetic energy of accelerated particles to create new particles and reactions. While in fixed target experiments the collision energy is proportional to \sqrt{E} (with E being the beam energy), in head-on collisions of two beams with equal energy the total energy of the two particles in the center of mass (c.m.) system is equal to the sum of the energies of each particle

$$E_{cm} = 2 E \quad .$$

However, due to the low particle density of the beams with respect to the particle densities in fixed targets, the number of particle reactions in beam-beam collisions is enormously reduced. While the typical distance between particles (or atoms) in solids or liquids is between 0.1 and 0.3 nm and in gases is 3.5 nm at 760 torr and 24°C, the density of particles in a beam is much lower. For instance the distance between protons in the Super Proton Synchrotron [8] beam at 315 GeV is in the order of 600 nm and between electrons in the LEP beam at 45.6 GeV is 200 nm at the collision points. It is therefore important to optimize the design and the operation of colliders to obtain the maximum rate of reactions.

In this chapter, CERN and LEP are introduced. The definition of luminosity is given and the beam-beam effect is discussed as the most important limitation of luminosity in a storage ring. Luminosity, beam size and beta function monitoring are also introduced.

1.1 CERN: The european laboratory for particle physics

CERN is one of the largest scientific research centers in the world. It is located at the border between France and Switzerland, near the city of Geneva. CERN was founded in 1954 and its name CERN comes from the French "Conseil Européen pour la Recherche Nucléaire".

CERN has currently 19 European member states although many institutes from other countries collaborate in the physics experiments.

The purpose of CERN is to provide the organization and infrastructure needed to build and operate large particle accelerators and installations for high energy experiments. It serves the scientific community in a large variety of interest, which requires new technologies and developments in materials, electronics, computing, communication, etc.

CERN has an advanced and versatile complex of particle accelerators, forming a chain towards higher beam energies. A typical example of this is the injection chain of positrons and electrons into LEP. LEP is the world largest particle accelerator with its circumference of 26.7 km. It is located inside of a tunnel excavated at an average depth of 100 m in the

area between the Geneva lake and the Jura mountains. At LEP, beams of electrons and positrons circulate in opposite directions at the speed of light for many hours. They collide at four points where the particle detectors of the collaborations L3, ALEPH, OPAL and DELPHI are located.

The machine is operated at center-of-mass energies around the mass of the Z particle (about 91.2 GeV). The particles created at the decay of Z particles are analyzed at the particle detectors, providing precise measurements of the Standard Model. In the second phase of LEP, beams will be accelerated at twice this energy in order to produce pairs of W^\pm particles, the partners of the Z particle in the electro-weak interaction.

1.1.1 The LEP collider

LEP is a synchrotron storage ring operating with beams of electrons and positrons in the same vacuum chamber. LEP was designed to operate with four equidistant bunches per beam. These bunches cross at eight interaction points indicated in fig. 1.1.

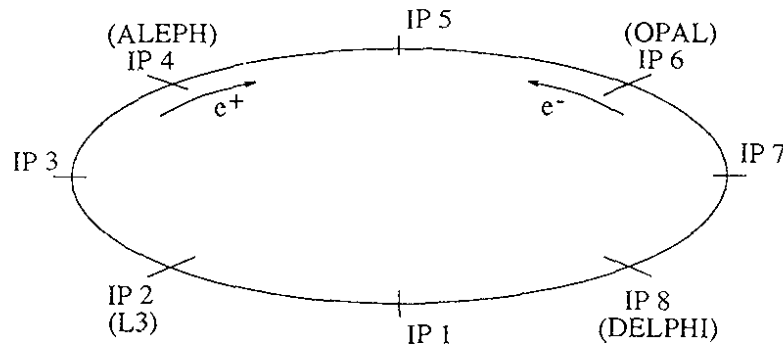


Figure 1.1: Interaction points for 4×4 equidistant bunches (IP: interaction point). The experiments L3, ALEPH, OPAL and DELPHI are located at the even interaction points.

The machine has eight straight sections and eight arcs. The straight sections, with about 500 m length, are located around the interaction points. The magnetic guiding structure at the even straight sections 2, 4, 6 and 8 are designed to focus the beams at the interaction points in order to increase the probability of collisions between electrons and positrons.

The acceleration is provided by radio-frequency cavities located around interaction points 2 and 6. They provide the energy needed to maintain electrons and positrons circulating since these particles emit synchrotron radiation along their curved trajectories. The particle energy loss per revolution U_o depends on the radius of its trajectory ρ and on its energy E [9]:

$$U_o = C_\gamma \frac{E^4}{\rho} \quad (1.1)$$

where

$$C_\gamma = \frac{4\pi}{3} \frac{r_e}{E_o^3} = 8.85 \cdot 10^{-5} \text{ m GeV}^{-3} ,$$

r_e is the classical electron radius and E_o is the electron mass at rest. For LEP, with a radius of curvature of 3096 m in the dipole magnets, this yields 125 MeV per turn for a particle of 45.6 GeV. This energy loss has to be replaced constantly by the accelerating cavities.

1.2 Definition of luminosity

Luminosity \mathcal{L} relates the event rate \dot{N} of a given process to its cross section σ

$$\dot{N} = \frac{dN}{dt} = \mathcal{L} \sigma \quad .$$

Typical numbers for luminosity at LEP are around $10^{31} \text{ cm}^{-2}\text{s}^{-1}$ per interaction point, which produced a total integrated luminosity ($\int \mathcal{L} dt$) of 64.4 pb^{-1} in 1994, or equivalent, 2.5 millions of Z particles¹ in all four LEP experiments together.

The luminosity of head-on collisions between two beams can be calculated [11, 12] from the convolution of the transverse particle distribution of each beam integrated over the collision transverse surface A

$$\mathcal{L} = \int_A N_{e+} \rho_{e+} N_{e-} \rho_{e-} da$$

where $N_{e\pm}$ is the number of particles per beam, $\rho_{e\pm}$ is the transverse particle distribution over the area A and da is the differential of area.

The transverse particle distributions depend on the longitudinal position and have a minimum at the interaction point. The length of the interaction region should be therefore taken into account in the above integral. The length of the interaction region is determined by the longitudinal particle distribution, which at LEP is about one centimeter and its effect on the luminosity is negligible.

Colliders present an important disadvantage due to the low density of particles with respect to the density of particles of the target in fixed target accelerators. To compensate for the low particle density of colliding beams, particles circulate around a storage ring for many hours (10 to 20 hours at LEP) and collide with the revolution frequency. Particles circulating in a storage ring are confined in a very reduced space using quadrupole and sextupole magnets in a special arrangement, called *magnetic lattice* (including dipole magnets). In this magnetic focusing system, the sizes of the transverse particle distribution change along the longitudinal position since the guide fields vary from place to place.

In electron machines the sizes of the equilibrium particle distribution are determined by the effect of synchrotron radiation which excites betatron oscillations and the effect of oscillation damping by the longitudinal acceleration provided by radio-frequency cavities. Both effects lead to a stationary Gaussian particle distribution. At LEP, as in most storage rings, the motion of particles in the horizontal and in the vertical planes is quasi-independent². The transverse particle density distribution function ρ can therefore be expressed as

$$\rho(x, y) = g(x) g(y)$$

where g is a Gaussian function with different widths for each plane. The luminosity of a collider ring is then given by

$$\mathcal{L} = k_b f_{rev} \int_{-\infty}^{\infty} \int_{-\infty}^{\infty} N_{e+} g_{e+}(x) g_{e+}(y) N_{e-} g_{e-}(x) g_{e-}(y) dx dy$$

where k_b is the number of bunches per beam, f_{rev} is the revolution frequency and N_{e+} , N_{e-} are the number of particles per bunch of positrons and electrons, respectively. The solution

¹The cross section for the production of Z particles at the energy of its resonance is about 41.5 nb [10].

²There is a certain degree of coupling between the horizontal and the vertical planes, which is often neglected in first approximation. At LEP, it is about 1% after correction of the coupling fields.

of this integral (see Appendix A) leads to the following expression for luminosity

$$\mathcal{L} = \frac{k_b f_{rev} N_{e+} N_{e-}}{2\pi \sqrt{(\sigma_{x_{e+}}^{*2} + \sigma_{x_{e-}}^{*2})(\sigma_{y_{e+}}^{*2} + \sigma_{y_{e-}}^{*2})}} ,$$

where σ_x^* and σ_y^* are the widths of the Gaussian distributions representing the r.m.s. beam sizes at the collision points [13]. The number of particles N is often expressed as the flux of electric charge or current I circulating in the ring per second:

$$I = Ne f_{rev}$$

where e is the electron charge. The luminosity can then be written as

$$\mathcal{L} = \frac{k_b I_{e+} I_{e-}}{2\pi e^2 f_{rev} \sqrt{(\sigma_{x_{e+}}^{*2} + \sigma_{x_{e-}}^{*2})(\sigma_{y_{e+}}^{*2} + \sigma_{y_{e-}}^{*2})}} \quad (1.2)$$

where I_{e+} and I_{e-} are the positron and the electron bunch currents. For equal electron and positron beam sizes, eq. (1.2) becomes

$$\mathcal{L} = \frac{k_b I_{e+} I_{e-}}{4\pi e^2 f_{rev} \sigma_x^* \sigma_y^*} .$$

Beam-beam interaction as a fundamental limit of luminosity in collider rings

It is not possible to increase the luminosity in a collider ring up to any desired value by simply increasing the intensity of the bunches or by reducing the beam sizes (as eq. (1.2) suggests), because the beam stability is limited by the electromagnetic interaction between the colliding beams, called *beam-beam* interaction [14]. The electromagnetic field of one beam disturbs the motion of particles of the opposite beam and can lead to the blow-up of the transverse beam size, causing significant luminosity decrease and beam current losses.

The beam-beam interaction depends on the number of particles N per beam, the transverse beam sizes at the interaction point σ_x^* , σ_y^* and the relativistic Lorentz factor $\gamma = E/m_e c^2$. The beam-beam interaction is parametrized in terms of the beam-beam tune shift ξ [15]

$$\xi_x = \frac{Nr_e \beta_x^*}{2\pi \gamma \sigma_x^* (\sigma_x^* + \sigma_y^*)} , \quad \xi_y = \frac{Nr_e \beta_y^*}{2\pi \gamma \sigma_y^* (\sigma_x^* + \sigma_y^*)} \quad (1.3)$$

where β_x^* and β_y^* are the values of the horizontal and vertical beta functions and $r_e = e^2/4\pi\epsilon_0 m_e c^2 = 2.818 \cdot 10^{-15}$ m is the classical electron radius.

For given values of β_x^* , β_y^* , σ_x^* and σ_y^* , there is a certain beam intensity threshold given by the maximum beam-beam tune shift. For higher intensities, the beam blows up and its lifetime is reduced. At LEP the maximum beam-beam tune shift found experimentally is $\xi \simeq 0.03-0.04$.

Due to emission of synchrotron radiation, the horizontal beam size in e^+e^- storage rings is much larger than the vertical beam size. To obtain the maximum horizontal and vertical beam-beam tune shifts ξ_x and ξ_y , the difference between vertical and horizontal beam sizes is compensated by a β_x^* larger than the β_y^* , which is done at the design stage and later optimized empirically [16]. For example, at LEP σ_y^* is about 50 times smaller than σ_x^* , $\beta_x^* = 2.5$ m and $\beta_y^* = 5$ cm.

At LEP there are two general strategies to reach higher luminosity. The first procedure uses wiggler magnets to increase the horizontal beam size. Higher beam currents and higher

luminosities can be reached by increasing the horizontal beam size to keep ξ_y constant in eq. (1.3). In this case, the luminosity grows linearly as the bunch current increases. At LEP, the bunch intensity is limited to about 500 μA at injection energies (20 GeV) by the transverse mode coupling instability [17, 18].

The second strategy is to increase the number of bunches per beam. LEP was designed to operate with four bunches of electrons and four bunches of positrons (equidistant) with eight crossing points numbered from 1 to 8 as shown in fig. 1.1. The four against four (4×4) bunches collide at even interaction points (2,4,6,8) where the LEP experiments are installed. To reduce the beam-beam interaction beams are vertically separated with high voltage electrostatic plates at odd interaction points (1,3,5,7). In 1993, the number of bunches per beam was increased from four to eight with the *pretzel* scheme [19]. Eight (equidistant) bunches of electrons encounter eight bunches of positrons in 16 interaction points, eight of which are located in the middle of arcs. Beams are separated in the horizontal plane with electrostatic separators located at both sides of straight sections 2, 4, 6 and 8 (see fig 1.2).

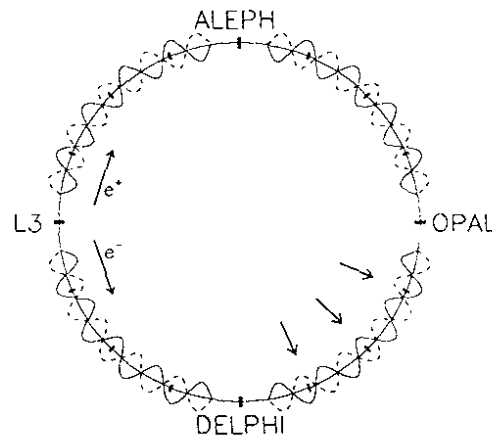


Figure 1.2: Schematic representation of the pretzel separation between the electron (dashed line) and the positron (full line) beams. The arrows indicate the unwanted collision points.

More recently, in 1995, a new scheme allows to inject up to 16 bunches per beam. This scheme, called *bunch trains* [20], replaces each of the initial four bunches by four "trains" of two, three or four bunches. The longitudinal distance between bunches in a train is $d = 74.1$ m (247 ns). Vertical electrostatic fields separate bunches at $d/2$, d and $3d/2$ from both sides of the interaction point (see fig. 1.3) to avoid parasitic collisions.

1.3 Luminosity and beam size monitoring

The operation of LEP requires very precise and reliable beam instrumentation and monitoring. Intensity monitors, beam profile cameras, tune meters, beam position monitors and luminosity detectors are the most important instruments to optimize and increase luminosity.

Luminosity is monitored by scaling the rate of Bhabha scattered e^+e^- pairs. The cross section of Bhabha scattering is well known and can be calculated precisely from QED theory. LEP luminosity detectors measure Bhabha scattering at very small scattering angles in order to provide a fast signal directly proportional to the luminosity at each interaction point.

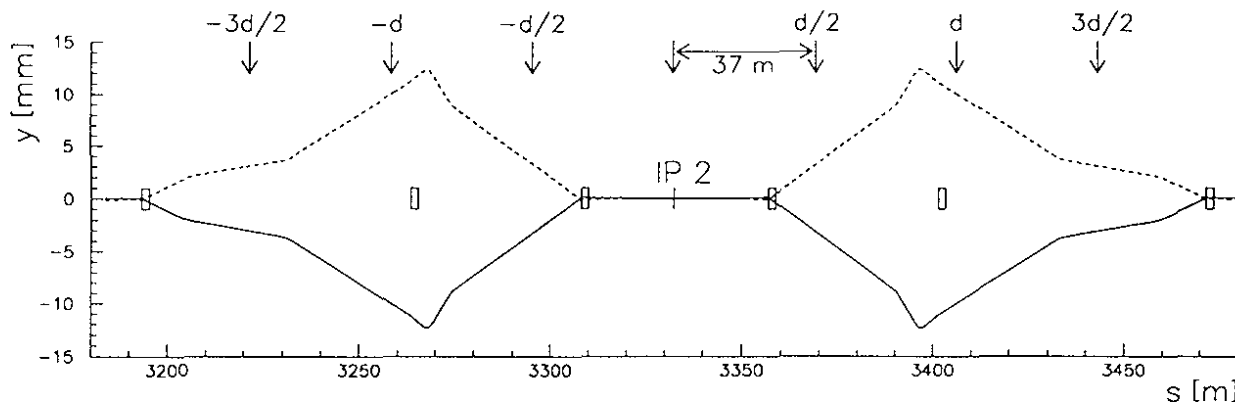


Figure 1.3: Vertical orbit separation around interaction point 2 between the electron (dashed line) and the positron (full line) beams used for the bunch train scheme. The boxes denote electrostatic separators. The arrows indicate the crossing points between bunches.

Luminosity optimization: Vernier scan

To collide the beams head-on, the vertical position of the electron and positron beams must be controlled with high precision since the vertical beam sizes are of the order of a few micrometers at collision points.

Vertical miscrossings of the two beams can be due to errors on the vertical electrostatic field used to separate the positron and the electron beams at odd interaction points (1,3,5,7). These errors can create a small difference in the vertical orbit of the two beams that propagates to the even points (2,4,6,8). Moreover, the electron and positron beams have a different horizontal orbit due to the opposite variation of energies around the ring (*sawtooth effect*). As a consequence, each beam sees a small difference in the focusing fields of sextupoles which together with field imperfections, positioning errors of magnets and non-linearities in quadrupole fields (which have to be considered in a real collider) also cause a difference between the electron and the positron vertical beam orbits.

It is therefore necessary to correct the voltage of electrostatic separators in order to optimize the beam overlap at the interaction points with the so-called *Vernier scans*. This procedure consists of measuring luminosity with respect to the change of electrostatic separation to find the zero separation which gives the maximum luminosity. Vernier scans are frequently done at LEP and need precise luminosity measurements made in a short interval of time. The luminosity is measured with the LEP monitors installed at the four interaction points and the Vernier scan procedure is described in section 3.4.4.

Vertical beam size

In an ideal machine the vertical beam size can be kept very low, being limited only by the beam-beam interaction. This is not true for a real machine with magnetic field errors. In this case the vertical beam size depends on the coupling of the horizontal betatron oscillations into the vertical plane and on linear as well as nonlinear imperfections around the machine. The vertical beam size is sensitive to small changes of various parameters like tunes and closed orbit. Vertical closed orbit displacements introduce vertical dispersion, which is a strong source for the increase of the vertical beam size.

Control and minimization of these effects have to be studied to improve the performance of the collider. Monitoring of vertical beam size and luminosity are needed.

Chapter 2

Some fundamental concepts in accelerator physics

In the previous chapter, the beam parameters related to the luminosity were introduced. In this thesis, more specific concepts of particle accelerators are used, which deserve a little introduction for a reader not familiar with them. The equation of motion of a charged particle in magnetic fields, the matrix notation and the Twiss functions are now introduced.

2.1 Linear beam dynamics

The basic elements of a storage ring are dipole and quadrupole magnets. Dipole magnets bend the trajectory of particles horizontally into a circular path. The horizontal force F (orthogonal to the trajectory of a particle with charge e and momentum $p = \gamma m_o v$) is provided by the vertical magnetic field B_y of dipoles

$$F = evB_y = \gamma m_o v^2 / \rho$$

which bends its trajectory into an arc of radius ρ

$$\rho = \frac{p}{eB_y} \quad . \quad (2.1)$$

Quadrupole magnets focus particles to confine their trajectories in a reduced space inside the vacuum chamber of the accelerator. The magnetic field of a quadrupole is characterized by its gradient g

$$g = \frac{\partial B_y}{\partial x} = \frac{\partial B_x}{\partial y}$$

where B_x and B_y are the field components in the horizontal and the vertical planes.

Other magnetic elements of higher order fields are used in particle accelerators. For example, at LEP sextupole magnets are used to correct chromatic effects of quadrupoles on particles with small energy differences. Their effect on the beam dynamics is considered as perturbations to the motion in linear magnetic field approximation. From now on, only linear terms are considered in the dynamics of beam particles.

In the design of a storage ring, magnetic elements are placed along the reference orbit. The coordinate system used to describe the motion of beam particles lies on the reference orbit and moves together with the ideal particle with nominal momentum (in the direction

of positrons for LEP), as it is shown in fig. 2.1. The position of the ideal particle is described with the longitudinal variable s . The horizontal axis x is defined towards outside the circumference and the vertical axis y is defined upwards.

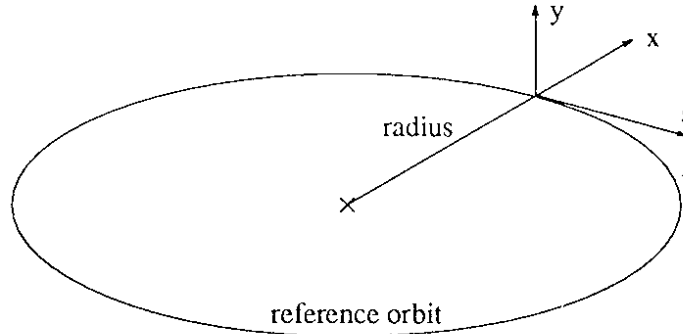


Figure 2.1: Coordinate system of the reference orbit.

LEP presents a regular structure of alternating quadrupoles and dipoles along the arcs. These magnets are arranged in consecutive units or cells called FODO cells. Each of these units consists of a horizontally focusing quadrupole followed by a dipole, then by a horizontally defocusing quadrupole and another dipole. Other magnets like sextupoles and orbit corrector dipoles are included in the FODO cell.

Equation of motion

The motion of particles in a storage ring is described by Hill's differential equation

$$\frac{d^2 u}{ds^2} + k(s)u = 0 \quad . \quad (2.2)$$

where the variable u represents the transverse coordinates x and y . The function $k(s)$ is periodic with the circumference C of the storage ring ($k(s+C) = k(s)$). In a quadrupole field with gradient g , the field *strength* $k(s)$ is given by

$$\begin{aligned} k &= \frac{eg}{p} && \text{for the horizontal plane} \\ k &= -\frac{eg}{p} && \text{for the vertical plane} \end{aligned}$$

and in a dipole field of bending radius ρ given by eq. (2.1), $k(s)$ is given by

$$\begin{aligned} k &= \frac{1}{\rho^2} && \text{for the horizontal plane} \\ k &= 0 && \text{for the vertical plane.} \end{aligned}$$

2.1.1 Transport matrices

As in light optics, a particle trajectory can be described in terms of a matrix in the phase space [9]. Thus, the position of a particle at the longitudinal position s_2 can be calculated as a function of its position at s_1 using a transport matrix:

$$\begin{pmatrix} u_2 \\ u'_2 \end{pmatrix} = \begin{pmatrix} m_{11} & m_{12} \\ m_{21} & m_{22} \end{pmatrix} \begin{pmatrix} u_1 \\ u'_1 \end{pmatrix} \quad (2.3)$$

where u is the particle transverse displacement from the reference orbit and $u' = du/ds$ is the angle between its trajectory and the reference orbit.

A beam transport line or a storage ring can be divided into a sequence of regions (magnets and free spaces) where the magnetic field is constant in the longitudinal direction s . In each of these regions $k(s)$ is constant and eq. (2.2) is the differential equation of a harmonic oscillator, whose solution is given bellow.

Drift space

In a *drift space* or field free region, the particle follows a straight line and the solution of eq. (2.2) for $k = 0$ is

$$\begin{aligned} u(s) &= u_o + (s - s_o) u'_o \\ u'(s) &= u'_o \end{aligned}$$

where u_o is the position and u'_o is the angle of the particle at the beginning of the field free region. A drift space section of length L is represented by the following matrix

$$M_d = \begin{pmatrix} 1 & L \\ 0 & 1 \end{pmatrix}$$

Dipole and quadrupole magnets

In a region where there is a magnetic field, k is not zero and the solution of eq. (2.2) depends on the sign of k . For a dipole, $k = 1/\rho^2$ is positive in the horizontal plane and zero in the vertical plane, where the solution of eq. (2.2) is identical to the drift space case. The value of k in a quadrupole magnet has the same sign as the gradient g in the horizontal plane and opposite sign in the vertical plane.

For $k > 0$, the quadrupole magnetic field is *focusing* and the trajectory of a particle is given by

$$u(s) = \cos [\sqrt{k}(s - s_o)] u_o + \frac{1}{\sqrt{k}} \sin [\sqrt{k}(s - s_o)] u'_o$$

The transport matrix of a focusing field region of length L is

$$M_{QF} = \begin{pmatrix} \cos \xi & \frac{1}{\sqrt{k}} \sin \xi \\ -\sqrt{k} \sin \xi & \cos \xi \end{pmatrix}$$

where $\xi = \sqrt{k} L$.

If $k < 0$, the quadrupole is *defocusing* and the trajectory of a particle is given by

$$u(s) = \cosh [\sqrt{|k|}(s - s_o)] u_o + \frac{1}{\sqrt{|k|}} \sinh [\sqrt{|k|}(s - s_o)] u'_o$$

The transport matrix of a defocusing field region of length L is

$$M_{QD} = \begin{pmatrix} \cosh \xi & \frac{1}{\sqrt{|k|}} \sinh \xi \\ \sqrt{|k|} \sinh \xi & \cosh \xi \end{pmatrix}$$

where $\xi = \sqrt{|k|} L$.

All these transport matrices shown above satisfy the general condition that their determinants are equal to one.

2.1.2 Twiss functions

A solution which satisfies eq. (2.2) is of the form

$$u(s) = a\sqrt{\beta(s)} \cos[\mu(s) + \psi] , \quad (2.4)$$

where β and μ are periodic functions with periodicity C , while a and ψ are constants depending on initial conditions. The function β is called *beta function* or amplitude function and μ is called *phase function* or betatron phase which is related to the beta function by

$$\mu(s_2) - \mu(s_1) = \int_{s_1}^{s_2} \frac{1}{\beta(s)} ds .$$

The integral around the ring (i.e. $s_2 = s_1 + C$) is $2\pi Q$, where Q is the *tune* or number of betatron oscillations per revolution.

The beta function, the phase function and the *alpha function*, which is defined as the derivative

$$\alpha(s) = -\frac{1}{2} \frac{d\beta(s)}{ds} ,$$

are called the *Twiss functions*.

While the equation of motion (eq. 2.2) and the transport matrices given above describe the movement of a single particle, the Twiss functions are more suitable to describe the dynamics of the large number of particles which form the beam. For instance, the square root of the beta function is directly proportional to the beam size σ

$$\sqrt{\beta\varepsilon} = \sigma \quad (2.5)$$

where ε is a constant called *emittance*. The phase advance, i.e. the difference of the phase function between two points s_1 and s_2 , is the change of the oscillation phase of particles. Finally, the sign of the alpha function at a certain point in the ring gives information whether the trajectories of particles are convergent (+ sign) or divergent (− sign).

Twiss functions and magnetic layout

The transport matrix of eq. (2.3) can be expressed as [21]:

$$M = \begin{pmatrix} \sqrt{\frac{\beta_2}{\beta_1}}(\cos \phi_{12} + \alpha_1 \sin \phi_{12}) & \sqrt{\beta_1 \beta_2} \sin \phi_{12} \\ \frac{\alpha_1 - \alpha_2}{\sqrt{\beta_1 \beta_2}} \cos \phi_{12} - \frac{1 + \alpha_1 \alpha_2}{\sqrt{\beta_1 \beta_2}} \sin \phi_{12} & \sqrt{\frac{\beta_1}{\beta_2}}(\cos \phi_{12} - \alpha_2 \sin \phi_{12}) \end{pmatrix} \quad (2.6)$$

where $\beta_1 = \beta(s_1)$, $\beta_2 = \beta(s_2)$, $\alpha_1 = \alpha(s_1)$, $\alpha_2 = \alpha(s_2)$ and ϕ_{12} is the phase difference between s_1 and s_2 , ($\phi_{12} = \mu(s_2) - \mu(s_1)$). This matrix M is obtained by multiplying successively the transport matrices for each existing element (drift space or quadrupole) between s_1 and s_2 . The ratio between matrix elements of the first row is

$$\frac{m_{11}}{m_{12}} = \frac{1}{\beta_1}(\cot \phi_{12} + \alpha_1) \quad (2.7)$$

and the ratio between matrix elements of the second column is

$$\frac{m_{22}}{m_{12}} = \frac{1}{\beta_2}(\cot \phi_{12} - \alpha_2) . \quad (2.8)$$

These expressions show the relationship between the Twiss parameters β and α at s_1 (or at s_2) and the phase difference ϕ_{12} between s_1 and s_2

$$\tan \phi_{12} = \frac{m_{12}}{m_{11}\beta_1 - m_{12}\alpha_1} = \frac{m_{12}}{m_{22}\beta_2 + m_{12}\alpha_2} .$$

The expressions given above will be used in section 4.2 to calculate the beta function from the measured phase function.

Twiss functions transformation

The transformation of the Twiss parameters β , $\alpha = -\frac{1}{2} \frac{d\beta}{ds}$ and $\gamma = \frac{1 + \alpha^2}{\beta}$ from s_1 to s_2 is given by [22]

$$\begin{pmatrix} \beta_2 \\ \alpha_2 \\ \gamma_2 \end{pmatrix} = \begin{pmatrix} m_{11}^2 & -2m_{11}m_{12} & m_{12}^2 \\ -m_{11}m_{21} & 1 + 2m_{12}m_{21} & -m_{12}m_{22} \\ m_{21}^2 & -2m_{21}m_{22} & m_{22}^2 \end{pmatrix} \begin{pmatrix} \beta_1 \\ \alpha_1 \\ \gamma_1 \end{pmatrix} \quad (2.9)$$

where m_{ij} are the coefficients of the matrix in eq. (2.6). The phase function at s_2 is obtained from eq. (2.7)

$$\mu_2 = \mu_1 + \phi_{12} = \mu_1 + \arctan \left(\frac{1}{\beta_1 m_{11}/m_{12} - \alpha_1} \right) . \quad (2.10)$$

An alternative way to obtain β_2 is with the square of the second element m_{12} of the matrix shown in eq. (2.6):

$$\beta_2 = \frac{m_{12}^2}{\beta_1 \sin^2 \phi_{12}} \quad (2.11)$$

where ϕ_{12} is taken from eq. (2.10). The value α at s_2 can be obtained using eq. (2.8)

$$\alpha_2 = \cot \phi_{12} - \beta_2 \frac{m_{22}}{m_{12}} \quad (2.12)$$

where β_2 is taken from eq. (2.11). The equivalence between the matrix in eq. (2.9) and eqs. (2.11) and (2.12) is shown in appendix C. These expressions will be used in chapter 4 to reconstruct $\beta(s)$ and $\phi(s)$ from the measured values of β and ϕ at the beam position monitors.

Beta function measurement using quadrupoles

The vertical beta function at even interaction points (2,4,6,8) is determined by a measurement of the vertical tune shift due to the change of the field strength of superconducting quadrupoles QS0. These quadrupoles are located at 4.76 m from the interaction point and focus the beams at interaction points 2,4,6 and 8.

The tune shift ΔQ due to a small change Δk in the strength of a quadrupole of length L is given by

$$\Delta Q \simeq \frac{1}{4\pi} \int_L \beta(s) \Delta k ds \simeq \frac{\beta_Q \Delta k L}{4\pi} \quad (2.13)$$

where β_Q is the average value of the beta function at the quadrupole. This result was obtained by Courant and Snyder [21] and allows the measurement of the function β at a single quadrupole by varying its strength and measuring the tune shift.

If the optics is symmetric at the interaction point, the alpha function $\alpha = -(1/2)(d\beta/ds)$ is zero at the interaction point and the beta function in the drift space between the two superconducting quadrupoles can be calculated using eq. (2.9)

$$\begin{pmatrix} \beta \\ \alpha \\ \gamma \end{pmatrix} = \begin{pmatrix} 1 & -2l & l^2 \\ 0 & 1 & -l \\ 0 & 0 & 1 \end{pmatrix} \begin{pmatrix} \beta^* \\ 0 \\ 1/\beta^* \end{pmatrix}$$

where β^* is the value of the beta function at the interaction point and l is the distance from the interaction point. In this drift space β follows the equation of a parabola centered at the interaction point. From the value of β at the two superconducting quadrupoles

$$\beta_Q = \beta^* + \frac{l^2}{\beta^*} \simeq \frac{l^2}{\beta^*} ,$$

we can extract the value of the beta function at the interaction point

$$\beta^* = \frac{l^2}{\beta_Q} .$$

Perturbation of the beta function due to a quadrupole gradient error

An additional quadrupole strength Δk also changes the Twiss functions around the storage ring. For a quadrupole magnet of length L located at the longitudinal position s_o , where the beta function is β_o and the phase function is μ_o , the beta function in the ring changes by [23]

$$\frac{\Delta\beta}{\beta}(s) = \frac{\Delta k L \beta_o \cos(2\pi Q - 2|\mu(s) - \mu_o|)}{2 \sin(2\pi Q)} \quad (2.14)$$

This equation represents a modulation of the beta function that propagates around the ring with twice the betatron frequency.

Beta function monitoring

For precise beam size measurements a good understanding of the beam instrumentation and also the knowledge of the beta function at the measurement points are needed. At LEP the beta function can change by $\pm 10-15\%$ with respect to the theoretical values due to errors in the magnetic field of quadrupoles. In the pretzel scheme, the separation of electron and positron beams increases this mismatch by another $\pm 20-30\%$. A precise measurement of the actual beta function is necessary to avoid systematic errors in the beam size measurement.

The measurement of other optical functions such as chromaticity (change of tunes versus particle energy) and dispersion (single particle orbit dependence on particle energy) and the distribution of impedance (electric field of the walls of the vacuum chamber as seen by the beam) provide a good understanding of the effect of magnetic imperfections on the optics of beams.

Chapter 3

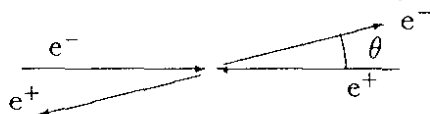
LEP luminosity monitors

The goal of the LEP luminosity monitors is to provide an accurate measurement of the luminosity at all four interaction points in a short interval of time. Small size compact silicon-tungsten calorimeters are installed inside the vacuum chamber at about 8.3 m away from both sides of the four interaction points. They measure the rate of Bhabha scattering of e^+e^- pairs for scattering angles between 2 and 5 mrad. These detectors measure Bhabha pairs at a rate of ~ 60 Hz for a luminosity of $10^{31} \text{ cm}^{-2}\text{s}^{-1}$, providing a statistically accurate measurement of luminosity in a few seconds.

The detector is described in section 3.1, and its acceptance is calculated in section 3.2. The source of particle background, its reduction using collimators and the correction to the Bhabha rate are presented in section 3.3. Section 3.4 includes calibration of signal thresholds, measured acceptance, examples of Vernier scans, acquisition time for various particle background levels and radiation dose measured at silicon detectors.

3.1 Luminosity measurement method

LEP luminosity monitors measure the rate of elastic scattering between highly relativistic positrons and electrons, known as Bhabha scattering [24].



The Bhabha scattering cross section for a scattering angle θ less than 50 mrad is dominated by the Coulomb contribution [25] and can be approximated by

$$\frac{d\sigma}{d\Omega} = \left(\frac{\alpha}{4E}\right)^2 \left[\frac{3 + \cos^2 \theta}{1 - \cos \theta}\right]^2 \quad (3.1)$$

where E is the beam energy and α is the fine structure constant

$$\alpha = \frac{e^2}{4\pi\epsilon_0\hbar c} = \frac{1}{137.036} .$$

For small scattering angles $\cos \theta$ can be approximated by $1 - \theta^2/2$, and eq. (3.1) can be written

$$\frac{d\sigma}{d\Omega} \simeq \frac{4\alpha^2}{E^2\theta^4} . \quad (3.2)$$

This cross section increases rapidly as the scattering angle θ gets smaller.

Detectors layout

To measure the high flux of Bhabha scattered e^+e^- pairs at very small scattering angles the detectors are housed inside horizontal collimators placed inside the vacuum chamber 8.3 m away from both sides of each interaction point (with the exception of interaction point 2, where the collimators on the right side are at a distance of 8.4 m and on the left side are at 8.2 m from the interaction point). As part of these collimators, the detectors can be moved very close to the circulating beam, intercepting Bhabha e^+e^- pairs scattered at angles between 2 and 5 mrad. The setup is shown schematically in fig. 3.1.

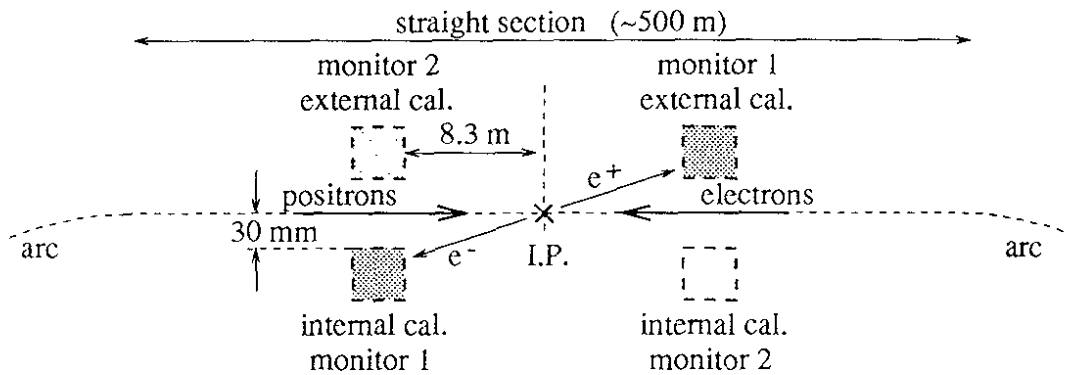


Figure 3.1: Top view (not to scale) of four detectors installed at interaction points 2, 4, 6 and 8. (I.P.: interaction point, cal.:calorimeter.)

To discriminate the signal of Bhabha scattering from background particles, each luminosity monitor consists of two calorimeters located at opposite sides of the interaction point, one internal and one external to the orbit in the horizontal plane. Monitor 1 detects coincidences of e^+e^- pairs with the positron outside and the electron inside as it is shown in fig. 3.1, and monitor 2 detects e^+e^- pairs with the positron inside and the electron outside.

Bhabha scattering calorimeters

The detectors used for luminosity monitoring are similar to the silicon calorimeters used for the polarimeter and have been developed in the Beam Instrumentation Group [26]. These calorimeters are made of tungsten and thin layers of silicon semiconductors. The distribution of silicon detector planes in the calorimeter is shown in fig. 3.2, where the longitudinal scale is given in radiation lengths of tungsten. The radiation length is defined as the mean distance over which a high energy electron (or positron) loses part of its energy by bremsstrahlung, remaining with $1/e$ of its initial energy. It is estimated to be [27]

$$L_{\text{rad}} = \frac{716.4 \text{ gcm}^{-2} A}{\rho Z (Z + 1) \ln(287/\sqrt{Z})}$$

where A is the atomic weight, Z is the atomic number and ρ is the material density. The radiation length for tungsten is 3.5 mm.

A high energy electron penetrating into tungsten radiates a number of photons by bremsstrahlung. These photons create in tungsten e^+e^- pairs which can radiate more photons initiating an electromagnetic cascade. The number of e^+e^- pairs in the cascade increases exponentially, until electron energies fall below the energy at which losses by ionization and

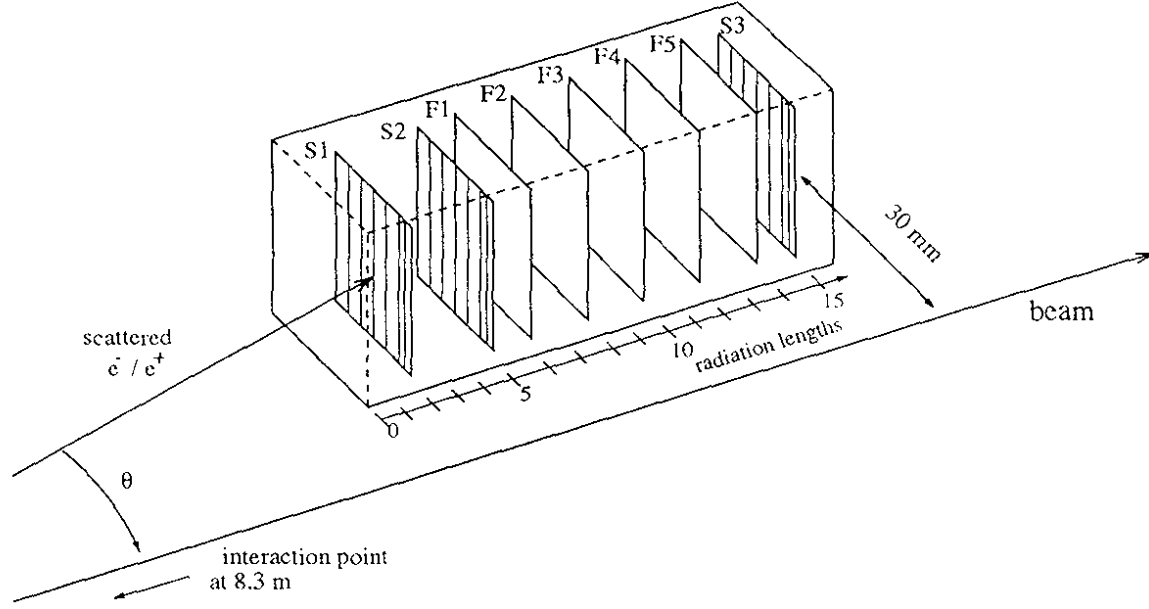


Figure 3.2: Strip (S) and full area (F) silicon detectors in the Bhabha scattering calorimeter.

by bremsstrahlung are equal, known as the *critical energy* E_c given by [28]

$$E_c = \frac{800 \text{ MeV}}{Z + 1.2} .$$

In tungsten E_c is about 10.6 MeV. Below this value, electrons dissipate their energy by ionization and excitation rather than by bremsstrahlung. The average longitudinal energy deposition in the electromagnetic cascade is described by [29]

$$\frac{dE}{dt} = E_o \frac{b^a t^{a-1} e^{-bt}}{\Gamma(a)}$$

where E_o is the incident electron energy, t is the depth from the calorimeter surface in radiation lengths and Γ is the gamma function. a and b are taken from a parametrization of test results for electrons from 5 to 92 GeV on iron and lead [30]:

$$\begin{aligned} a &= 2.284 + 0.7136 \log(E_o) \\ b &= 0.5607 + 0.0093 \log(E_o) . \end{aligned}$$

The longitudinal profile of the energy deposited in the Bhabha scattering calorimeter by the electromagnetic cascade developed by an electron of 45.6 GeV is shown in fig. 3.3.

There are two types of silicon detectors in the Bhabha scattering calorimeter: strip detectors (S) and full area detectors (F). Strip detectors have a $40 \times 40 \text{ mm}^2$ area which is divided into 16 vertical strips, 8 strips of 1 mm width in the area close to the beam followed by 8 strips of 4 mm width. They allow the determination of the cascade position in the calorimeter. Full area detectors are made of a continuous area of silicon of $50 \times 50 \text{ mm}^2$. They can measure the energy of an incident particle by sampling the energy deposition of the electromagnetic cascade.

During the commissioning of these calorimeters [31] a careful study was made on the energy and the collinearity of e^+e^- pairs [32]. This study has shown a position dispersion of about $\sigma_x = 2 \text{ mm}$ between the positron and the electron at the detector plane, due to the

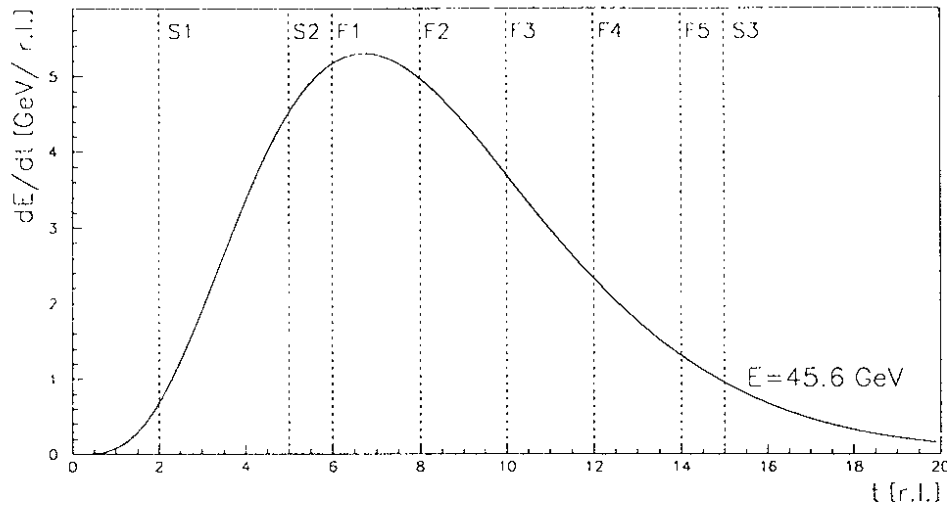


Figure 3.3: Longitudinal profile of the energy deposition in the electromagnetic cascade developed by an electron of 45.6 GeV incident in the Bhabha scattering calorimeter. (r.l.: radiation lengths, S: strip detectors, F: full area detectors.)

beam divergence at the interaction point. This effect makes the discrimination of Bhabha scattering from background signals using collinearity cuts difficult. It was therefore decided to use the sum signal from the strip detector S2, which provides the best signal-to-noise ratio, to count the coincidences from both calorimeters and to subtract the delayed coincidence rate to the e^+e^- pairs signals to obtain the Bhabha scattering rate. Later, the delayed background coincidence measurement was replaced by the statistical evaluation from the background rate received at each calorimeter (described in section 3.3).

Data acquisition

When electrons and positrons of the electromagnetic cascade created in tungsten blocks enter the silicon detectors they liberate electron-hole pairs which are swept out by the applied electric field (reversed bias voltage). The pulse of charge collected by the silicon detector is amplified and transmitted through 50–60 m of cables to the data acquisition electronics located in a shielded gallery protected from synchrotron radiation. The signal is integrated for 150 ns by an Integrate and Hold module. The output is digitized by a 12-bit Analog-Digital Conversion (ADC) module in 4.5 μ s. Digital signals from external and internal calorimeters are processed in the Digital Signal Processor (DSP) for every bunch crossing. The DSP controls the ADC module (both produced by CES [33]) and is a software programmable device which can be used as a preprocessor (for data reduction) and memory buffer [34] between the ADC and an external microprocessor.

The DSP program compares the signals from S2 detectors of external and internal calorimeters to threshold values which discriminate the electronic noise. If the signals from both external and internal calorimeters are above thresholds the counter for *pairs* N_{pair} is incremented by one. If only the signal from the external detector is higher than the threshold, the counter for *externals* N_{ext} is increased by one. If, instead, only the internal signal is higher than the threshold, the counter for *internals* N_{int} is increased by one. In order to take into account different bunch intensities, there are a set of N_{ext} , N_{int} and N_{pair} counters for each bunch. After an acquisition of three seconds, the values of N_{ext} , N_{int} and N_{pair} are transferred to a buffer memory where they can be read by the local microprocessor, while these counters are set to zero to start a new acquisition.

3.2 Detector acceptance for Bhabha scattering

The rate \dot{N} of Bhabha scattered e^+e^- pairs hitting a pair of detectors is a function of luminosity \mathcal{L} and the acceptance of the detector. It is calculated by integrating eq. (3.2)

$$\dot{N} \simeq \mathcal{L} \frac{4\alpha^2}{E^2} \int_{\Delta\Omega} \frac{d\Omega}{\theta^4} , \quad (3.3)$$

where $\Delta\Omega$ is the solid angle of the detector. The differential solid angle $d\Omega$ can be written in terms of spherical coordinates θ and ϕ

$$d\Omega = \sin \theta \, d\theta \, d\phi \simeq \theta \, d\theta \, d\phi ,$$

which is valid for small θ .

Since the surface of the detector is a square, it is more convenient to use Cartesian coordinates x, y to solve the integral over the detector area. The angles θ and ϕ are expressed in terms of angular coordinates x' and y' (see fig. 3.4)

$$\theta = +\sqrt{x'^2 + y'^2} , \quad \phi = \arctan \frac{y'}{x'} .$$

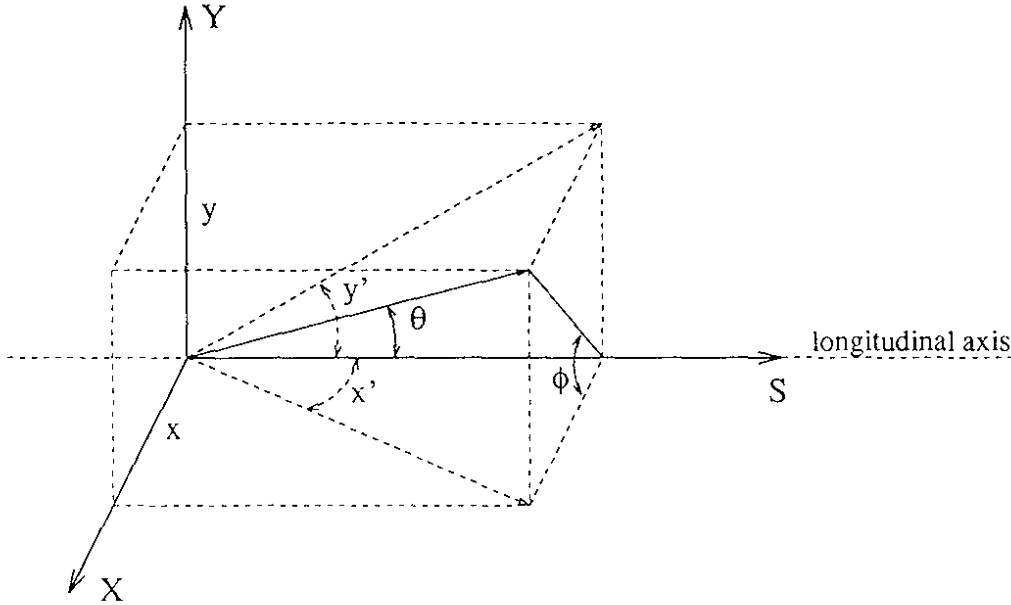


Figure 3.4: Transformation between spherical coordinates and x' and y' angular coordinates.

The differential ($d\theta \, d\phi$) is transformed by using the Jacobian determinant

$$d\theta \, d\phi = \frac{\partial(\theta, \phi)}{\partial(x', y')} \, dx' \, dy' = \begin{vmatrix} \frac{\partial\theta}{\partial x'} & \frac{\partial\phi}{\partial x'} \\ \frac{\partial\theta}{\partial y'} & \frac{\partial\phi}{\partial y'} \end{vmatrix} \, dx' \, dy' = \frac{dx' \, dy'}{\sqrt{x'^2 + y'^2}} .$$

Eq. (3.3) becomes a double integral along the horizontal angle x' and the vertical angle y'

$$\dot{N} \simeq \mathcal{L} \frac{4\alpha^2}{E^2} \int_{x'} \int_{y'} \frac{dx' \, dy'}{(x'^2 + y'^2)^2} , \quad (3.4)$$

where the integration domain is defined by the detector area and position.

The trajectories of Bhabha scattered e^+e^- pairs from the interaction point to the detectors are modified by the magnetic field of superconducting quadrupoles of 2 m length located at 4.70 m from the interaction point (except at interaction point 6, where these quadrupoles are at 4.89 m). The transverse positions x, y of a particle at the detector can be calculated as a function of the angles x', y' of its trajectory at the interaction point using the transport matrices M from the interaction point to the detector

$$M = M_{L2} \times M_{Qs0} \times M_{L1}$$

where M_{Qs0} is the transport matrix through the superconducting quadrupole and M_{L1} and M_{L2} are the transport matrices through the drifts spaces from the interaction point to this quadrupole and from the quadrupole to the detector. Let A and B be the matrix element m_{12} of the matrix M for the horizontal and the vertical planes, respectively, then

$$x = A x' \quad \text{and} \quad y = B y' .$$

A and B are the effective lengths and their values in table 3.1 are calculated for the value of k_{Qs0} used in the optics of 1993 (g05p46h), where $\beta_x^* = 2.5$ m and $\beta_y^* = 5$ cm. For the optics used in 1994 (k05p46v3), where $\beta_x^* = 2.0$ m, the lengths A and B remain the same within 1%.

	$k_{Qs0} \text{ (m}^{-2}\text{)}$	$A \text{ [m]}$	$B \text{ [m]}$
left IP2	-0.1649	14.00	3.32
right IP2	-0.1649	14.54	3.34
IP4	-0.1644	14.25	3.30
IP6	-0.1600	14.00	3.48
IP8	-0.1644	14.25	3.30

Table 3.1: Horizontal A and vertical B effective lengths of luminosity calorimeters from the interaction point.

The sensitive surface of the detector is the silicon semiconductor with a square area with size $L = 40$ mm. The detector is centered in the horizontal plane of the beam and its closest edge to the beam is at a distance $X = 35$ mm approximately. The detector location in the transverse plane as it is seen from the interaction point is shown in fig. 3.5.

The integration domain of eq. (3.4) for the angle x' is between the horizontal limits of the detector

$$x'_1 = \frac{X}{A} \quad \text{and} \quad x'_2 = \frac{X+L}{A} \quad (3.5)$$

and for the angle y' is between

$$y'_1 = -\frac{L}{2B} \quad \text{and} \quad y'_2 = \frac{L}{2B} . \quad (3.6)$$

The analytical solution of the integral in eq. (3.4) (described in the appendix B) is

$$\dot{N} = \mathcal{L} \frac{\alpha^2}{E^2} \left[\left[-\frac{1}{x'y'} - \left(\frac{1}{x'^2} - \frac{1}{y'^2} \right) \arctan \frac{y'}{x'} \right]_{y'_1}^{y'_2} \right]_{x'_1}^{x'_2}$$

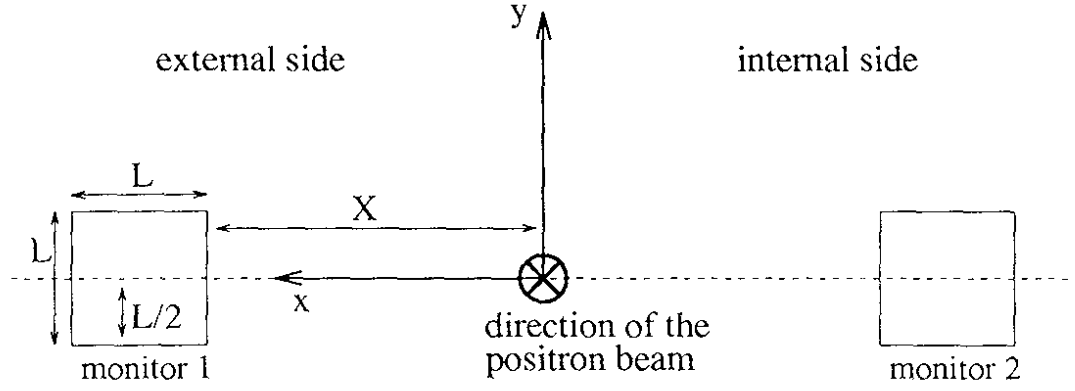


Figure 3.5: Detector area seen from the interaction point.

Replacing the integration limits we obtain \dot{N} as a function of X and \mathcal{L}

$$\begin{aligned} \dot{N} = \mathcal{L} \frac{4\alpha^2}{E^2} & \left[\frac{AB}{(X+L)X} + \left(\frac{A^2}{2X^2} - \frac{2B^2}{L^2} \right) \arctan \frac{AL}{2BX} \right. \\ & \left. - \left(\frac{A^2}{2(X+L)^2} - \frac{2B^2}{L^2} \right) \arctan \frac{AL}{2B(X+L)} \right] \end{aligned} \quad (3.7)$$

The counting rate of Bhabha scattering at a detector placed at 8.3 m with $A = 14.25$ m, $B = 3.30$ m and $L = 40$ mm is shown in fig. 3.6 as a function of the horizontal distance X from the beam, for a typical luminosity of $10^{31} \text{ cm}^{-2}\text{s}^{-1}$ and a beam energy $E = 45.6$ GeV. The rapid increase of \dot{N} for smaller X is due to the strong dependence of the Bhabha scattering cross section on the scattering angle θ (see eq. (3.2)). The typical range for X is from 33 to 37 mm, which corresponds to $\dot{N} = 44.2$ and 33.5 Hz, respectively.

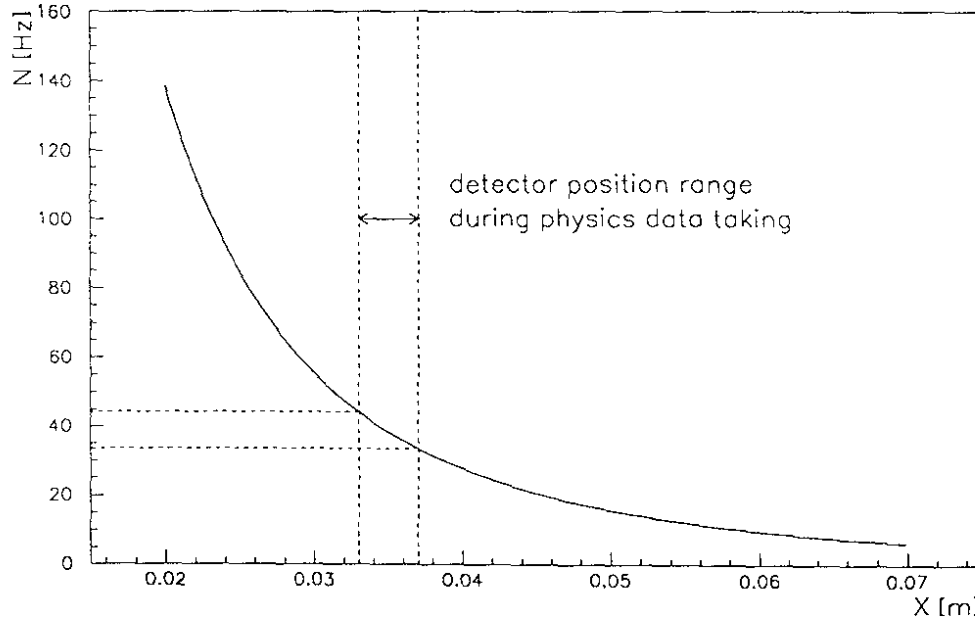


Figure 3.6: Calculated Bhabha scattering rate detected with calorimeters of area $40 \times 40 \text{ mm}^2$ as a function of its horizontal distance X from the edge of the detector to the beam, for $\mathcal{L} = 10^{31} \text{ cm}^{-2}\text{s}^{-1}$ and $E = 45.6$ GeV.

Beam angle and divergence at the interaction point

The Bhabha scattering rate obtained in eq. (3.7) is calculated assuming a dimensionless, centered ($x = y = 0$) beam, where particles have parallel trajectories ($x' = y' = 0$).

Horizontal closed orbit changes in the collider can affect the beam angle at the interaction point and therefore the detector rate. An angle of ± 0.1 mrad at the interaction point represents a relative position change of ± 1.4 mm and a $\Delta \dot{N}/\dot{N} \simeq \pm 10\%$ in a single monitor (two opposite detectors) at $X = 30$ mm. This effect is compensated at first order by averaging the two monitors.

The beam size and beam divergence, i.e. the position and the angular spread of the particles in the beam, are given by the emittance ϵ and the value of β

$$\sigma_u = \sqrt{\beta_u \epsilon_u} \quad , \quad \sigma_{u'} = \sqrt{\frac{\epsilon_u}{\beta_u}} \quad , \quad u = x, y \quad .$$

The horizontal emittance ϵ_x is increased by emittance wiggler magnets in order to limit the beam-beam force in the interaction between the two beams (see section 1.2). Depending on the emittance wiggler field strength the horizontal emittance ranges from 15 to 45 nm for the k05p46v3 optics [35]. Values of beam sizes and beam divergences at the interaction point, where $\beta_x = 2.5$ m and $\beta_y = 5$ cm, are given in table 3.2 assuming an emittance ratio $\epsilon_y/\epsilon_x = 5\%$ between the vertical and the horizontal planes.

ϵ_x	σ_x^*	σ_y^*	$\sigma_{x'}^*$	$\sigma_{y'}^*$
[nm]	[mm]	[μ m]	[mrad]	[mrad]
15	0.194	6.12	0.078	0.123
20	0.224	7.07	0.089	0.141
25	0.250	7.91	0.100	0.158
30	0.274	8.66	0.110	0.173
35	0.296	9.35	0.118	0.187
40	0.316	10.00	0.127	0.200
45	0.335	10.61	0.134	0.212

Table 3.2: Beam size and divergence at the interaction point for various ϵ_x .

The finite dimensions of the beam and its position at the interaction point have very small effects on the trajectories of e^+e^- pairs and therefore on the detector rates. However, the beam divergence has a small but non negligible effect on the detector rate.

To estimate the systematic error due to the beam divergence on the Bhabha scattering rate of eq. (3.7), a Monte Carlo simulation for tracking Bhabha scattered e^+e^- pairs from the interaction point to the left and right detectors is used. The simulation program includes the dimensions of the vacuum chamber which limit the aperture for e^+e^- pairs.

Simulations of 10^7 Bhabha scattering events were carried out for 10 horizontal emittance values $\{0, 5, 10, \dots, 45 \text{ nm}\}$ and for a detector position X range between 20 and 80 mm. The Bhabha scattering angle θ distribution follows the function $1/\theta^3$ as expected from eq. (3.2) since $d\Omega \simeq \theta d\theta d\phi$. The distribution of the azimuthal angle ϕ is uniform between $-\pi/2$ and $\pi/2$. In order to represent the beam angular spread in the horizontal and vertical planes, the angles θ and ϕ are transformed to

$$x' = \theta \cos \phi \quad , \quad y' = \theta \sin \phi$$

and smeared with a Gaussian distribution independently for the scattered positron and electron.

The limits of the θ distribution are calculated taking into account the position of the detectors and the beam angular spread. For a detector placed at $X_{\min} = 20$ mm, the minimum of the θ distribution is given by the minimum angle θ of the inner edge of the detector minus the maximum horizontal angle of $\pm 6\sigma_x^*$, generated by the Gaussian random generator RG32 [36]:

$$\theta_{\min} = \frac{X_{\min}}{A} - 6\sigma_x^*(\max) = 0.6 \text{ mrad} ,$$

where $\sigma_x^*(\max)$ is the maximum angular spread simulated (see table 3.2). The maximum of the θ -distribution for a detector located at $X_{\max} = 80$ mm is given by the angle θ of the outer corner of the detector plus the maximum horizontal and vertical angle generated by the Gaussian random generator:

$$\theta_{\max} = \sqrt{\left(\frac{X_{\max} + L}{A} + 6\sigma_x^*(\max)\right)^2 + \left(\frac{L/2}{B} + 6\sigma_y^*(\max)\right)^2} = 11.8 \text{ mrad}$$

The θ values are generated in the range from $\theta_{\min} = 0.6$ mrad to $\theta_{\max} = 12$ mrad.

The counting rate of events in which positron and electron hit each detector is

$$\dot{N} = \mathcal{L} \sigma(\theta_{\min} - \theta_{\max}) \frac{N_{(e^+ \& e^-)}}{N_{\text{generated}}}$$

where $N_{\text{generated}}$ is the total number of e^+e^- pairs of the simulation, $N_{(e^+ \& e^-)}$ is the number of e^+e^- pairs detected at both calorimeters and $\sigma(\theta_{\min} - \theta_{\max})$ is the integral of the Bhabha scattering cross section of eq. (3.2) over $\theta_{\min} < \theta < \theta_{\max}$ and $-\pi/2 < \phi < \pi/2$:

$$\sigma(\theta_{\min} - \theta_{\max}) = \frac{4\alpha^2}{E^2} \int_{\theta_{\min}}^{\theta_{\max}} \frac{d\theta}{\theta^3} \int_{-\pi/2}^{\pi/2} d\phi = \frac{2\pi\alpha^2(\hbar c)^2}{E^2} \left(\frac{1}{\theta_{\min}^2} - \frac{1}{\theta_{\max}^2} \right) = 173.6 \text{ } \mu\text{b}$$

using the constant $(\hbar c)^2 = 389.38 \text{ GeV}^2 \mu\text{b}$.

As expected, results of the simulation for $\varepsilon_x = 0$, $\varepsilon_y = 0$ agree with eq. (3.7) within the statistical error of the simulation ($\Delta\dot{N}/\dot{N} = \sqrt{1/N_{(e^+ \& e^-)}}$) which is lower than 0.5%. The effect of the beam divergence on the detector rate at $X = 20, 30, 40$ and 50 mm expressed as the relative change $\Delta\dot{N}/\dot{N}$ as a function of the horizontal emittance values given in table 3.2 is shown in fig. 3.7. Detector positions X which are smaller than $12\sigma_x$ are excluded from this plot, since it is the minimum distance of collimators to the beam.

The size of the vacuum chamber limits the aperture of Bhabha scattering detected at the luminosity monitors. The geometry of the vacuum chamber between the interaction point and the detectors at 8.3 m is shown in fig. 3.8. The vacuum chamber at interaction points 4, 6 and 8 have between 7.10 and 7.43 m from the interaction point an elliptic chamber of 120 mm width and 156 mm height. This elliptic chamber is not present at interaction point 2, where the chamber has a diameter of 156 mm. Bhabha pairs scattered with a horizontal angle of 4.5 mrad (5.5 mrad in the case of interaction point 2) hit the wall of the vacuum chamber and are lost. Consequently, the rate of Bhabha scattering at detectors placed further than $X=35$ mm is smaller than what is calculated in eq. (3.7) and shown in fig. 3.6.

A simulation of Bhabha scattering where the size of the vacuum chamber is taken into account gives the results shown in table 3.3. The effect of the vacuum chamber on the

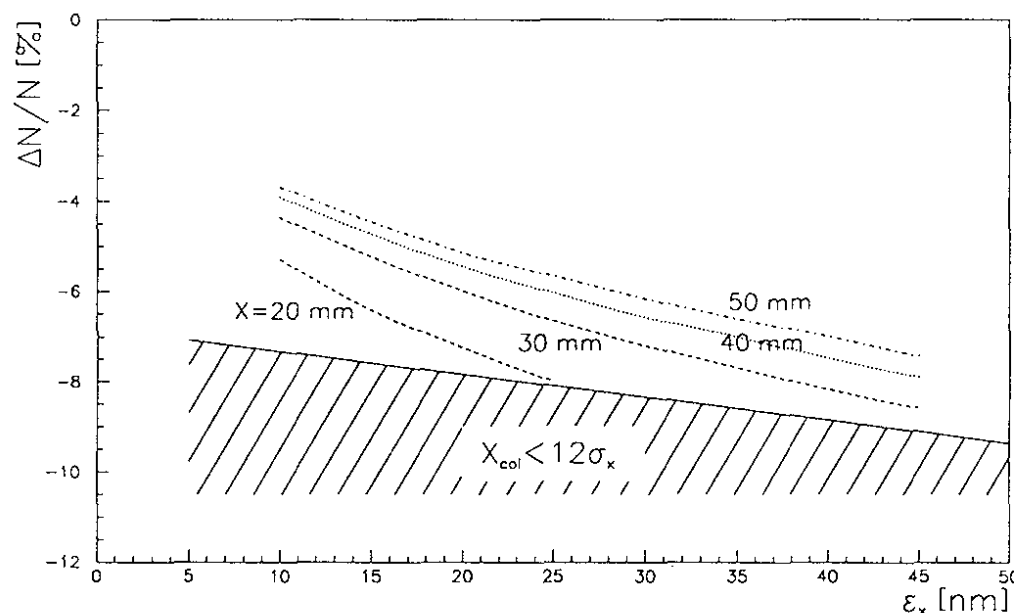


Figure 3.7: Effect on Bhabha scattering rate at detectors due to beam divergence. The relative decrease of Bhabha rate is plotted as a function of the horizontal beam emittance. Typical emittance values are between 15 and 45 nm. The shadowed area limits the minimum detector position of $12\sigma_x$, with σ_x being the horizontal beam size.

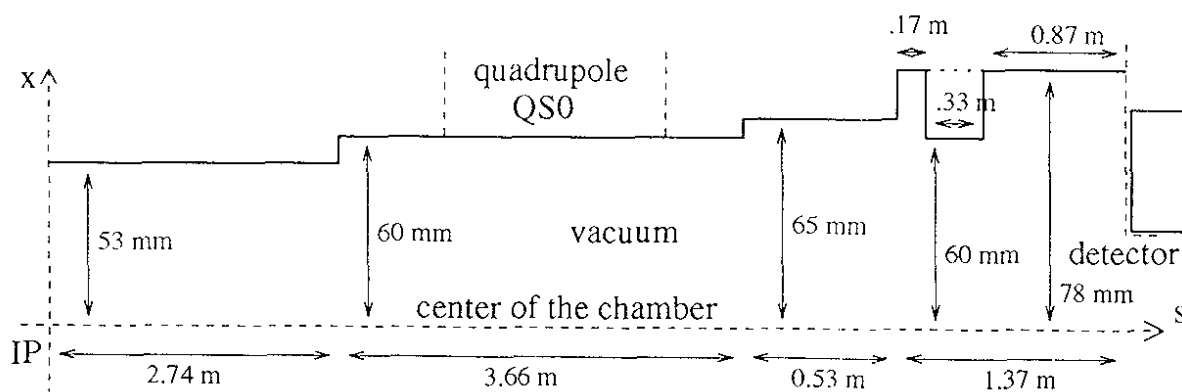


Figure 3.8: Vacuum chamber dimensions at interaction points (IP) 4, 6 and 8. The dotted line shows the profile of the vacuum chamber at interaction point 2 where the elliptic chamber is not installed.

detector pos. X [mm]	$\Delta \dot{N} / \dot{N}$	
	IP 2	IP 4, 6 and 8
35	0%	-3%
40	-3%	-8%
45	-9%	-15%
50	-17%	-25%
55	-27%	-37%
60	-39%	-51%
65	-54%	-71%
70	-73%	-94%
75	-95%	-100%

Table 3.3: Relative Bhabha rate decrease with respect to the rate calculated in eq. (3.7) due to the presence of the vacuum chamber.

Bhabha rate is less than 1% for detector positions smaller than 38 mm at interaction point 2 and 33 mm at interaction points 4, 6 and 8.

The Bhabha scattering rate calculated with eq. (3.7) and shown in fig. 3.6 is compared in fig. 3.9 to simulation results which include the effect of the beam emittance and the vacuum chamber. Both effects reduce the detector acceptance by about 10% with respect to the calculated one in the region between $X = 33$ and 37 mm (the region indicated in the plot).

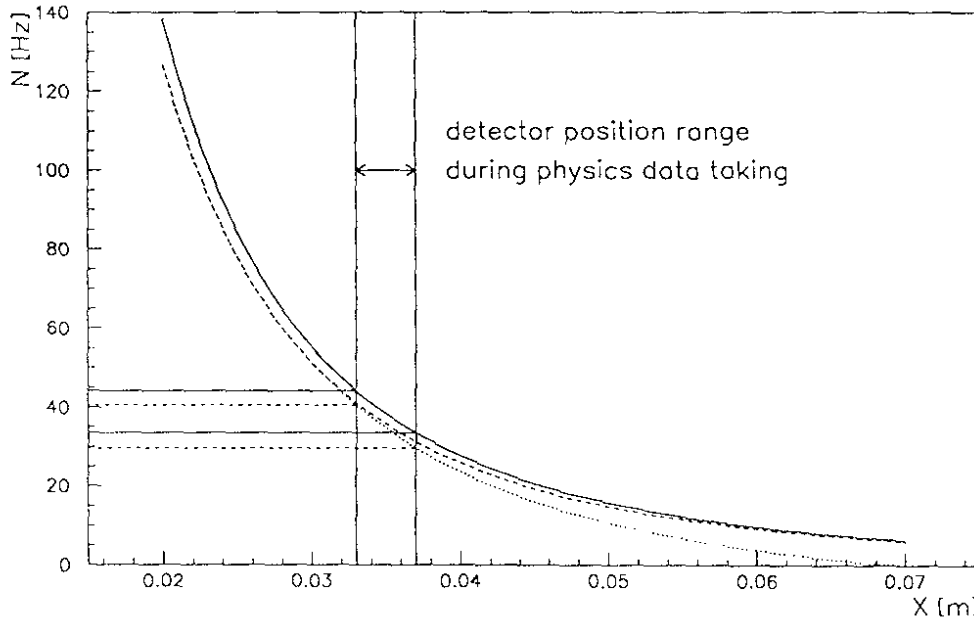


Figure 3.9: Simulated Bhabha scattering rate (full line) at a pair of detectors of area $40 \times 40 \text{ mm}^2$ as a function of the horizontal distance X from the edge of the detector to the beam, for $\mathcal{L} = 10^{31} \text{ cm}^{-2} \text{ s}^{-1}$ and $E = 45.6 \text{ GeV}$. The simulated Bhabha scattering rate including the effect of a horizontal emittance $\epsilon_x = 30 \text{ nm}$ is plotted with a dashed line and including the vacuum chamber limits is plotted with a dotted line.

These results have been compared with results obtained previously [37]. In this paper, the authors used different values for the following parameters: the beam energy is 50 GeV, the superconducting quadrupole strength is $k = -0.16462 \text{ m}^{-2}$, the detector is placed at 8.5 m from the interaction point and the elliptic chamber is placed between 7.65 and 7.90 m

(instead of 7.10 and 7.43 m, the current position) from the interaction point. These values were included into the simulation and the results obtained correspond to the curves given in [37].

3.3 Particle background at the detectors

Vertical and horizontal collimators placed at 8.3 m in both sides of each interaction point protect the LEP experiments by absorbing photons and beam particles traveling off-center from the beam. The luminosity detectors are installed inside the horizontal collimators. The back of these detectors (see fig. 3.10) is shielded by a block of 30 radiation lengths of tungsten. However, the detectors receive background at the frontside coming from the interaction point.

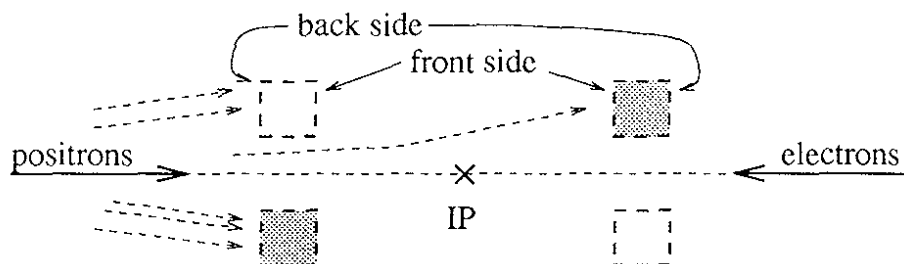


Figure 3.10: Background at the back and front side of luminosity detectors.

The background has the following origin:

- Direct or scattered synchrotron radiation photons produced in the last dipoles of the arc and in the quadrupoles and orbit correction dipoles of the straight section,
- Particles with large oscillation amplitudes, which have lost a small part of their energy (off-momentum particles) in the interaction with residual gas molecules or with thermal photons.

Synchrotron radiation photons do not affect the detectors because these photons, with energies of several tens of keV, are absorbed within the first 5 radiation lengths of lead and tungsten placed in front of the silicon detector S2 (see fig. 3.2).

The calorimeter energy resolution of $64\%/\sqrt{E[\text{GeV}]}$ [26] is not sufficient to discriminate off-momentum particles with energies about 1 GeV less than the beam energy. If the particle background rate is high, accidental coincidences of individual off-momentum particles from each beam can occur within the same bunch crossing and can be detected in coincidence as Bhabha scattering.

Off-momentum particle background

Off-momentum particles with large oscillation amplitudes are due to two phenomena occurring at the arcs:

- By bremsstrahlung photon emission in the interaction between a beam particle and a residual gas molecule in the vacuum chamber,

- By Compton interaction between a beam particle and a thermal photon in the vacuum chamber [38, 39, 40].

Part of the energy of the particle is lost in these interactions. When the energy loss is greater than 1 or 2 GeV, the trajectory of the particle is deflected into the wall of the vacuum chamber, as the deflection due to dipole fields is stronger for particles with smaller energy. However, if the particle loses less than 1 or 2 GeV, it can travel for a few hundred meters oscillating around the orbit with a large amplitude until it hits a collimator.

The number of off-momentum particles which create background at luminosity detectors is significantly reduced by pairs of collimators placed in the horizontal plane in the internal side of the beam orbit at the end of the arc. The difference between the phase of betatron oscillations at collimators and at the detectors located on the opposite side of the interaction point must be near a multiple of 2π in order to protect the internal detector or be near $(2n + 1)\pi$ (n : integer) to protect the external detector. The effect of a pair of collimators adjacent to quadrupoles QS15 and QD20 protecting the internal and the external detectors from off-momentum particles is schematically shown in fig. 3.11.

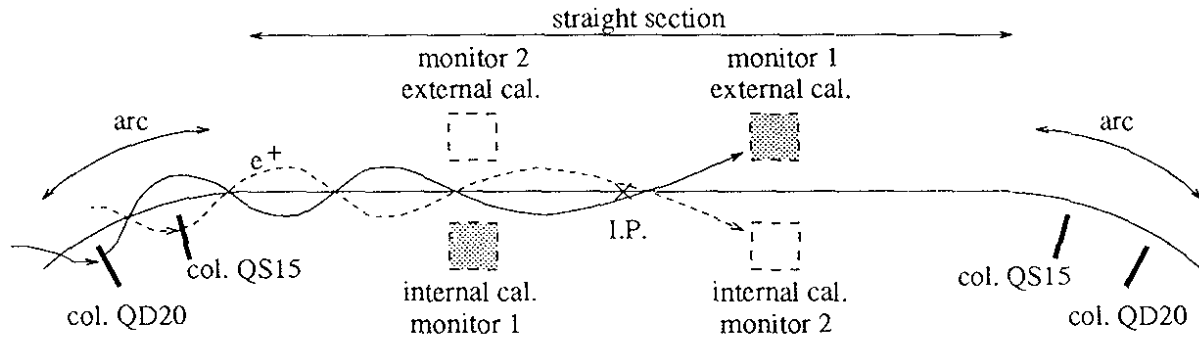


Figure 3.11: Top view (not to scale) of the location of LEP luminosity detectors and off-momentum collimators. (col.: collimator, cal.: calorimeter.)

The QS15 collimators are located at 357 m from the interaction point and QD20 collimators are located at 522 m, on both sides of each interaction point. The phase advance between QS15 collimators and the opposite internal detector is $2 \times 360^\circ + 10^\circ$ and between QD20 collimators and the opposite external detector is $2 \times 360^\circ + 187^\circ$, for the optics configuration used in 1992, 1993 and 1994 of 90° horizontal phase advance per FODO cell.

The optics configuration used in 1990 and 1991 had a 60° phase advance per FODO cell in the horizontal plane. According to the phase advance requirements described in the previous paragraph, the collimators were placed near the quadrupoles QS17 and QF23, at 420 and 637 m from both sides of each interaction point, respectively.

Particle background rates

The particle background rates shown in table 3.4 are normalized to beam intensities and averaged over all monitors. This table shows also the accidental coincidence rate \dot{n}_{acc} of particle background in the external and internal calorimeters normalized to beam intensities for $k_b = 4$ and $k_b = 8$ bunches per beam. Note that the particle background rate is higher at the detectors located on the external side than at the ones on the internal side.

The optics configuration was changed in 1992 to have a 90° phase advance per FODO cell in the horizontal plane. As a consequence of this phase advance change, the QS17 and QF23

year	optics	collimators	\dot{n} [Hz/mA]		\dot{n}_{acc} [Hz/mA ²]	
	$\Delta\mu_x/\Delta\mu_y$		external cal.	internal cal.	$k_b = 8$	$k_b = 4$
1991	60°/60°	QS17, QF23	1500±100	200±100	7	14
1992	90°/60°	—	6000±1000	900±100	60	120
1993		QS15	6000±1000	130±50	17	34
1994		QS15, QD20	1400±100	150±50	4	8

Table 3.4: Intensity normalized particle background rates \dot{n} and accidental coincidence rate \dot{n}_{acc} at luminosity detectors. k_b is the number of bunches per beam. $\Delta\mu_x/\Delta\mu_y$ are the horizontal and vertical phase advance per FODO cell.

collimators were no longer effective to protect the detectors and off-momentum background rates increased in 1992 with respect to 1991 (see table 3.4).

New collimators were installed near the quadrupoles QS15 at the beginning of 1993 reducing the internal background rate and the accidental rate. The ratio between internal background rates of 1993 and 1992 shows that the average reduction factor of QS15 collimators is about 6-7. An experiment [41] measured the efficiency of the collimators at QS15 as a function of its position on the right side of interaction point 2 and on the left side of interaction point 6 (fig. 3.12). The background reduction factors are about 4 and 7, respectively.

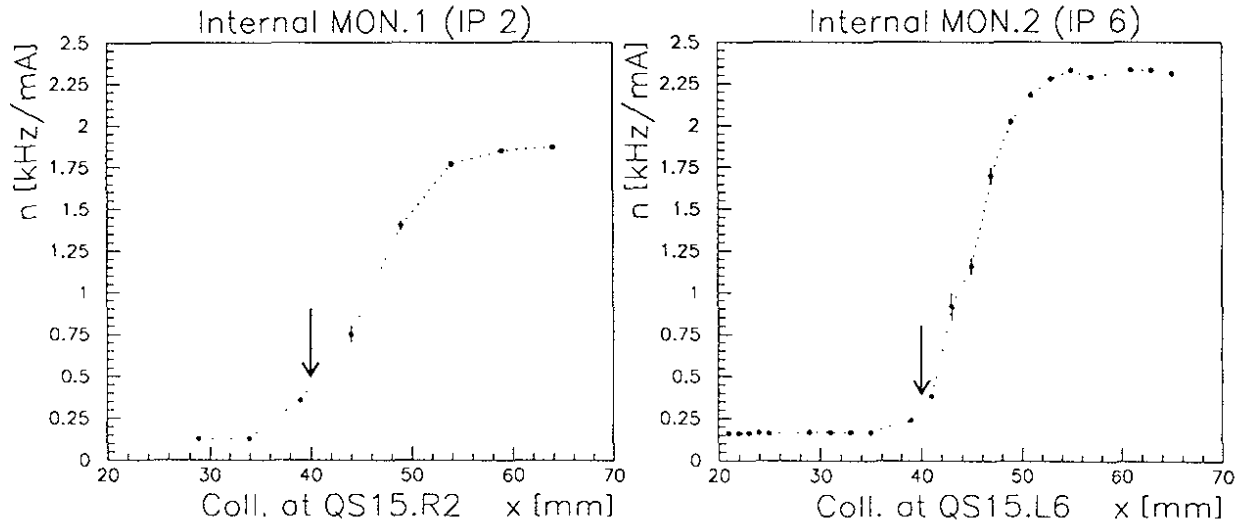


Figure 3.12: Normalized particle background rate received at two internal calorimeters versus the horizontal position x of the collimator located in the arc near quadrupole QS15. Left plot: rate at the internal calorimeter of monitor 1 (MON.1) of interaction point 2 (IP 2) versus the position of the QS15 collimator in the arc on the right of point 2. Right plot: rate at the internal calorimeter of monitor 2 (MON.2) of interaction point 6 (IP 6) versus the position of the QS15 collimator in the arc on the left of point 6. The data was taken on Aug. 2nd 1993. The arrows indicate the collimator position during physics data taking (40 mm).

QD20 collimators were installed at the beginning of 1994 to protect the external detectors. A reduction factor of about 4 between external background rates in 1994 and in 1992 was achieved.

Correction of particle background coincidence

The accidental coincidence due to background at the internal and the external detectors affects the measurements of the coincidence pairs from Bhabha scattering events. The collimators installed at QS15 and QD20 help reduce the accidental coincidence rate to similar or lower values than the Bhabha scattering rate. The remaining background must be measured and subtracted from the monitor pair rate.

The Bhabha scattering rate \dot{N}_b is obtained by

$$\dot{N}_b = \dot{N}_{pair} - \dot{N}_{acc} , \quad (3.8)$$

where \dot{N}_{pair} is the total e^+e^- pair rate and \dot{N}_{acc} is the accidental coincidence rate. Assuming uncorrelated particle background, the coincidence rate \dot{N}_{pair} can be corrected by:

1. Measuring the coincidence rate between the internal detector and the external detector one bunch crossing later (*delayed coincidence*).
2. Calculating the probability of coincidences due to background in the internal and external detectors.

In the following, both possibilities are considered and discussed.

1. The accidental coincidence rate between external and internal detectors can be measured as the coincidence rate between the internal detector and the external detector one (or n in general) bunch crossing(s) later. This can be implemented easily in the logic of the data acquisition (for example, by a flip/flop memory). However, this procedure has limited precision due to the statistical error of the measured coincidence rate.

The Bhabha scattering rate obtained from eq. (3.8) has an error

$$\Delta \dot{N}_b = \sqrt{\Delta \dot{N}_{pair}^2 + \Delta \dot{N}_{acc}^2} . \quad (3.9)$$

If the accidental coincidence rate \dot{N}_{acc} is measured by counting the coincidences between internal background and one turn delayed external background, its error is

$$\Delta \dot{N}_{acc} = \frac{\Delta N_{acc}}{\Delta t} = \frac{\sqrt{N_{acc}}}{\Delta t} = \sqrt{\frac{\dot{N}_{acc}}{\Delta t}} \quad (3.10)$$

with Δt being the measurement time.

2. The accidental coincidence rate can be estimated by

$$\dot{N}_{acc} = \frac{\dot{N}_{ext} \dot{N}_{int}}{k_b f_{rev}} , \quad (3.11)$$

where \dot{N}_{ext} and \dot{N}_{int} are the particle background rates at the external and internal calorimeters, k_b is the number of bunches per beam and f_{rev} the revolution frequency.

The statistical error of \dot{N}_{acc} obtained with eq. (3.11) is

$$\Delta \dot{N}_{acc} = \sqrt{\frac{\dot{N}_{ext}^2}{(k_b f_{rev})^2} (\Delta \dot{N}_{int})^2 + \frac{\dot{N}_{int}^2}{(k_b f_{rev})^2} (\Delta \dot{N}_{ext})^2}$$

where

$$\Delta \dot{N}_{ext} = \sqrt{\frac{\dot{N}_{ext}}{\Delta t}} , \quad \Delta \dot{N}_{int} = \sqrt{\frac{\dot{N}_{int}}{\Delta t}} .$$

Then, we have

$$\Delta \dot{N}_{acc} = \sqrt{\frac{\dot{N}_{ext}^2 \dot{N}_{int} + \dot{N}_{int}^2 \dot{N}_{ext}}{\Delta t (k_b f_{rev})^2}}.$$

Inserting eq. (3.11) we get

$$\begin{aligned} \Delta \dot{N}_{acc} &= \sqrt{\frac{\dot{N}_{acc}(\dot{N}_{ext} + \dot{N}_{int})}{\Delta t k_b f_{rev}}} \\ &= \sqrt{\frac{\dot{N}_{acc}}{\Delta t}} \sqrt{\frac{\dot{N}_{ext} + \dot{N}_{int}}{k_b f_{rev}}} \end{aligned}$$

which is smaller than $\Delta \dot{N}_{acc}$ of eq. (3.10), because $\dot{N}_{ext} + \dot{N}_{int}$ is at least one or two orders of magnitude smaller than $k_b f_{rev}$, the number of bunch crossings per second. Therefore, the accidental coincidence rate obtained using eq. (3.11) from the external and internal background rates measured is more accurate than the delayed coincidences rate.

Correction for high particle background rates

When background rates are very high, the calculation of \dot{N}_b from eq. (3.8) introduces a systematic error. The systematic error of the accidental rate \dot{N}_{acc} calculated with eq. (3.11) is shown in fig. 3.13 as a function of the particle background rate.

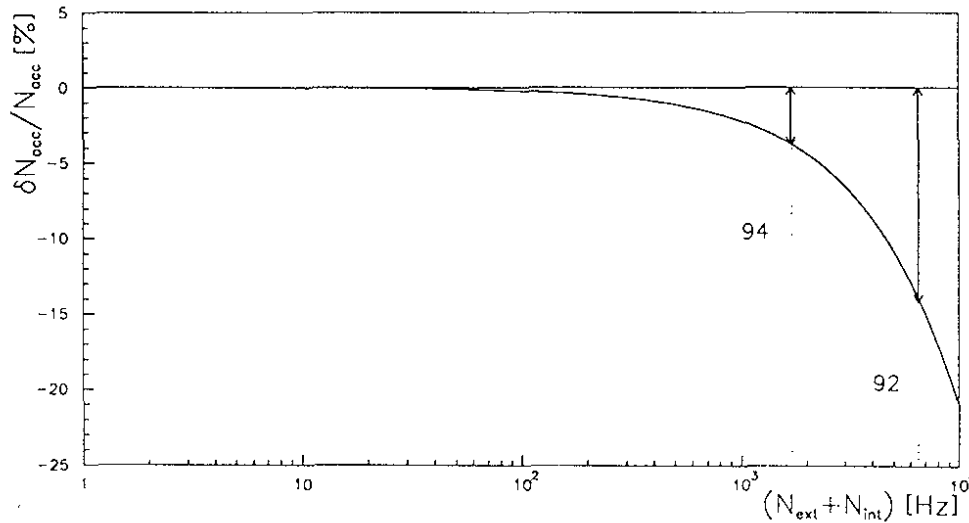


Figure 3.13: Relative systematic error on the accidental rate \dot{N}_{acc} of eq. (3.11) due to high particle background rates with respect to $\dot{N}_{ext}\dot{N}_{int}/D$ of eq. (3.18). The typical background rate during physics in 1992 and in 1994 are indicated.

In the following, the expressions of \dot{N}_b and $\Delta \dot{N}_b$ are obtained from a calculation of probabilities in second order for the values \dot{N}_{ext} , \dot{N}_{int} and \dot{N}_{pair} .

Let P_e and P_i be the probability to detect in one bunch crossing a particle background at the external and the internal detectors, respectively. P_b is the probability for a Bhabha scattered e^+e^- pair to be detected at both external and internal detectors simultaneously, which theoretical rate \dot{N}_b was calculated using eq. (3.7) for a luminosity \mathcal{L} .

Luminosity monitors measure external and internal particle background rates, \dot{N}_{ext} and \dot{N}_{int} , and the pair rate \dot{N}_{pair} . These rates are associated to P_{ext} , P_{int} and P_{pair} , which are

defined as the probability to detect a particle only at the external detector, only at the internal detector and at both detectors, respectively, in one bunch crossing.

For low particle background rates, the probability to detect an accidental coincidence of an internal and an external particle background can be calculated in first approximation as the product of internal and external background probabilities

$$P_{acc} = P_e P_i .$$

Multiplying both sides by the number of bunch crossings per second $k_b f_{rev}$, this equation corresponds to eq. (3.11).

For higher background rates, second order probabilities have to be considered in the calculation of P_{acc} in order to take into account coincidences between internal background, external background and Bhabha scattering pairs. The probability to detect a background particle only at the external detector (no particle at the internal detector) can be expressed as the probability of a background particle to hit the external detector and the probability that no background particle hits the internal detector and the probability of no Bhabha scattered e^+e^- pair at internal and external detectors

$$P_{ext} = P_e (1 - P_i)(1 - P_b) . \quad (3.12)$$

Similarly, the probability to detect a background particle only at the internal detector is

$$P_{int} = P_i (1 - P_e)(1 - P_b) . \quad (3.13)$$

The probability to detect a particle at both external and internal detectors in the same bunch crossing can be written as the probability of both external and internal detectors being hit by a background particle, $P_i P_e$, and/or the probability of a Bhabha scattering pair, P_b , incident at both detectors

$$P_{pair} = P_e P_i + P_b - P_e P_i P_b . \quad (3.14)$$

Eqs. (3.12), (3.13) and (3.14) form a system of 3 equations and 3 unknowns. The solutions of this system of equations are:

$$P_e = \frac{P_{ext}}{1 - P_{int} - P_{pair}} \quad (3.15)$$

$$P_i = \frac{P_{int}}{1 - P_{ext} - P_{pair}} \quad (3.16)$$

$$P_b = P_{pair} - \frac{P_{ext} P_{int}}{1 - P_{ext} - P_{int} - P_{pair}} . \quad (3.17)$$

In terms of counting rates (multiplying by $k_b f_{rev}$), eq. (3.17) becomes

$$\dot{N}_b = \dot{N}_{pair} - \frac{\dot{N}_{ext} \dot{N}_{int}}{D} , \quad \text{with} \quad D = k_b f_{rev} - \dot{N}_{ext} - \dot{N}_{int} - \dot{N}_{pair} . \quad (3.18)$$

The statistical error of \dot{N}_b is given by

$$\Delta \dot{N}_b = \sqrt{\left(\frac{\partial \dot{N}_b}{\partial \dot{N}_{ext}}\right)^2 \Delta \dot{N}_{ext}^2 + \left(\frac{\partial \dot{N}_b}{\partial \dot{N}_{int}}\right)^2 \Delta \dot{N}_{int}^2 + \left(\frac{\partial \dot{N}_b}{\partial \dot{N}_{pair}}\right)^2 \Delta \dot{N}_{pair}^2}$$

with

$$\frac{\partial \dot{N}_b}{\partial \dot{N}_{ext}} = -\frac{\dot{N}_{int}(D + \dot{N}_{ext})}{D^2}, \quad \frac{\partial \dot{N}_b}{\partial \dot{N}_{int}} = -\frac{\dot{N}_{ext}(D + \dot{N}_{int})}{D^2}, \quad \frac{\partial \dot{N}_b}{\partial \dot{N}_{pair}} = 1 - \frac{\dot{N}_{ext}\dot{N}_{int}}{D^2}.$$

If the counting rates are measured for a period of time Δt , then the statistical errors are:

$$\Delta \dot{N}_{ext} = \sqrt{\frac{\dot{N}_{ext}}{\Delta t}}, \quad \Delta \dot{N}_{int} = \sqrt{\frac{\dot{N}_{int}}{\Delta t}}, \quad \Delta \dot{N}_{pair} = \sqrt{\frac{\dot{N}_{pair}}{\Delta t}}$$

and the statistical error of \dot{N}_b is

$$\Delta \dot{N}_b = \frac{\sqrt{\dot{N}_{ext}^2 \dot{N}_{int}(D + \dot{N}_{int})^2 + \dot{N}_{ext} \dot{N}_{int}^2 (D + \dot{N}_{ext})^2 + \dot{N}_{pair}[D^2 - \dot{N}_{ext}\dot{N}_{int}]^2}}{D^2 \sqrt{\Delta t}}. \quad (3.19)$$

If the particle background rates $\dot{N}_{ext}, \dot{N}_{int} \ll k_b f_{rev}$, then $D \simeq k_b f_{rev}$ and eq. (3.19) can be approximated to

$$\Delta \dot{N}_b \simeq \sqrt{\frac{\dot{N}_{pair}}{\Delta t}} = \Delta \dot{N}_{pair},$$

which is smaller than the error of \dot{N}_b calculated from eq. (3.8) with measured accidental coincidence rate.

3.4 Results

3.4.1 Detector efficiency

The acceptance of the detector is defined as the ratio between the measured Bhabha scattering rate \dot{N} and luminosity \mathcal{L} . The calibration of LEP luminosity monitors is carried out by comparison to luminosity measurements of the LEP experiments L3, ALEPH, OPAL and DELPHI. As a result of this comparison, the average detector acceptance \dot{N}/\mathcal{L} per monitor over all interaction points is determined within a 5% error

$$\dot{N}/\mathcal{L} = 3.8 \mu\text{b}$$

for $X_{col} = 30$ mm. Luminosity measured with LEP monitors and on-line luminosity measurement from the luminosity detectors of the LEP experiments are in reasonable agreement. An example is shown in fig. 3.14.

The position X of the inner edge of the sensitive silicon area of the detector is at 2.7 mm from the collimator edge X_{col}

$$X = X_{col} + 2.7 \text{ mm}.$$

The efficiency of LEP luminosity monitors is given by the calibrated acceptance with respect to the acceptance calculated from the simulation for a horizontal emittance of 30 mm and for $X = (30.0 + 2.7)$ mm

$$\epsilon = \frac{3.8 \mu\text{b}}{4.2 \mu\text{b}} \simeq 90\%.$$

The Bhabha scattering detection efficiency of the monitors depends on the signal threshold which selects high energy events. The voltage pulse of the silicon semiconductor material is proportional to the charge of the electromagnetic cascade collected over the detector

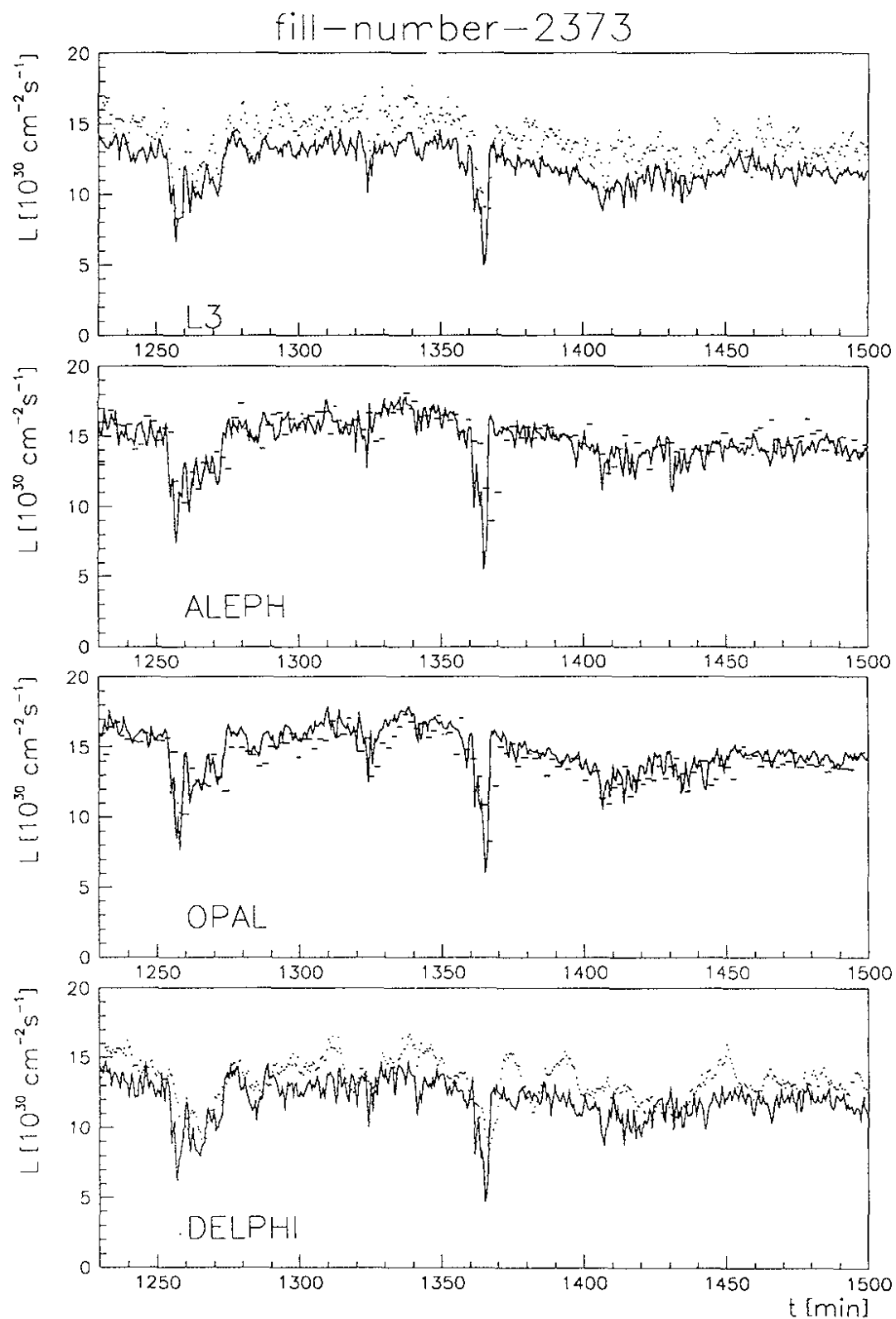


Figure 3.14: Comparison between luminosity measured with LEP monitors (full lines) at each interaction point and on-line luminosity of the LEP experiments (dots).

surface. The small dimensions of the silicon detectors ($40 \times 40 \text{ mm}^2$) used for luminosity measurements at LEP limit the full containment of the electromagnetic cascade created by electrons (or positrons) incident in the calorimeter. A good fraction of Bhabha scattered e^+e^- pairs hits the detectors in a range of a few millimeters from its inner edge, where part of their electromagnetic cascades are not detected.

Determination of the signal threshold

The signal threshold is adjusted to discriminate the electronic noise of the signals. While part of this electronic noise originates in the preamplification of the detector signals, there is a significant contribution from an external source. It was found that electronic pulses provided by the power supplies for the stepping motors which drive the collimators are a source of noise to the detector signals. In order to reduce this noise, the output of the power supplies are connected to low-pass frequency filters.

The determination of the threshold is obtained by analyzing the frequency distribution of the detector signal amplitude. The DSP module has an extended memory of 32 kbytes. Two blocks of four kbytes (one block per detector) are booked in order to acquire a histogram of the digital signal of 12-bit. An example of the histograms of the external and the internal detector signals are shown on the first two upper plots in fig. 3.15. A third block of four kbytes is reserved to acquire the histogram of the least value of the external and the internal detector signals at the same bunch crossing, which is shown on the right upper plot in fig. 3.15.

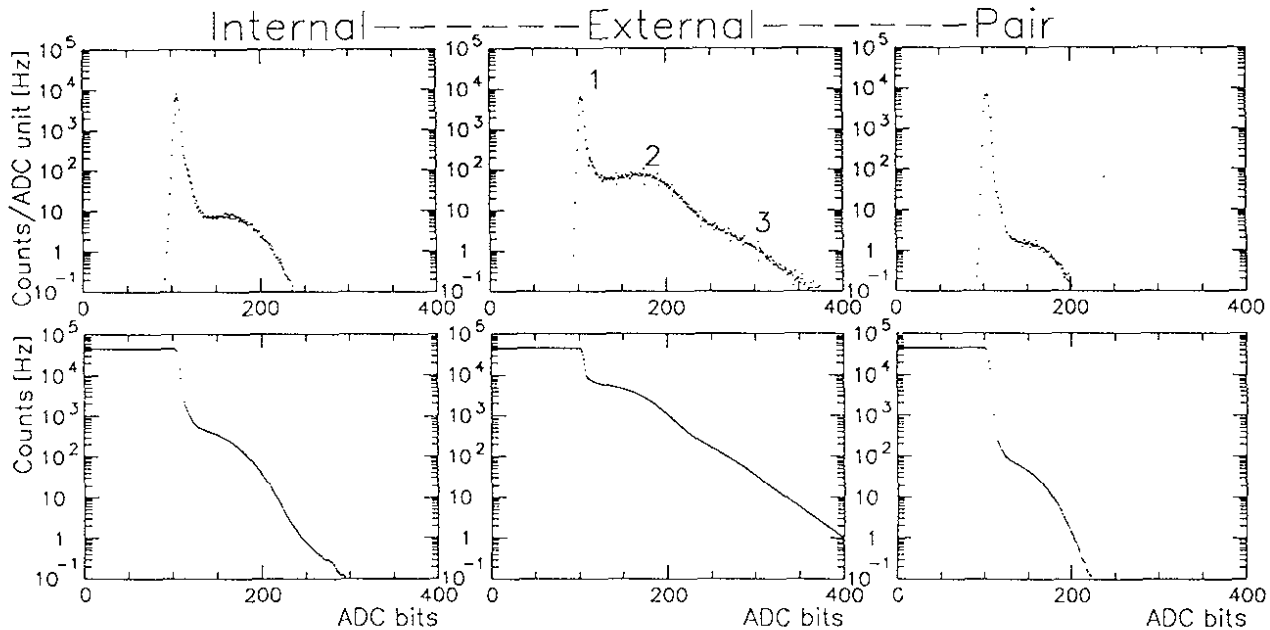


Figure 3.15: Histogram of the frequency distribution of internal and external calorimeter signals (and least value of them) in ADC units during 180 seconds. The lower plots are the accumulated histograms of the upper ones (see text). The acquisition frequency is $4 f_{rev} = 45 \text{ kHz}$. The narrow, high peak (1) in these histograms is the pedestal signal and its width corresponds to the electronic noise voltage in bit units. The lower peak on the right (2), which is wider than the pedestal peak, represents the spectrum of the energy deposited by the cascade on the silicon detector. In the histogram of the external detector, whose particle rate is higher, we observe a long tail (3) corresponding to acquisitions when two particles hit the detector at the same bunch crossing.

The three lower plots in fig. 3.15 correspond to the accumulated histograms of the upper

ones. They are obtained by

$$a(j) = \sum_{k=j}^{4095} h(k) ,$$

where $a(j)$ is the accumulated histogram and $h(k)$ is the histogram value corresponding to the ADC bin k .

The histogram values $i(j)$, $e(j)$ and $p(j)$ corresponding to the three lower plots in fig. 3.15 are equivalent to the rates \dot{N}_{int} , \dot{N}_{ext} and \dot{N}_{pair} for a threshold value of j in ADC bits. The Bhabha scattering rate $b(j)$ as a function of the threshold j is deduced from eq. (3.18) replacing \dot{N}_{int} , \dot{N}_{ext} , \dot{N}_{pair} and \dot{N}_b by $i(j)$, $e(j)$, $p(j)$ and $b(j)$

$$b(j) = p(j) - \frac{e(j)i(j)}{k_b f_{rev} - e(j) - i(j) - p(j)} .$$

The Bhabha scattering rate $b(j)$ is shown as a function of the signal threshold in fig. 3.16.

The signal threshold is set to the minimum value on the right side of the sharply rising peak of pedestal signal seen in fig. 3.16, sitting in an almost horizontal "plateau". The determination of thresholds gave the following results

interaction point	monitor1 (in ADC bits)	monitor2
2	130	135
4	135	130
6	130	130
8	135	140

The relative error of the measured Bhabha scattering rate $b(j)$ as a function of the threshold j is shown in fig. 3.17 as deduced from eq. (3.19) replacing \dot{N}_{int} , \dot{N}_{ext} , \dot{N}_{pair} and \dot{N}_b by $i(j)$, $e(j)$, $p(j)$ and $b(j)$ and for $\Delta t = 180$ s. Discarding the region of electronic noise, it is observed that the relative error increases (since the measured Bhabha scattering rate decreases) for larger threshold values.

3.4.2 Detector acceptance measurement as a function of collimator position

The luminosity detectors are mounted in the horizontal collimators, which are moved to a position X_{col} from the center of the vacuum chamber during operation with beams in collision. The position at which the two collimator jaws are located (between $-X_{col}$ and X_{col}) is adjusted to the horizontal beam size σ_x . The minimum X_{col} position must be $12\sigma_x$, in order not to become the aperture limit, although the optimum position is adjusted experimentally depending on the background received at the LEP experiments. Typical values of X_{col} during the operation of LEP are listed in table 3.5.

The Bhabha scattering rate rapidly decreases as a function of X as it is shown in fig. 3.6. Therefore, the detector acceptance is scaled with the position of the collimators by the factor

$$F = \left(\frac{X_{col} + 2.7 \text{ mm}}{32.7 \text{ mm}} \right)^a$$

where $a = 2.5$ is obtained from a fit to eq. (3.7).

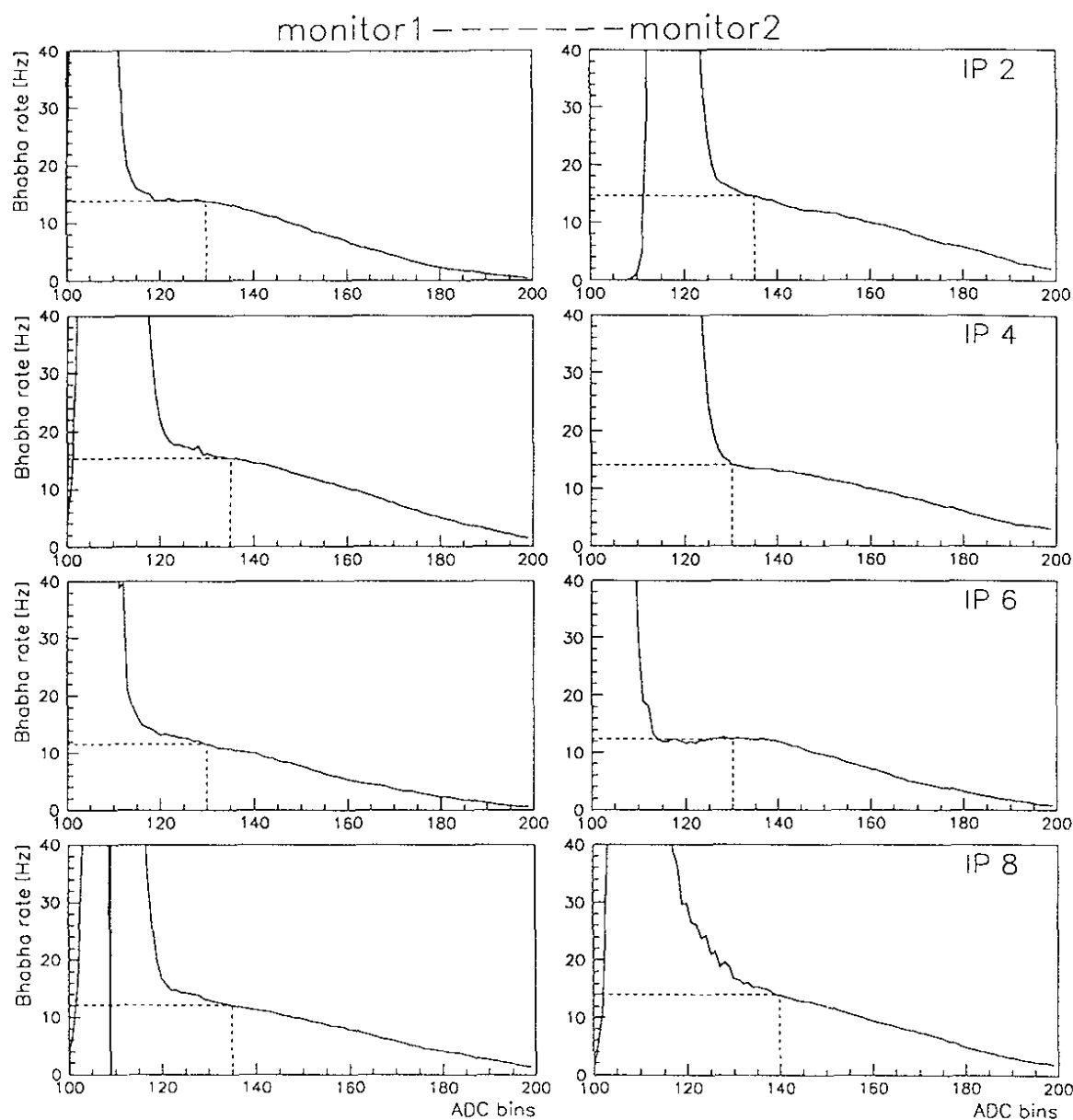


Figure 3.16: Bhabha scattering rate versus threshold level (same for internal and external signals) for all luminosity monitors. Signal thresholds are indicated with vertical dashed lines. The luminosity is about $4 \cdot 10^{30} \text{ cm}^{-2}\text{s}^{-1}$ and the background coincidence rate is in average eight times the Bhabha scattering rate.

year	IP 2	IP 4	IP 6	IP 8
1991	33	30/31	33	30/33
1992	31	31	35/32	32
1993	30	30	32	32
1994	34	33	31	32

Table 3.5: Collimator positions X_{col} in millimeters for LEP operation (IP: interaction point).

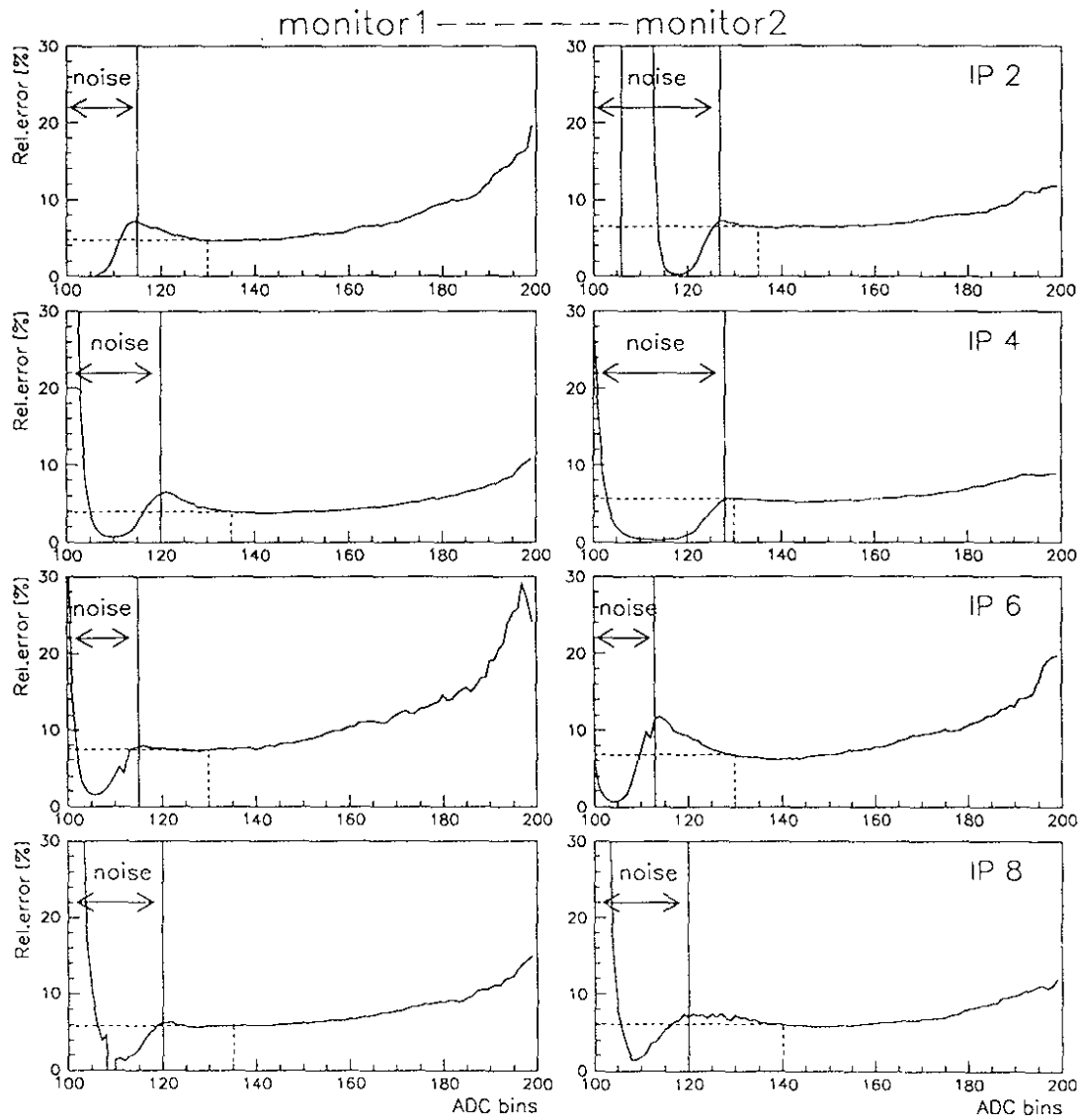


Figure 3.17: Relative error of the measured Bhabha scattering rate as a function of the threshold level (same for internal and external signals) for all luminosity monitors.

The detector acceptance as a function of its position has been determined experimentally [41, 43] and a good agreement with eq. (3.7) was found. The first detector position scan was done in July 1991 with beam intensities $I_{e-} = 0.9$ mA and $I_{e+} = 1.3$ mA at interaction point 2. Collimators were moved from $X_{col} = 25$ to 47 mm. At each point, data was acquired for three minutes. The average between the counting rate of monitor 1 and monitor 2 is shown in fig. 3.18. The result of a fit of the detector acceptance obtained by simulation including the limits of the vacuum chamber at interaction point 2 is plotted as well. Note that the last three measurement points (from $X_{col} = 43$ to 47 mm) agree better with simulation results than with eq. (3.7).

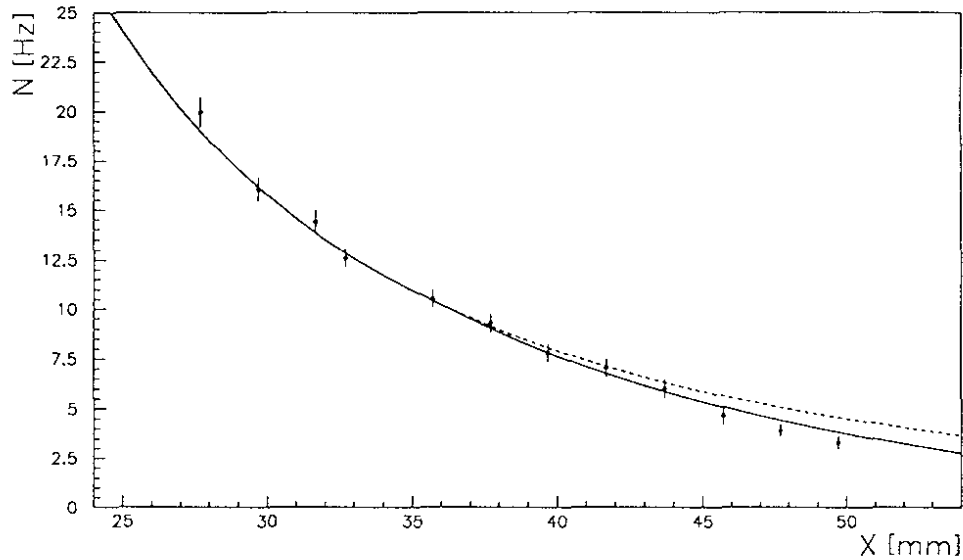


Figure 3.18: Monitor rate measured at interaction point 2 as a function of its horizontal position X in July 1991. The fit of simulation results including the vacuum chamber dimensions in interaction point 2 gives $\mathcal{L} = (2.85 \pm 0.04) \cdot 10^{30} \text{ cm}^{-2}\text{s}^{-1}$ and is shown with a full line. Eq. (3.7) for the same luminosity is plotted with a dashed line.

Another experiment was carried out in August 1993 with both monitors of interaction point 2, moving the four horizontal collimators from 27 to 40 mm. During this experiment the luminosity of the colliding beams was perturbed. To maintain high luminosity the vertical dispersion was corrected, followed by an orbit correction. The counting rates of monitors at interaction points 4, 6 and 8 were recorded as a reference. The counting rate at monitor 1 and 2 of interaction point 2 was measured and compared to the reference rates. The average rate between monitor 1 and 2 versus the detector position is shown in fig. 3.19 as well as the function of eq. (3.7) fitted to the experimental points.

The Bhabha rates measured as a function of the detector position are in good agreement with the detector acceptance versus position calculated in section 3.2.

3.4.3 Measurement of the luminosity statistical error

The statistical error of measured Bhabha scattering rate is calculated using eq. (3.19). This expression takes into account the statistics of the Bhabha pair rate and of the accidental background coincidence rate. The Bhabha pair rate and its statistical error are scaled to provide the luminosity measurement and its error.

An estimate of the statistical error of luminosity measurements is taken from the measured luminosity at time t_i minus the measured luminosity at time $t_{i-1} = t_i - \Delta t$, where Δt is

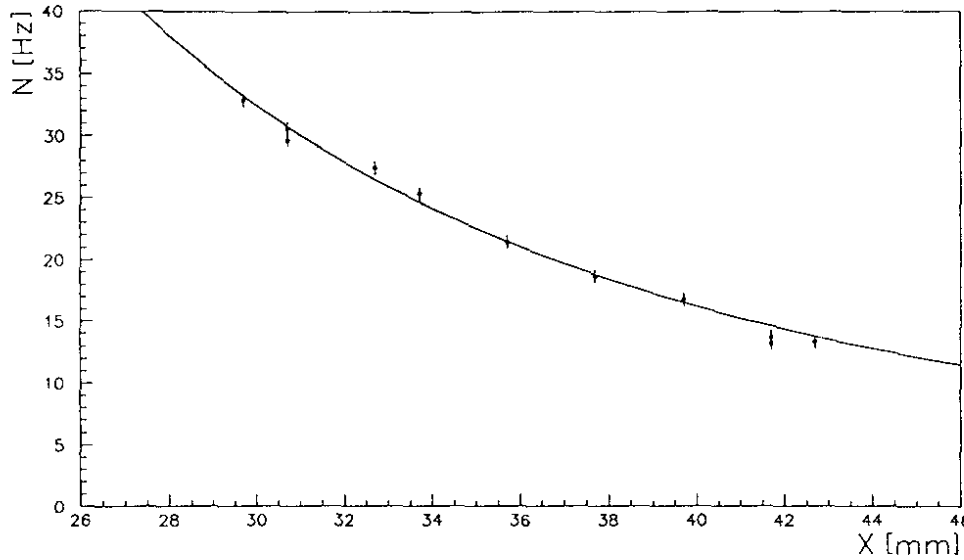


Figure 3.19: Monitor rate measured at interaction point 2 as a function of its horizontal position in August 1993. The fit of eq. (3.7) gives $\mathcal{L} = (5.86 \pm 0.03) \cdot 10^{30} \text{ cm}^{-2}\text{s}^{-1}$ and is shown with a line.

the acquisition time. If the variation of the luminosity is only due to statistical fluctuations, the r.m.s. of this difference $\mathcal{L}_i - \mathcal{L}_{i-1}$ divided by $\sqrt{\sigma_i^2 + \sigma_{i-1}^2}$ (where σ_i is the luminosity error calculated from the Bhabha rate error of eq. (3.19)) must be one.

In fig 3.20, histograms of $(\mathcal{L}_i - \mathcal{L}_{i-1})/\sqrt{\sigma_i^2 + \sigma_{i-1}^2}$ for the luminosity measured at interaction points 2, 4, 6 and 8 are plotted. The acquisition time is nine seconds and the statistical error is about 5%. The shape of the four histograms fits well to a Gaussian function and the average sigma from the four histograms gives 0.995 ± 0.008 . This demonstrates that the statistical error calculated using eq. (3.19) is correct.

3.4.4 Vernier scan

The optimization of the LEP collider performance needs accurate luminosity measurements within a short time interval at the four interaction points. Fast monitoring of luminosity allows to detect quickly any deviation from the optimum collision parameters: beam-beam strength, vertical beam size, closed orbit changes, etc. With the help of LEP luminosity monitors and other beam instrumentation it is possible to rapidly diagnose problems and recover in a short time.

At LEP, closed orbit measurements are not precise enough to determine the beam position with a few micrometers accuracy at the interaction points. Instead, the optimization procedure of the beam overlap in the vertical plane at the interaction points is called *Vernier scan* and uses the luminosity measurements. During such a scan the beams are displaced one against the other with vertical electrostatic separators. For each step, the luminosity is measured.

The measured luminosity plotted as a function of the vertical displacement follows the shape of a Gaussian function. The maximum indicates the setting where the vertical beam separation is zero. The size of this Gaussian expressed in terms of its standard deviation σ_{scan} gives direct information about the vertical size of the beams at the interaction point (see appendix A, eq. A.3)

$$\sigma_{\text{scan}} = \sqrt{\sigma_{e^-}^2 + \sigma_{e^+}^2} .$$

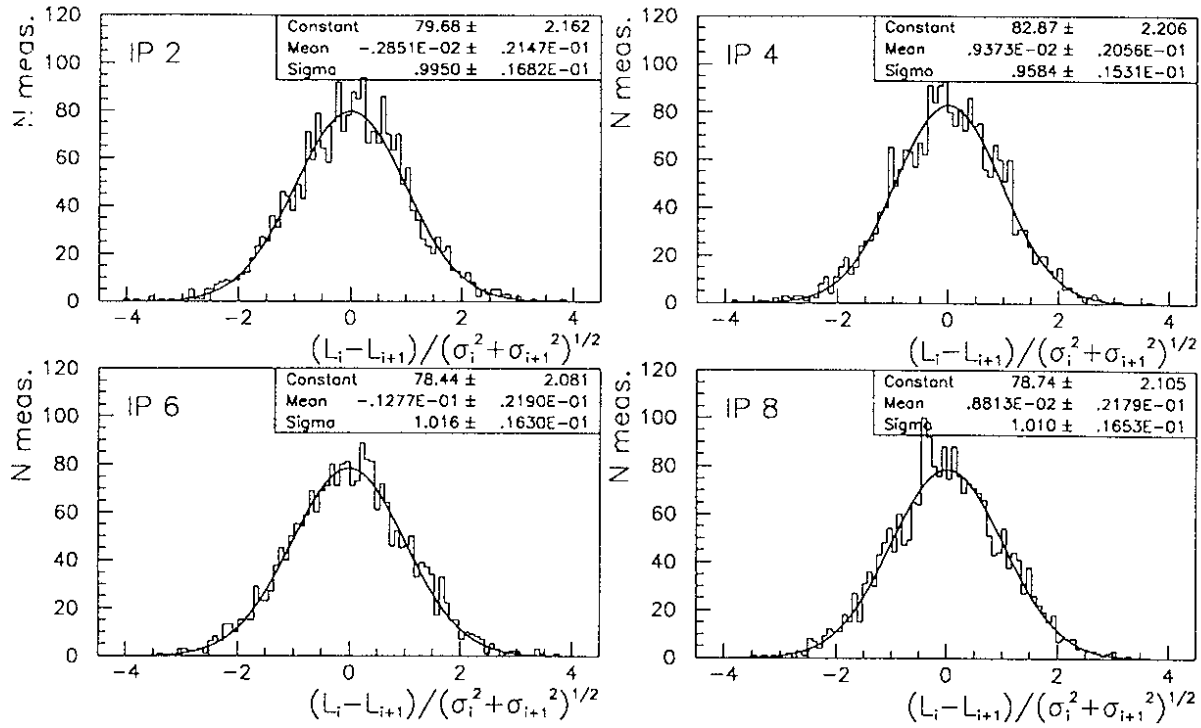


Figure 3.20: Histograms of luminosity measurement fluctuations at each interaction point divided by the calculated error using eq. (3.19). Luminosity data was taken during the physics fill 2958 (Sept. 5th 1995) and histograms are made from more than 2000 luminosity measurements between 15 and $20 \cdot 10^{30} \text{ cm}^{-2} \text{ s}^{-1}$.

When the sizes of both beams are equal, σ_y is obtained by dividing σ_{scan} by $\sqrt{2}$. Vernier scans have been used to measure the vertical beam emittance [5] from

$$\varepsilon_y = \frac{\sigma_{\text{scan}}^2}{2\beta_y^*} \quad (3.20)$$

where β_y^* is the value of the beta function at the interaction point.

An example of Vernier scans done in all four interaction points is shown in fig. 3.21. Vernier scans in interaction points 2 and 6 were carried out five days later than those in interaction points 4 and 8. The optimal electrostatic separation was found at $4.8 \pm 0.8 \mu\text{m}$ at interaction point 2, $5.0 \pm 1.5 \mu\text{m}$ at 4, $-8.1 \pm 0.8 \mu\text{m}$ at 6 and $-3.6 \pm 1.3 \mu\text{m}$ at 8. Using eq. (3.20) for $\beta_y^* = 5 \text{ cm}$, the vertical emittance extracted from the Gaussian distribution fit to the data points at the Vernier scans in interaction points 2 and 6 carried out at the same physics fill is:

$$\begin{aligned} \text{IP 2} \quad \varepsilon_y &= 0.90 \pm 0.18 \text{ nm} \\ \text{IP 6} \quad \varepsilon_y &= 0.80 \pm 0.18 \text{ nm} \end{aligned}$$

and at the Vernier scans in interaction points 4 and 8 (carried out five days later) the vertical emittance is:

$$\begin{aligned} \text{IP 4} \quad \varepsilon_y &= 2.6 \pm 0.6 \text{ nm} \\ \text{IP 8} \quad \varepsilon_y &= 2.6 \pm 0.6 \text{ nm} \end{aligned}$$

Luminosity at interaction point 6 measured at many different vertical electrostatic separations is shown in fig. 3.22. A Gaussian fit gives a maximum luminosity at a vertical separation of $7.8 \pm 0.8 \mu\text{m}$ and a vertical emittance of $1.1 \pm 0.2 \text{ nm}$.

Vernier scans are carried out mainly during machine start-up and after long technical stop periods. The optimal electrostatic separation can change and frequent optimizations

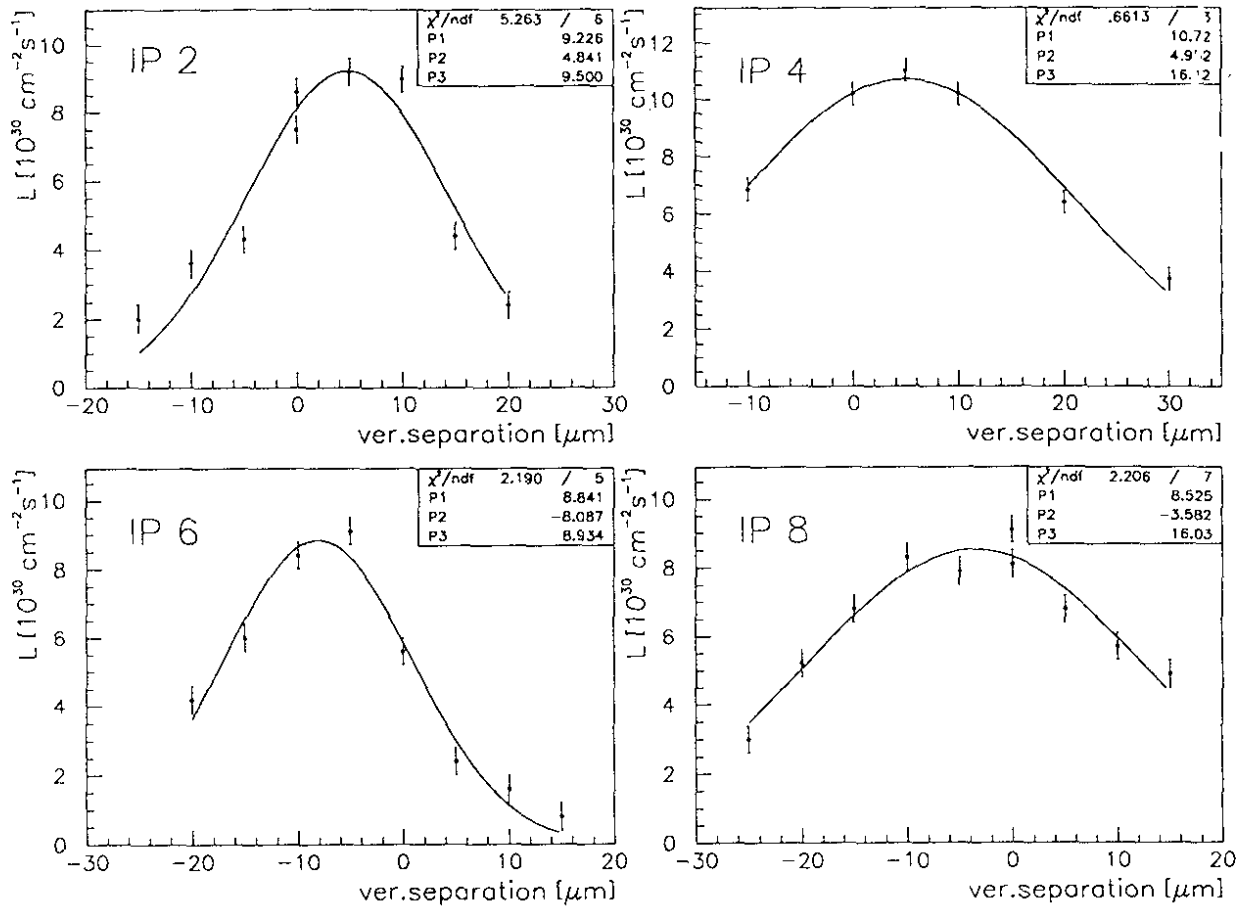


Figure 3.21: Luminosity at interaction points 2, 4, 6 and 8 as a function of the electrostatic separation. Data taken in April 1992. (Parameters of the Gaussian fit: P1 peak height, P2 mean, P3 sigma.)

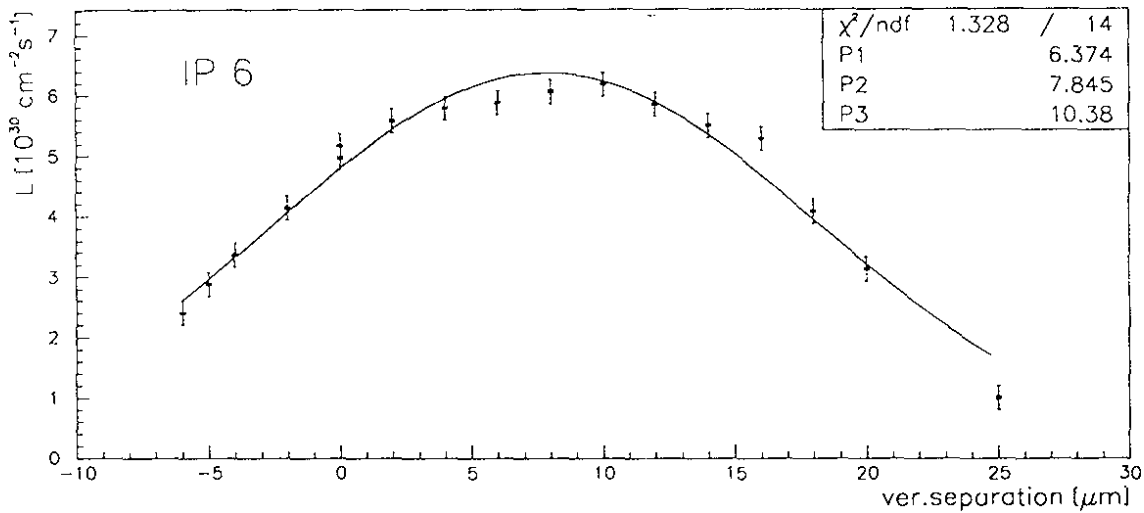


Figure 3.22: Luminosity at interaction point 6 as a function of electrostatic separation. Data taken by M. Lamont in October 1994. (Parameters of the Gaussian fit: P1 peak height, P2 mean, P3 sigma.)

are required. Since Vernier scans are made rather frequently to check the good beam overlap, a fast automatic procedure has been implemented in collaboration with members of the Control Group (CO), the Electrostatic Separators Section (BT/ES) and the Beam Instrumentation Group (BI). The good performance of the automatic Vernier scan together with the achievement of fast luminosity measurements has brought the total scan time required down to about 5 minutes per interaction point.

3.4.5 Luminosity acquisition time

The high rate of Bhabha scattering detected by the LEP luminosity monitors allows accurate luminosity measurement in a short time. Although the absolute calibration of these monitors is not accurate enough for precise physics measurements, they have shown to be very useful in the daily operation of the luminosity optimization of the collider.

The Bhabha scattering rate error (statistical) $\Delta \dot{N}_b$ is estimated by eq. (3.19) which can be approximated to

$$\Delta \dot{N}_b \simeq \Delta \dot{N}_{pair} = \sqrt{\frac{\dot{N}_{pair}}{\Delta t}} = \sqrt{\frac{\dot{N}_b + \dot{N}_{acc}}{\Delta t}}.$$

The relative luminosity error $\Delta \mathcal{L}/\mathcal{L}$ can be written

$$\frac{\Delta \mathcal{L}}{\mathcal{L}} = \frac{\Delta \dot{N}_b}{\dot{N}_b} = \sqrt{\frac{\dot{N}_b + \dot{N}_{acc}}{\dot{N}_b^2 \Delta t}} = \sqrt{\frac{1+r}{q \mathcal{L} \Delta t}} \quad (3.21)$$

where the detector acceptance q is defined as \dot{N}_b/\mathcal{L} and r is \dot{N}_{acc}/\dot{N}_b . Both quantities are roughly constant during the fills and the relative luminosity error is inversely proportional to $\sqrt{\mathcal{L}}$.

The acquisition time required by two monitors to obtain a relative error of 5% as a function of luminosity for particle background levels of 1992, 1993 and 1994 is shown in fig. 3.23.

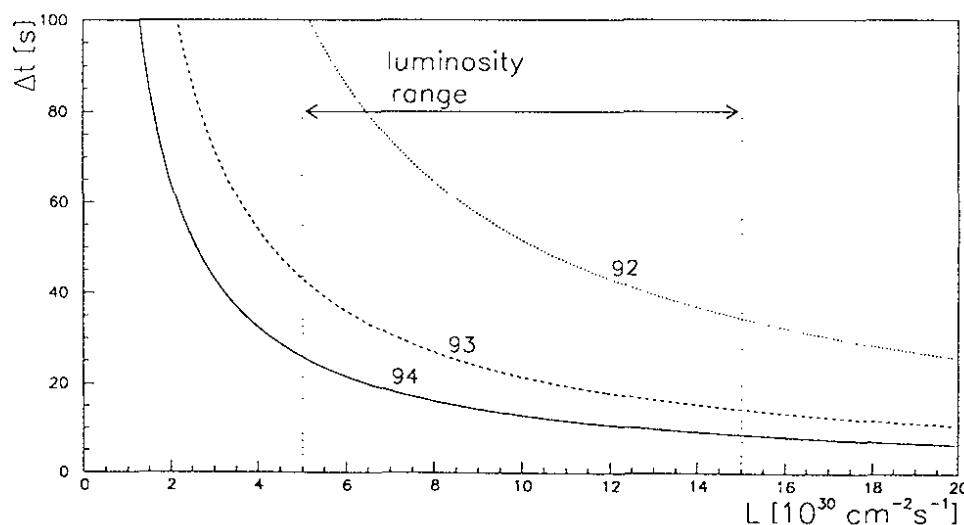


Figure 3.23: Acquisition time for a relative luminosity error of 5% for the particle background levels of 1992, 1993 and 1994 presented in table 3.4.

Luminosity measurement at LEP 2

The second phase of LEP (LEP 2), with electron and positron beams accelerated to twice the energy of present LEP, will bring new operational conditions for luminosity monitors.

The Bhabha scattering cross section (eq. 3.1) depends on the beam energy as $1/E^2$, such that the Bhabha scattering rate measured with LEP luminosity monitors will decrease by a factor 4 as the energy is doubled. The rate is expected to be even smaller due to new collimator position requirements. There are two optics envisaged for LEP 2: the $90^\circ/60^\circ$ and the $108^\circ/60^\circ$ (the first number is the horizontal phase advance per FODO cell and the second number is the vertical phase advance per FODO cell). Estimated collimator positions are $X_{col} = 42$ mm and 35 mm, respectively.

On the other hand, the expected luminosity (between 30 and $60 \cdot 10^{30} \text{ cm}^{-2}\text{s}^{-1}$) increases the Bhabha scattering rate and reduces the statistical error of the measurements (eq. 3.21).

Finally, a strong increase of accidental rate of particle background is expected, which can perturb seriously the monitors performance. The increase of accidental background rate is due to two effects: first, the number of off-momentum particles created in collisions with thermal photons could increase by a factor of two for the same beam current [44], and second, the current per bunch in collision can be increased as the beam-beam force is smaller at 90 GeV.

Luminosity monitor parameters at LEP 2 are compared to typical parameters at LEP 1 in 1994 in table 3.6. In this table, the coefficient q is calculated by

$$q = \frac{\dot{N}_b}{\mathcal{L}} = 3.8 \text{ } \mu\text{b} \left(\frac{32.7 \text{ mm}}{X_{col} + 2.7 \text{ mm}} \right)^{2.5} \left(\frac{45.6 \text{ GeV}}{E} \right)^2 . \quad (3.22)$$

The coincidence background rate \dot{N}_{acc} is obtained with eq. (3.11)

$$\dot{N}_{acc} = \frac{\dot{n}_{ext} \dot{n}_{int} I^2}{k_b f_{rev}}$$

where \dot{n}_{ext} and \dot{n}_{int} are the particle background rate (normalized to beam intensity) detected in the external and internal calorimeters, respectively, I is the beam intensity and the acquisition time Δt is deduced from eq. (3.21)

$$\Delta t = \frac{1}{(\Delta \mathcal{L}/\mathcal{L})^2} \frac{1+r}{q \mathcal{L}} . \quad (3.23)$$

The acquisition time required for luminosity measurements with a relative error of 5% for both optics at LEP 2 in the scenario described above is shown in fig. 3.24, and is compared with the equivalent acquisition time in 1992 and 1994 for LEP 1.

A comparative study made by G. von Holtey [45] between Bhabha scattering measurements and other luminosity measurement techniques shows that LEP luminosity monitors can still bring the fastest luminosity measurements.

3.4.6 Radiation damage on silicon detectors

Silicon detectors are rather resistant to radiation damage compared to other solid state detectors like scintillators, optical fibers, etc. This condition was required for LEP luminosity monitors since they are installed inside the vacuum chamber very close to the beams. The silicon detectors used for luminosity monitors are exposed to a high radiation of low energy

	LEP 1	LEP 2	
E [GeV]	45.6	90	90
optics [$\Delta\mu_x/\Delta\mu_y$ per cell]	90°/60°	90°/60°	108°/60°
X_{col} [mm]	32	42	35
$q = \dot{N}_b/\mathcal{L}$ [μb]	3.3	0.45	0.68
\dot{n}_{int} [Hz/mA]	150	300	300
\dot{n}_{ext} [Hz/mA]	1400	2800	2800
I [mA/bunch]	0.4	0.8	0.65
k_b (number of bunches per beam)	8	8	8
\mathcal{L} [$10^{30} \text{ cm}^{-2}\text{s}^{-1}$]	16	60	60
\dot{N}_b [Hz]	53	27	41
\dot{N}_{acc} [Hz]	25	380	250
$r = \dot{N}_{acc}/\dot{N}_b$	0.5	14	6
Δt [s] for $\Delta\mathcal{L}/\mathcal{L} = 5\%$ for two monitors per IP	8	160	50

Table 3.6: Luminosity monitor parameters for LEP 1 and LEP 2.

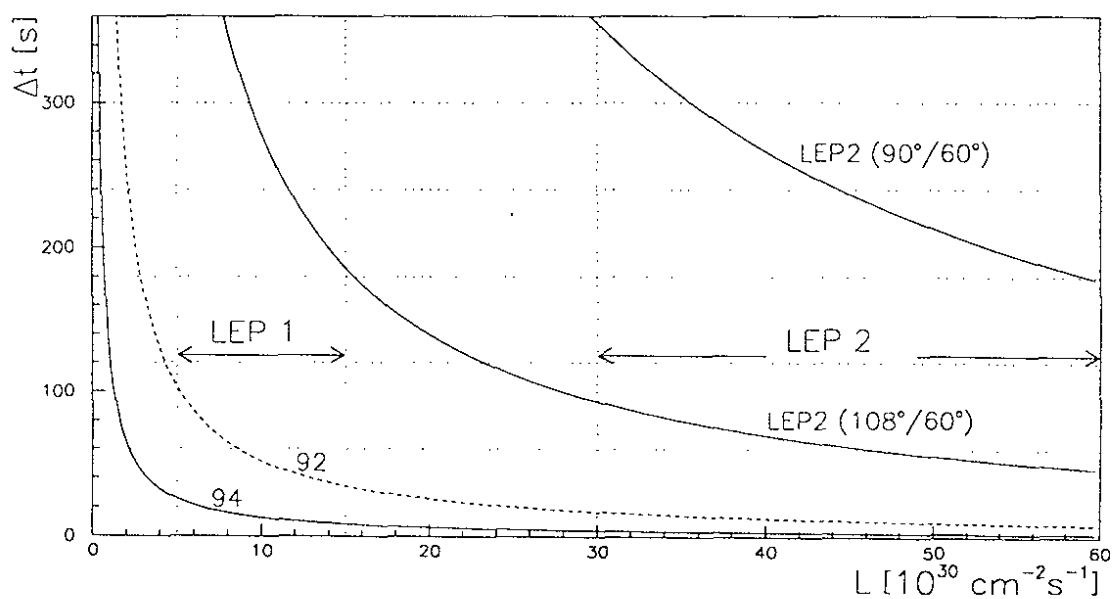


Figure 3.24: Acquisition time (eq. 3.23) for a relative luminosity error of 5% in LEP 1 and LEP 2 luminosity ranges. Changes are due to different background rates and collimator settings.

photons and of beam halo particles, and can eventually receive great amounts of beam particles due to beam instabilities.

Radiation affects silicon detectors by increasing the diode inverse bias currents. This effect on the Bhabha calorimeters was studied by G.P. Ferri et al. [26] using gamma rays from a ^{60}Co source. For a dose of 10^6 Gy the increase of measured inverse currents is less than a factor 10, while the charge collection efficiency remains unchanged.

The radiation dose received in five months of collider operation in 1993 was measured [46] by a set of 8 LiF^7 dosimeters inserted into the external calorimeter of monitor 1 at interaction point 2. They were located at the place of the F1 detector at six radiation lengths depth from the collimator surface (see fig. 3.2). The transverse position of the dosimeters is indicated in fig. 3.25. The numbers shown in this figure represent the doses measured in Gy, for the 5 months of exposure, with 1240 hours of beam at 45.6 GeV. During this time no change was observed in the inverse bias current of the silicon detectors and no effect on the counting rate was noticed.

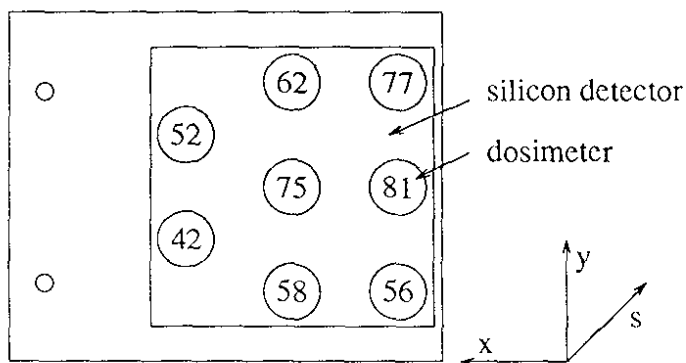


Figure 3.25: Doses measured in Gy at the external calorimeter of monitor 1 at interaction point 2.

Chapter 4

Phase and beta function measurement

The observation of coherent betatron oscillations provides accurate measurements of the optics functions in a storage ring. A well-known example is the measurement of the betatron tunes by analyzing the spectrum of the signal from a beam position monitor.

The phase of betatron oscillations can be measured at beam position monitors with the 1000-turns acquisition [47] provided by the beam orbit measurement system [48].

After a brief introduction, the method to measure the phase and the beta functions at beam position monitors and the calculation of these functions between monitors are described in section 4.2. The procedure to measure the phase of the oscillations using harmonic analysis is presented in section 4.3 and the error analysis of the phase and the beta functions is given in sections 4.4 and 4.5. This method is used in section 4.6 to measure changes of the beta and the phase functions due to quadrupole field changes, pretzel separation and energy sawtooth. Finally, changes of the phase function due to bunch current and beam energy variations are shown in sections 4.7 and 4.8.

4.1 Phase measurement at beam position monitors

The transverse oscillations of beam particles around the equilibrium orbit (closed orbit) due to the focusing effect of magnetic fields in a storage ring are called *betatron oscillations*. If the oscillation amplitude is relatively small, only linear terms of the magnetic fields have to be considered and the motion of particles is given by eq. (2.4), which is a solution of Hill's differential equation (eq. 2.2). If we observe these oscillations in successive turns or revolutions, then the tune Q_x , i.e. the number of oscillations per revolution, should be included in the phase argument of eq. (2.4)

$$x(s, i) = a\sqrt{\beta_x(s)} \cos[2\pi Q_x i + \mu_x(s) + \psi] \quad i = 0, \dots, N-1 \quad (4.1)$$

where β_x and μ_x are the beta and the phase functions, a and ψ are constants depending on initial conditions, $Q_x = \mu_x(C)/2\pi$ and C is the circumference of the ring. At a fixed point s_o the position of this particle at each revolution i is given by

$$x_o(i) = A \cos(2\pi q_x i + \phi) + x_{co}(s_o) \quad (4.2)$$

where q_x is the fractional part of the tune Q_x and $x_{co}(s)$ is the transverse position of the closed orbit. This equation represents the sampling of an oscillation of constant amplitude $A = a\sqrt{\beta_x(s_o)}$, with an initial phase $\phi = \mu_x(s_o) + \psi$ and a frequency $q_x f_{rev}$ (where f_{rev} is the revolution frequency).

At LEP, betatron oscillations are excited by modulating the field of ferrite dipole magnets (so-called shaker magnets) used by the Q-meter system [49]. The excitation is coherent, so that all particles oscillate with the same amplitude and at the same phase. Q-meter dipole magnets are 40 cm long and can provide a maximum beam deflection of about $3 \mu\text{rad}$ at the energy of 20 GeV and about $1.3 \mu\text{rad}$ at 45.6 GeV. Two vertical and two horizontal dipole magnets are installed at 122.4 m and 151.8 m respectively, on both sides from interaction point 1.

When betatron oscillations are excited coherently the center of the particle distribution follows the same trajectory as a single particle oscillating around the closed orbit (eq. 4.1). After some turns these oscillations are damped due to the longitudinal acceleration provided by the radio-frequency cavities and the effect of particle tune spread. Restoring the energy loss due to synchrotron radiation with the longitudinal acceleration of the radio-frequency cavities damps the transversal oscillation with a damping time of about 60 ms (675 turns). The spread of particle tunes in the beam creates differences in betatron oscillation phases and leads to the damping of coherent beam oscillations. In order to maintain beam particle oscillations in a coherent mode the beam is excited continuously with a frequency which is close to the fractional part of the tune times the revolution frequency. The excitation is maintained for some 10 or 20 seconds in order to allow beam position measurements for about 1000 turns, because the acquisition software of beam position monitors is not synchronized to the excitation dipole magnet.

The amplitude observed at each beam position monitor is proportional to the square root of the beta function

$$A = a S_i \sqrt{\beta_x(s)}$$

with a constant factor a for all monitors and the scaling factor S_i of each monitor. This provides a relative value of the beta function at the beam position monitors and its accuracy depends on the individual calibration of the monitors and their electronics, therefore it is not used in this thesis to determine the beta function.

If the acquisition of position monitors is synchronized within a revolution time, we obtain the measurement of the phase difference between any two beam position monitors k and $k+1$ from the difference between phases ϕ_k and ϕ_{k+1} of betatron oscillations measured for 1000 turns

$$\mu(s_{k+1}) - \mu(s_k) = \phi_{k+1} - \phi_k \quad ,$$

where s_k is the position of the monitor k and s_{k+1} is the position of the monitor $k+1$.

The phase measurements of coherent beam oscillations have systematic errors which are function of the longitudinal size of the beam. At LEP, this systematic error is negligible because the bunch length is only of about 1 cm. The acquisition of beam position monitors is self-triggered by the bunch passage with an error of about 30 picoseconds. The contribution of position measurement errors on the measured phases will be discussed in section 4.4.

The measured phases provide the following data:

- The perturbation of the phase and of the beta functions can be obtained with a fit of a modulation with twice the betatron frequency (see eq. 2.14) to the phase of about 15 monitors [50]. This is not studied here.
- The phase μ , the alpha and the beta functions can be obtained from the phase advance measured between three beam position monitors using the transport matrix [51]. The procedure is described in the following section and its accuracy is discussed in sections 4.4 and 4.5.

4.2 Measurement of the Twiss functions

Beta function measurement at beam position monitors

The optics functions β , α and μ of a given storage ring are calculated from quadrupole gradients and the layout of magnetic elements using programs like MAD [2]. If the measured phase advance $\phi'_{12} = \phi'_2 - \phi'_1$ ¹ between two beam position monitors at s_1 and s_2 is different from the phase advance ϕ_{12} calculated with MAD, then the beta function β' and the alpha function α' are also different from β and α . If we suppose that quadrupole gradients and the layout of magnetic elements are perfectly known between s_1 and s_2 (that is to assume the perturbation is outside the interval $[s_1, s_2]$), then eq. (2.7) is valid for β'_1 , α'_1 and ϕ'_{12}

$$\frac{a_{11}}{a_{12}} = \frac{1}{\beta'_1} (\cot \phi'_{12} + \alpha'_1) \quad (4.3)$$

where a_{11} and a_{12} are the elements of the first row of the transport matrix A from monitor 1 to monitor 2. This equation has two unknown variables: β'_1 and α'_1 . A solution can be found using a second equation which relates β'_1 and α'_1 to the measured phase advance ϕ'_{13} between monitor 1 at s_1 and a third beam position monitor located at s_3 .

$$\frac{c_{11}}{c_{12}} = \frac{1}{\beta'_1} (\cot \phi'_{13} + \alpha'_1)$$

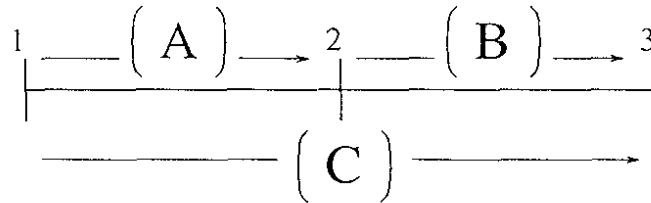
where c_{11} and c_{12} are elements of the transport matrix C from monitor 1 to monitor 3. The system of equations to solve is

$$\begin{cases} \beta'_1 \frac{a_{11}}{a_{12}} = \cot \phi'_{12} + \alpha'_1 \\ \beta'_1 \frac{c_{11}}{c_{12}} = \cot \phi'_{13} + \alpha'_1 \end{cases}$$

The solution for β'_1 is

$$\begin{aligned} \beta'_1 &= \frac{\cot \phi'_{12} - \cot \phi'_{13}}{(a_{11}/a_{12}) - (c_{11}/c_{12})} \\ &= \frac{a_{12}c_{12}}{a_{11}c_{12} - a_{12}c_{11}} (\cot \phi'_{12} - \cot \phi'_{13}) \end{aligned} \quad (4.4)$$

Let B be the transport matrix from monitor 2 to monitor 3, then $C = B \times A$.



By calculating

$$\begin{aligned} a_{11}c_{12} - a_{12}c_{11} &= a_{11}(b_{11}a_{12} + b_{12}a_{22}) - a_{12}(b_{11}a_{11} + b_{12}a_{21}) \\ &= b_{12}(a_{11}a_{22} - a_{12}a_{21}) \\ &= b_{12} \det(A) = b_{12} \end{aligned}$$

¹The quantities β' , α' and ϕ' refer to measurement values in contrast with β , α , ϕ which refer to design values.

eq. (4.4) can be written as

$$\beta'_1 = \frac{a_{12}c_{12}}{b_{12}}(\cot \phi'_{12} - \cot \phi'_{13}) . \quad (4.5)$$

Eq. (2.7) can also be applied to the measured phase advance ϕ'_{23} between monitor 2 and 3

$$\beta'_2 \frac{b_{11}}{b_{12}} = \cot \phi'_{23} + \alpha'_2$$

and eq. (2.8) can be applied to the measured phase advance ϕ'_{12} between monitor 1 and 2

$$\beta'_2 \frac{a_{22}}{a_{12}} = \cot \phi'_{12} - \alpha'_2 .$$

Both equations form a new system of equations solved by

$$\begin{aligned} \beta'_2 &= \frac{\cot \phi'_{12} + \cot \phi'_{23}}{(a_{22}/a_{12}) + (b_{11}/b_{12})} \\ &= \frac{a_{12}b_{12}}{c_{12}}(\cot \phi'_{12} + \cot \phi'_{23}) . \end{aligned} \quad (4.6)$$

Finally, the value of the beta function at the 3rd beam position monitor is obtained from

$$\begin{cases} \beta'_3 \frac{b_{22}}{b_{12}} = \cot \phi'_{23} - \alpha'_3 \\ \beta'_3 \frac{c_{22}}{c_{12}} = \cot \phi'_{13} - \alpha'_3 \end{cases}$$

which has the solution

$$\begin{aligned} \beta'_3 &= \frac{\cot \phi'_{23} - \cot \phi'_{13}}{(b_{22}/b_{12}) - (c_{22}/c_{12})} \\ &= \frac{b_{12}c_{12}}{a_{12}}(\cot \phi'_{23} - \cot \phi'_{13}) \end{aligned} \quad (4.7)$$

Replacing a_{11}/a_{12} in eq. (4.4) by $(\cot \phi_{12} + \alpha_1)/\beta_1$ according to eq. (2.7) and c_{11}/c_{12} by $(\cot \phi_{13} + \alpha_1)/\beta_1$, the expression of β'_1 yields the ratio between $\cot \phi'_{12} - \cot \phi'_{13}$ and the same quantity obtained with MAD:

$$\beta'_1 = \beta_1 \frac{\cot \phi'_{12} - \cot \phi'_{13}}{\cot \phi_{12} - \cot \phi_{13}} . \quad (4.8)$$

Using

$$\cot x \pm \cot y = \frac{\sin(y \pm x)}{\sin x \sin y} \quad (4.9)$$

allows to write

$$\beta'_1 = \beta_1 \frac{\sin \phi'_{23} \sin \phi_{12} \sin \phi_{13}}{\sin \phi_{23} \sin \phi'_{12} \sin \phi'_{13}} .$$

Doing similarly for eq. (4.6) we obtain

$$\begin{aligned} \beta'_2 &= \beta_2 \frac{\cot \phi'_{12} + \cot \phi'_{23}}{\cot \phi_{12} + \cot \phi_{23}} \\ &= \beta_2 \frac{\sin \phi'_{13} \sin \phi_{12} \sin \phi_{23}}{\sin \phi_{13} \sin \phi'_{12} \sin \phi'_{23}} \end{aligned}$$

and for eq. (4.7) we obtain

$$\begin{aligned}\beta'_3 &= \beta_3 \frac{\cot \phi'_{23} - \cot \phi'_{13}}{\cot \phi_{23} - \cot \phi_{13}} \\ &= \beta_3 \frac{\sin \phi'_{12} \sin \phi_{23} \sin \phi_{13}}{\sin \phi_{12} \sin \phi'_{23} \sin \phi'_{13}}.\end{aligned}$$

The solutions for the function alpha at s_1 , s_2 and s_3 are derived in Appendix D. Note that six values of β' and α' at s_1 , s_2 and s_3 have been obtained from the three phase measurements ϕ'_1 , ϕ'_2 and ϕ'_3 , or, more precisely, from the measured phase advance ϕ'_{12} , ϕ'_{23} and ϕ'_{13} .

Interpolation of the Twiss functions between beam position monitors

The calculation of β' and α' at the three beam position monitors using above equations assumes that the magnetic gradients used in the transfer line model between beam position monitors 1 and 3 are perfect. In this case, it is valid to interpolate the values of the measured Twiss functions to any point between beam position monitors 1 and 3 using for instance the Twiss transfer matrix given in eq. (2.9). To simplify the equations, we have developed the expressions of $\phi'(s)$, $\beta'(s)$ and $\alpha'(s)$ as functions of the measured ϕ'_{12} , ϕ'_{23} , β'_1 and α'_1 .

Let s be the longitudinal coordinate at a point between s_1 and s_3 . The measured phase advance $\phi'(s)$ between s_1 and s is deduced from eq. (4.3) which can be written as

$$\cot \phi'(s) = \beta'_1 \frac{m_{11}(s)}{m_{12}(s)} - \alpha'_1$$

where $m_{11}(s)$ and $m_{12}(s)$ are elements of the transport matrix $M(s)$ from s_1 to s . Using eq. (2.7), we replace the fraction $m_{11}(s)/m_{12}(s)$ in terms of β_1 and α_1 to get

$$\cot \phi'(s) = \frac{\beta'_1}{\beta_1} [\cot \phi(s) + \alpha_1] - \alpha'_1$$

where $\phi(s) = \mu(s) - \mu(s_1)$. Replacing now the value of β'_1/β_1 by eq. (4.8) and α'_1 by eq. (D.4), we obtain $\phi'(s)$ as a function of ϕ'_{12} , ϕ'_{13} , $\phi(s)$, ϕ_{12} and ϕ_{13}

$$\cot \phi'(s) = \frac{[\cot \phi(s) - \cot \phi_{13}] \cot \phi'_{12} - [\cot \phi(s) - \cot \phi_{12}] \cot \phi'_{13}}{\cot \phi_{12} - \cot \phi_{13}}. \quad (4.10)$$

Using eq. (2.11), the measured beta function $\beta'(s)$ can be expressed as a function of the above expression of $\cot \phi'(s)$

$$\beta'(s) = \frac{m_{12}^2(s)}{\beta'_1 \sin^2 \phi'(s)} = \frac{m_{12}^2(s)}{\beta'_1} (\cot^2 \phi'(s) + 1) \quad (4.11)$$

where $m_{12}(s)$ can be replaced by the second coefficient of the matrix of eq. (2.6)

$$\beta'(s) = \frac{\beta(s) \beta_1 \sin^2 \phi(s)}{\beta'_1 \sin^2 \phi'(s)} = \beta(s) \frac{\beta_1 (\cot^2 \phi'(s) + 1)}{\beta'_1 (\cot^2 \phi(s) + 1)}.$$

Finally, the expression of the measured alpha function is

$$\alpha'(s) = \cot \phi'(s) - \beta'(s) \frac{m_{22}(s)}{m_{12}(s)}$$

which can be written in terms of $\beta(s)$, $\alpha(s)$ and $\cot \phi(s)$

$$\alpha'(s) = \cot \phi'(s) + \frac{\beta'(s)}{\beta(s)} [\alpha(s) - \cot \phi(s)] \quad . \quad (4.12)$$

The values of the phase, the beta and the alpha functions can be interpolated to any point between two beam position monitors. The expressions of $\phi'(s)$, $\beta'(s)$ and $\alpha'(s)$ have been written as functions of the measured phase function at three monitors.

4.3 Measurement of the phase and the amplitude of betatron oscillations

At LEP, coherent betatron oscillations can be excited by modulating the field of the Q-meter dipole magnets at the frequency of the tune times the revolution frequency. These oscillations are sampled turn by turn at each beam position monitor for 1024 revolutions. This number is the maximum memory available by the local processor to store beam position data.

An example of data obtained for a vertically excited beam is given in fig. 4.1, where the horizontal and vertical beam positions at one monitor are shown for 50 turns together with the frequency spectrum (FFT) for 1024 turns.

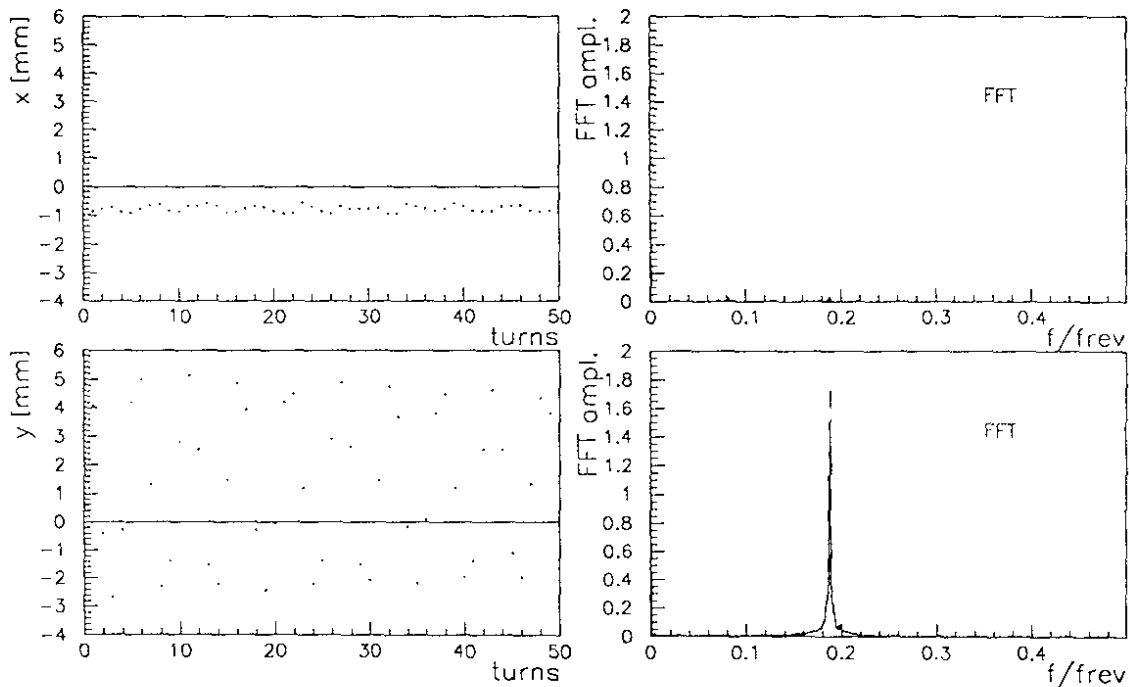


Figure 4.1: Example of a multiturn beam position acquisition for a vertically excited beam. Left: horizontal (top) and vertical (bottom) beam positions measured at a single beam position monitor turn by turn. Right: the frequency spectrum (the Fast Fourier Transform's amplitude) of each signal (for 1024 turns).

Harmonic analysis of betatron oscillations

The amplitude A and the initial phase ϕ of beam oscillations at each beam position monitor are obtained using a *harmonic analysis* based on the function

$$\mathcal{F}(\omega) = \sum_{i=0}^{N-1} x_i e^{j\omega i} \quad (4.13)$$

where N is the number of samples or turns and the values $\{x_i\}_{i=0}^{N-1}$ are the measured beam positions. The values of this function for $\omega = n/N$ for $n = 0, 1, \dots, N-1$ correspond to twice the Discrete Fourier Transform applied to the vector $\{x_i\}_{i=0}^{N-1}$.

The function $\mathcal{F}(\omega)$ can be written as $C(\omega) + jS(\omega)$, where $C(\omega)$ and $S(\omega)$ are real numbers given by

$$C(\omega) = \sum_{i=0}^{N-1} x_i \cos(\omega i) \quad S(\omega) = \sum_{i=0}^{N-1} x_i \sin(\omega i) \quad .$$

The amplitude A and the phase ϕ of $\mathcal{F}(\omega)$ are given by

$$A(\omega) = \frac{2\sqrt{C(\omega)^2 + S(\omega)^2}}{N} \quad \phi(\omega) = -\arctan \left[\frac{S(\omega)}{C(\omega)} \right] \quad .$$

If the vector $\{x_i\}_{i=0}^{N-1}$ is replaced by eq. (4.2), the amplitude $A(\omega)$ and the phase $\phi(\omega)$ at the harmonic $\omega = 2\pi q_x$ correspond to the parameters A and ϕ of eq. (4.2). This is demonstrated in appendix E.

Example of a phase measurement

As an example, the difference between a measurement of the vertical phase and the vertical phase function calculated with the program MAD is shown in fig. 4.2. The measured vertical fraction of the tune was $q = 0.224$ and the positron bunch number 1 was excited with the frequency of $0.224 \times f_{rev}$ Hz.

The phases obtained by harmonic analysis at some position monitors which have a trigger delayed have to be corrected by $\pm 2\pi q$. The trigger to the BOM electronics A22 is delayed by one turn (A refers to arc and 22 indicates that is located on the left side of interaction point 2) and the phase data obtained at the beam position monitors of the A22 electronics must be corrected by $-2\pi q$, which is the phase delay for one turn. The bunch measured is the positron bunch 1 and the acquisition starts with the L15 electronics (located in the straight section on the left side of interaction point 1). The phase measured at the monitors of the L15 electronics must be corrected by $+2\pi q$, since their acquisition started one turn earlier. Both corrections to the raw phase data are indicated in fig. 4.2. If the phases are measured with another bunch, the corrections that must be applied are given in appendix F.

Example of beta and alpha function measurements

Three beam position monitors located at 756.7, 835.7 and 914.7 m on the right side of interaction point 1 are selected. The amplitude A and the phase ϕ' of the oscillations recorded at each monitor are shown in table 4.1. The vertical phase advance between these three beam position monitors calculated with MAD for the optics k05p46v3 gives $\phi_{12} = \phi_{23} = 60^\circ$, while the measured ones are $\phi'_{12} = 61.54^\circ$ and $\phi'_{23} = 62.73^\circ$.

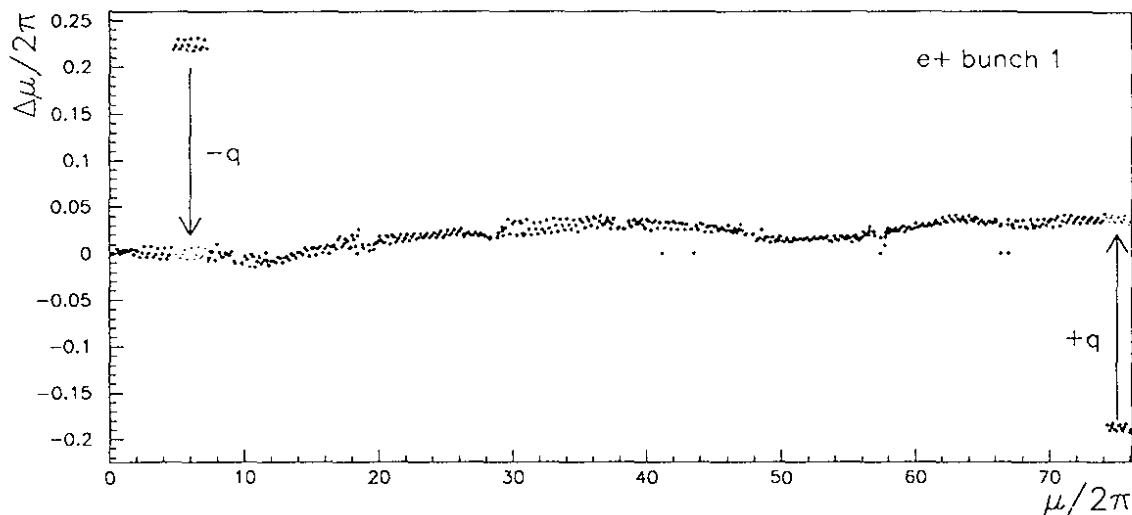


Figure 4.2: Difference between phase measurements at beam position monitors done on 4th June 1994 at 10:40 with the positron bunch 1 of $50 \mu\text{A}$ at 20 GeV and the phase function calculated with MAD for the optics k21p20v3. Due to trigger delays the phase at the beam position monitors of the A22 electronics (right) must be corrected by $-2\pi q$ and the phase at the monitors of the L15 electronics (left) must be corrected by $+2\pi q$. Both raw phase (big dots) and corrected phase (small dots) are shown. The positive difference between the measured and the nominal phase corresponds to the difference between the tune $q = 0.224$ and the nominal tune $q = 0.194$.

n	monitor	position from IP 1	A (mm)	ϕ'
1	PU.QD26.R1	756.71 m	4.1 mm	148.05°
2	PU.QD28.R1	835.71 m	3.9 mm	209.59°
3	PU.QD30.R1	914.71 m	4.1 mm	272.32°

Table 4.1: Oscillation amplitude A and phase ϕ' at three adjacent beam position monitors. The treatment of phase errors is given in section 4.4 and shown in table 4.6. The name of the monitor indicates its location near the quadrupole magnet QDxx counting from the right side of interaction point 1 (R1).

The values of the beta and the alpha functions shown in table 4.2 are calculated using eqs. (4.5) and (D.1) for the beam position monitor 1, using eqs. (4.6) and (D.2) for monitor 2, and using eqs. (4.7) and (D.3) for monitor 3. The transport matrices A from monitor 1 to 2, B from monitor 2 to 3 and C from monitors 1 to 3 are

$$A = B = \begin{pmatrix} -1.3555 & 130.14 \\ -0.03222 & 2.3558 \end{pmatrix} \quad C = \begin{pmatrix} -2.3559 & 130.18 \\ -0.03223 & 1.3564 \end{pmatrix}.$$

The error of the alpha and beta measurements of this example are given in table 4.6 at the end of section 4.4.

n	β (m)	β' (m)	α	α'
1	150.2	159.3	-2.142	-2.201
2	150.3	137.6	-2.143	-1.949
3	150.3	155.8	-2.142	-2.305

Table 4.2: Design and measured (primed) beta and alpha functions at three adjacent beam position monitors. The treatment of errors is given in section 4.4 and the values are presented in table 4.6.

The beta function $\beta'(s)$ and the phase function $\phi'(s)$ between monitor 1 and 3 are calculated using eqs. (4.11) and (4.10) in which the measured values ϕ'_{12} and ϕ'_{23} are used. The $\beta'(s)$ and $\phi'(s)$ obtained are plotted together with the theoretical $\beta(s)$ and $\phi(s)$ in fig. 4.3. The origin of the phase function is taken at the beam position monitor 1, so $\phi'(s_1) = \phi(s_1) = 0$.

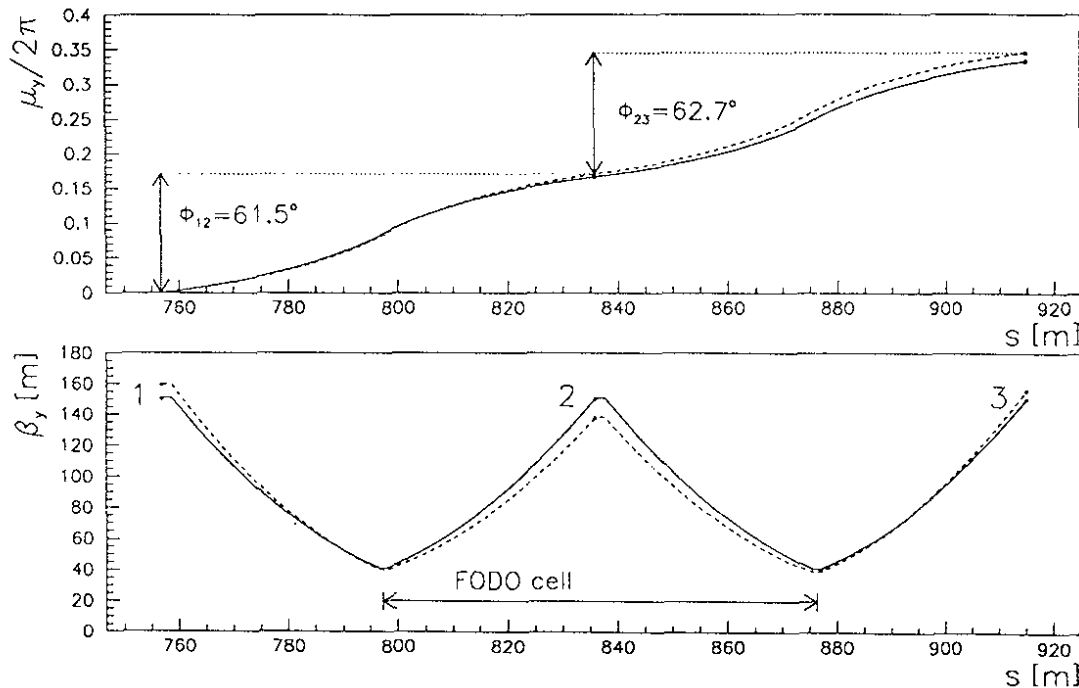


Figure 4.3: The measured vertical phase and beta functions using eqs. (4.10) and (4.11) are shown with dashed lines along the transport line between three beam position monitors. The measurement errors are shown in fig. 4.18. The results from MAD simulation with optics k05p46v3 are shown with full line.

4.4 Error analysis of phase measurements

Dependence of the phase on the harmonic analysis frequency

A precise determination of the oscillation frequency is needed for the calculation of the phase. The oscillation frequency of the beam is imposed by the excitation frequency of the dipole magnet. However, the frequency generated by the power supply of the shaker magnet may differ from the selection made by the user due to the truncation of the data sent to the microprocessor which controls the shaker magnet. This difference can be up to $2.5 \cdot 10^{-4} \times f_{rev}$ and has not yet been understood. In order to obtain the real frequency, we search for the value of ω corresponding to the maximum amplitude $A(\omega)$ of the function of $\mathcal{F}(\omega)$. Results of the harmonic analysis versus frequency applied to a horizontal oscillation are shown in fig. 4.4. For this example, the maximum amplitude A is found at the oscillation frequency of $f = 0.26708 \times f_{rev}$, giving a phase $\phi = 104.45^\circ$ rad. At this point, the value of ϕ changes by about 2° for a frequency shift of $\Delta f = 10^{-5} \times f_{rev}$ and errors in the frequency determination could lead to significant systematic phase errors.

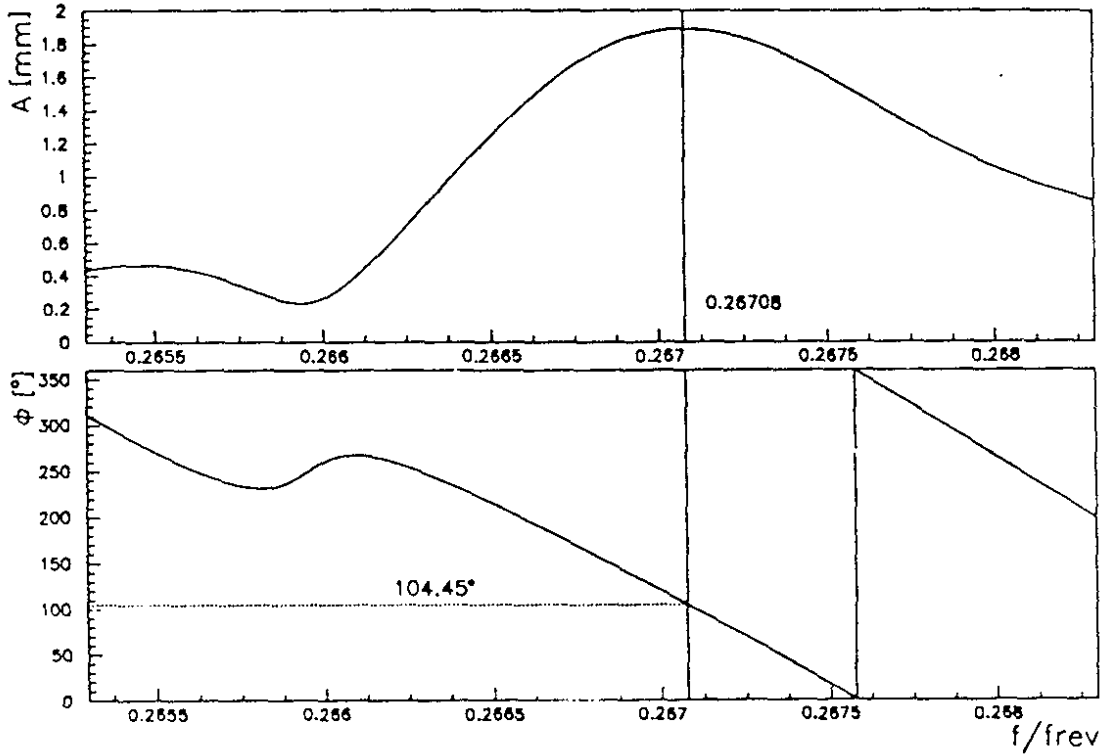


Figure 4.4: Harmonic analysis amplitude A (upper plot) and phase ϕ (lower plot) as function of the frequency for a horizontal oscillation measured at the beam position monitor PU.QL15.R1 on Sept. 3rd 1994.

It has been observed that the change of ϕ due to a frequency deviation in the harmonic analysis is almost equal for all beam position monitors in a single measurement. The relative change in phase between monitors for the same frequency shift is about 100 times smaller than the absolute phase change at each monitor. For the previous example, the change of the phase ϕ for a frequency shift of $\Delta f = 10^{-5} \times f_{rev}$ is 2° , while the phase difference between two monitors changes by less than 0.03° . The relative phase changes between beam position monitors due to a certain frequency shift are smaller for oscillations with high amplitude. An example is given in fig. 4.5, where the histograms of the phase change for all beam position monitors caused by a frequency shift of $\Delta f = 10^{-5} \times f_{rev}$ of the harmonic analysis are shown.

The first histogram corresponds to a measurement with a vertical oscillation amplitude of 1.9 mm and the second histogram is for a measurement with a vertical amplitude of 3.7 mm. To compare both measurements, the range of the scales in both plots is the same. The r.m.s. deviation of the phase change for the measurement with 1.9 mm amplitude is $\sigma_1 = 0.0049^\circ$ and for the measurement with 3.7 mm is $\sigma_2 = 0.0024^\circ$.

In order to keep systematic phase errors one order of magnitude lower than 0.1° , a frequency determination of about 10^{-5} is needed.

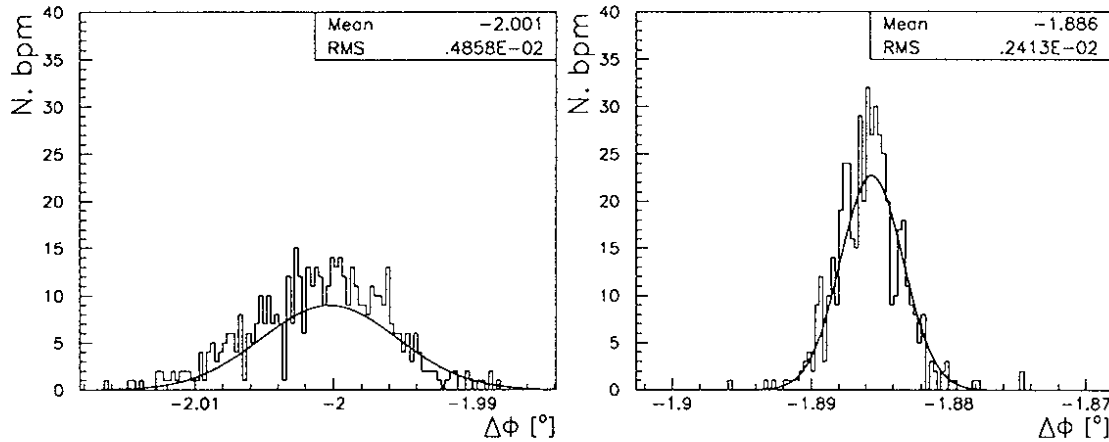


Figure 4.5: Histograms of the phase change at about 500 beam position monitors for frequency shift of $\Delta f = 10^{-5} \times f_{rev}$ in a measurement with average vertical amplitude 1.9 mm (left) and in a measurement with average vertical amplitude 3.7 mm (right) taken on Sept. 3rd 1994.

Frequency analysis

The frequency used for harmonic analysis is the average of the frequencies where the maximum amplitude $A(\omega)$ is found at each beam position monitor. The precision in the determination of the oscillation frequency depends on the amplitude of the oscillations. As an example, three vertical oscillations with amplitudes of 0.41, 1.9 and 3.7 mm are taken. The histograms of the frequencies found at all monitors for these three measurements are shown in fig. 4.6.

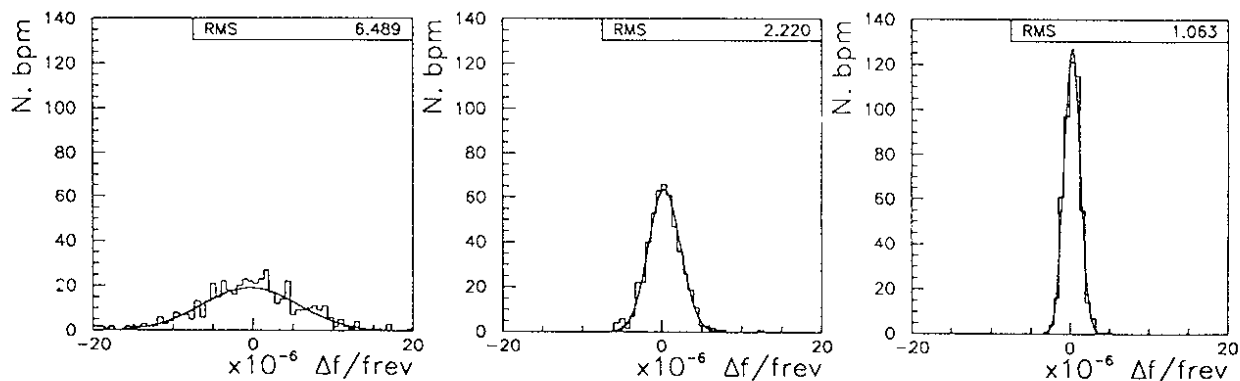


Figure 4.6: Histograms of frequencies measured from all beam position monitors (centered at the mean frequency) for three measurements of average vertical amplitudes 0.41 mm (right), 1.9 mm (middle) and 3.7 mm (left) taken on Sept. 3rd 1994. The mean frequency values are given in table 4.3.

The oscillation amplitude A , the mean frequency and the frequency r.m.s. from all monitors, for these three measurements are given in table 4.3. The mean phase shift and the

relative phase r.m.s. deviation due to a frequency shift of $\Delta f = 10^{-5} \times f_{rev}$ are also included in this table.

time	A [mm]	mean frequency f/f_{rev}	r.m.s. freq. σ_f/f_{rev}	for $\Delta f = 10^{-5} \times f_{rev}$	
				$\Delta\phi$ [°]	$\sigma_{\Delta\phi}$ [°]
7:48	0.41	0.1840876	$6.5 \cdot 10^{-6}$	-2.3	0.020
7:52	1.9	0.1858083	$2.2 \cdot 10^{-6}$	-2.0	0.005
8:04	3.7	0.1880224	$1.1 \cdot 10^{-6}$	-1.9	0.002

Table 4.3: Oscillation amplitude A , mean frequency and frequency r.m.s. obtained from all monitors. The three measurements were taken on Sept. 3rd 1994. The frequency dependence of the phase is given as the mean phase shift $\Delta\phi$ and the relative phase r.m.s. deviation $\sigma_{\Delta\phi}$ for a frequency change of a $\Delta f = 10^{-5} \times f_{rev}$.

In fig. 4.7, the r.m.s. spread of the frequencies found at all beam position monitors is plotted against the average oscillation amplitude.

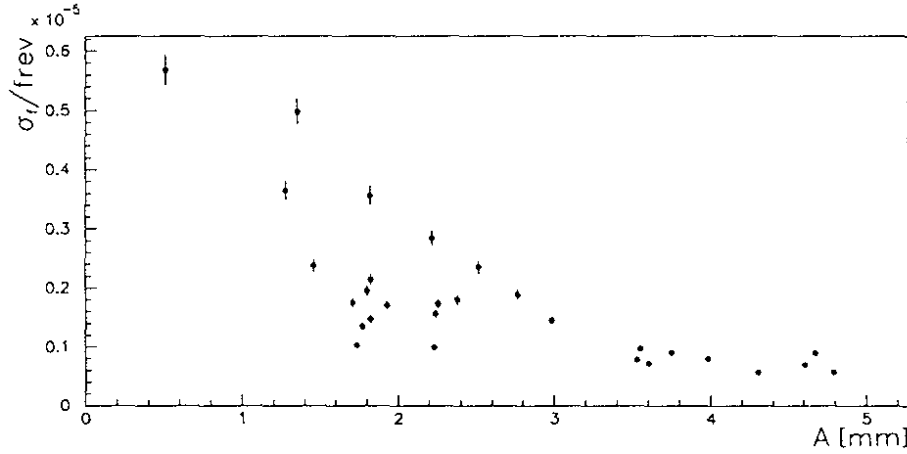


Figure 4.7: Frequency r.m.s versus oscillation amplitude for 29 vertical measurements taken in 1994. Error bars are calculated using $\sigma/(2n)^{1/2}$, where n is 250, the number of monitors in the bending sections.

It is possible to obtain the frequency with an accuracy of $3 \cdot 10^{-6} \times f_{rev}$ when the oscillation amplitude is about 2 mm or higher.

Position error contribution to the phase

Beam position measurement errors affect the analysis of the amplitude A and the phase ϕ of the oscillations. Most beam position monitors are equipped with narrow band electronics which have two uncorrelated sources of noise:

- Numerical noise from the analog digital conversion, which has a standard deviation of $1/\sqrt{12}$ LSB (Least Significant Bit)
- Electronic noise with a measured r.m.s. of $\sigma = 1/2$ LSB.

The LSB is equivalent to 0.15 mm in the vertical plane (0.21 mm in the horizontal plane) for narrow band beam position monitors. The total standard deviation is

$$\sigma \approx \sqrt{\sigma_{\text{Num.Error}}^2 + \sigma_{\text{Electr.Noise}}^2} = 0.09 \text{ mm} .$$

The estimated error on A and ϕ due to position errors of the monitors can be calculated by error propagation (see appendix E)

$$\sigma_A = \sqrt{\frac{2}{N}} \sigma, \quad \sigma_\phi = \frac{1}{A} \sqrt{\frac{2}{N}} \sigma. \quad (4.14)$$

Both quantities are proportional to $\sqrt{1/N}$ where N is the number of samples or turns. Moreover, the error of the phase σ_ϕ is inversely proportional to the oscillation amplitude. The measurement error of the phase advance between two monitors with same oscillation amplitude A is:

$$\sigma_{\Delta\phi} = \frac{2}{A} \sqrt{\frac{1}{N}} \sigma. \quad (4.15)$$

Results

The error of phase measurements has been obtained by comparing two measurements carried out with a very short delay between them, while the parameters of the machine, like tunes and currents, remained unchanged. As an example, the difference between two phase measurements made with oscillation amplitudes of about 4 mm is shown in fig. 4.8, which gives a phase difference r.m.s. of 0.17° . The theoretical r.m.s. error on the phase difference is given by eq. (4.15) for $A = 4$ mm and $\sigma = 0.09$ mm, which gives 0.08° , two times smaller than the phase difference r.m.s. from the measurements.

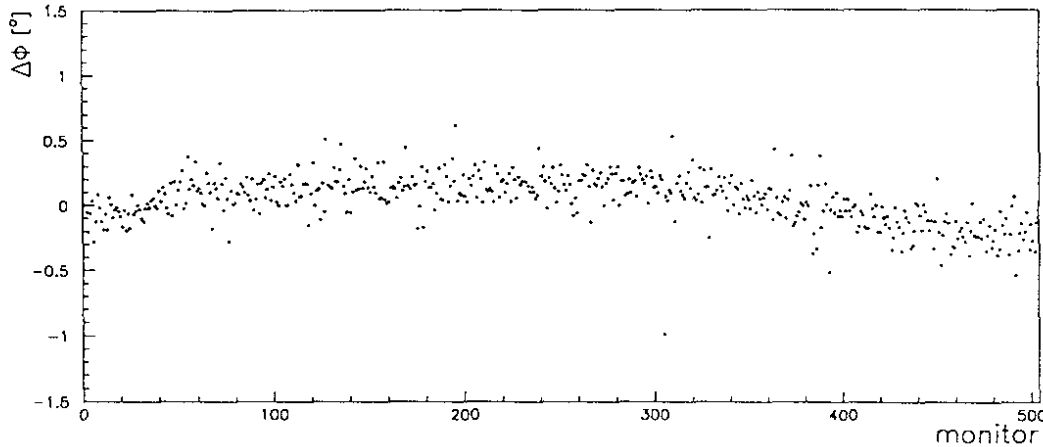


Figure 4.8: Difference monitor by monitor between two measurements of the vertical phase taken on June 4th 1994 at 11:12 and 11:20. The oscillations amplitude was about 4 mm for both measurements.

Some phase measurements give different results as for example the comparison shown in fig. 4.9. between measurements of vertical oscillation amplitudes of 1.8 mm. The difference r.m.s. between these two phase measurements with 1.8 mm vertical amplitude is 0.7° (where the effect seen in fig. 4.9 is included) and the expected r.m.s. is 0.18° , a factor of 4 smaller.

This phase perturbation in the measurements is not a problem for the measurement of the phase advance between consecutive beam position monitors. In the previous case of two measurements with vertical amplitudes of 1.8 mm, the comparison between the phase advance measurements gives an r.m.s. of 0.4° and the expected one is given by:

$$\sigma_{\Delta\phi_{12}} = \sqrt{2} \sigma_{\Delta\phi} = 0.25^\circ.$$

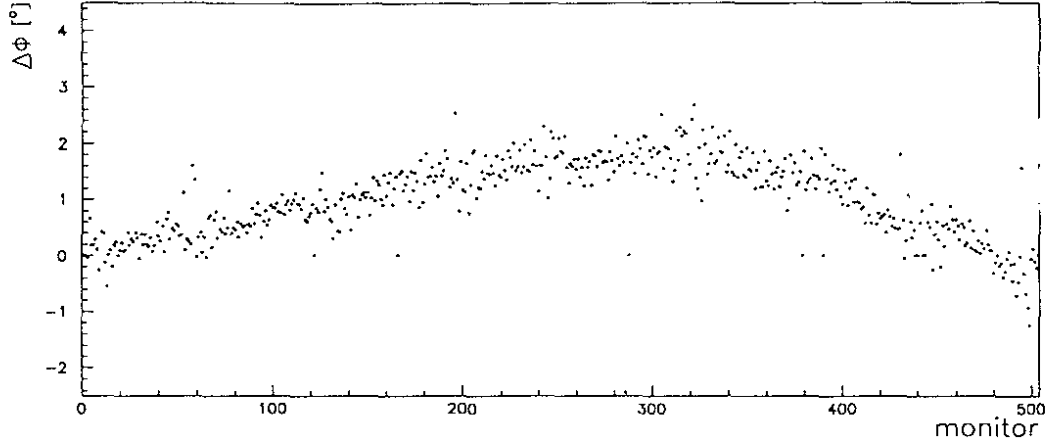


Figure 4.9: Difference monitor by monitor between two vertical phase measurements with oscillations amplitude of 1.8 mm taken on Sept. 3rd 1994 at 5:43 and 5:48.

The theoretical difference between phase advance measurements with different amplitude is:

$$\begin{aligned}\sigma_{\Delta\phi_{12}} &= \sqrt{\sigma_{\Delta\phi(1)}^2 + \sigma_{\Delta\phi(2)}^2} \\ \sigma_{\Delta\phi_{12}} &= 2\sqrt{\left(\frac{1}{A_1^2} + \frac{1}{A_2^2}\right) \frac{1}{N} \sigma} \quad (4.16)\end{aligned}$$

where (1) indicates the first measurement with amplitude A_1 and (2) indicates the second measurement with amplitude A_2 .

To check the expression of the phase error σ_ϕ given in eq. (4.14), the difference between phase advance measurements for six pairs of measurements are shown in fig. 4.10 and the results are presented in table 4.4. Results of the comparison between phase advance mea-

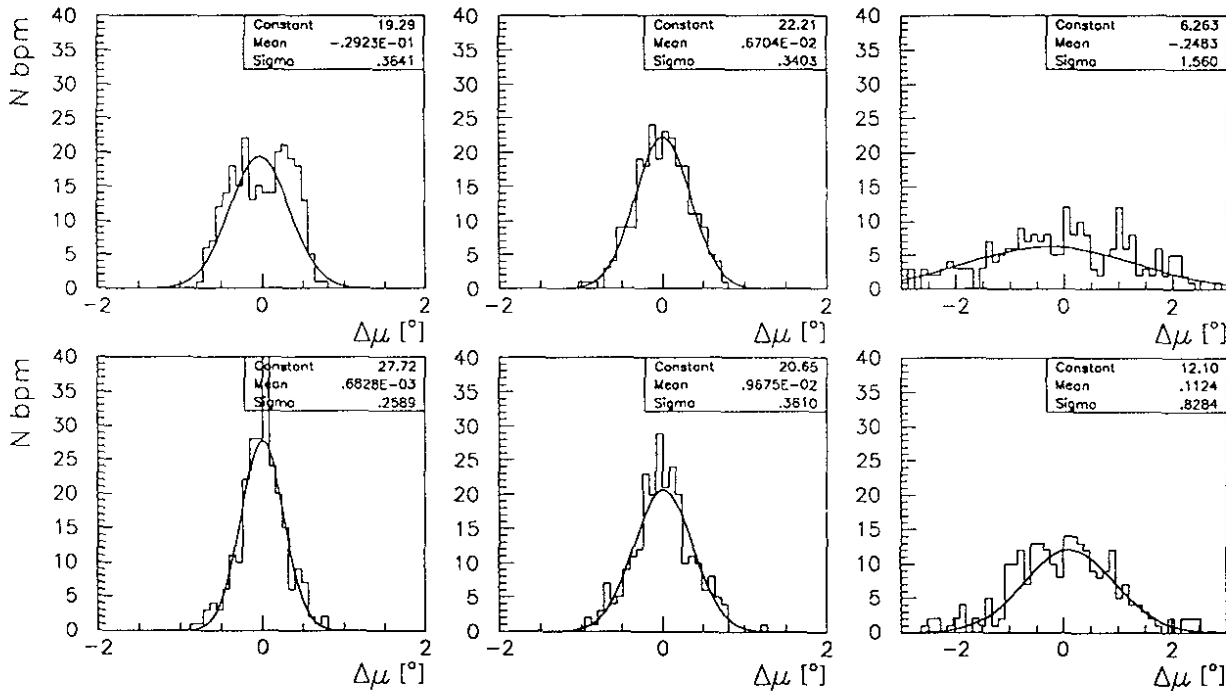


Figure 4.10: Histograms of the phase advance difference between pairs of measurements. The oscillation amplitudes and phase errors are shown in table 4.4.

date	time	optics	plane	bunch	ampl. [mm]	σ_ϕ [°] eq.(4.14)	$\sigma_{\Delta\phi_{12}}$ [°] eq.(4.16)	$\Delta\phi_{12}$ (r.m.s) [°] (measured)
4/26	20:24	k21p20v2	Ver.	2 e^-	5.6	0.04	0.08	0.36
4/26	20:27	k21p20v2	Ver.	2 e^-	6.5	0.04		
4/27	13:39	k21p20v2	Ver.	2 e^+	2.3	0.10	0.22	0.34
4/27	13:53	k21p20v2	Ver.	2 e^+	1.9	0.12		
4/28	0:55	k05p46v2	Hor.	2 e^+	0.7	0.33	0.50	1.6
4/28	1:03	k05p46v2	Hor.	2 e^+	1.7	0.13		
4/28	1:15	k05p46v2	Ver.	2 e^+	2.6	0.09	0.17	0.26
4/28	1:33	k05p46v2	Ver.	2 e^+	2.8	0.08		
5/6	19:58	k05p46v3	Ver.	1 e^+	3.4	0.07	0.13	0.36
5/6	20:01	k05p46v3	Ver.	1 e^+	3.5	0.07		
5/6	20:07	k05p46v3	Hor.	1 e^+	0.7	0.33	0.50	0.83
5/6	20:11	k05p46v3	Hor.	1 e^+	1.6	0.14		

Table 4.4: Amplitude and expected phase error from eq. (4.14) for $\sigma = 0.09$ mm for measurements taken in April and May 1994.

measurements show phase errors between 1.5 and 5 times the estimated ones using eq. (4.16). This result is compared to results obtained by analyzing the phase of more than 30 measurements using the two following methods:

1. An estimate of the phase error at each beam position monitor is obtained by analyzing the phase of short segments of $N/2$ points from a measurement of $N=1024$ points. Let φ_j be the phase obtained by harmonic analysis from the array of data $\{x_i\}_{i=j}^{j+511}$ (a segment of 512 points which begins at point j). The phases φ_j , with $j = 0, \dots, 512$, are delayed by $2\pi qj$ with respect to ϕ . If the array $\{x_i\}_{i=0}^{N-1}$ is a sample from a pure sine oscillation, all values $\varphi'_j = \varphi_j - 2\pi qj$ are equal to ϕ or φ_o . If the position x_i has a statistical error r.m.s. of σ , the spread between the phases φ'_j should correspond to the phase error estimated by eq. (4.14) for $N = 512$. However, the spread found at the measurements can be up to 10 times more than expected. Otherwise, if the phases φ_j of monitor 1 are compared to the set of phases in another adjacent monitor 2, the spread of phase advances $\Delta\varphi_j = (\varphi_j)_2 - (\varphi_j)_1$ agrees much better with the theoretical phase advance error of eq. (4.15) for $N = 512$. This leads to the conclusion that whatever effect introduces a change in the oscillations (e.g. 50 Hz noise, etc) is systematic for all monitors and the phase difference $\Delta\phi = \phi_2 - \phi_1$ between two monitors is not very sensitive to these perturbations.

As an example, three measurements with oscillation amplitudes of 1.5, 2.8 and 4.6 mm are analyzed by segments of 512 points, and the phase spread of $\Delta\varphi_j$ for every two pairs of monitors are plotted in histograms in fig. 4.11. Both axes are the same for the three plots. As the oscillation amplitude is increased, the distribution of phase spread is narrower and its mean position decreases.

The results of 30 measurements of vertical oscillations are shown in fig. 4.12, where each point is the mean phase spread of $\Delta\varphi_j$ of one measurement plotted against the oscillation amplitude. These results are compared to eq. (4.15) where $N = 512$ and $\sigma = 0.09$ mm, where $A_1 = A_2 = A$ since the selected monitors have the same amplitude. A fit of this equation on the results gives $\sigma = 0.106 \pm 0.003$ mm position error.

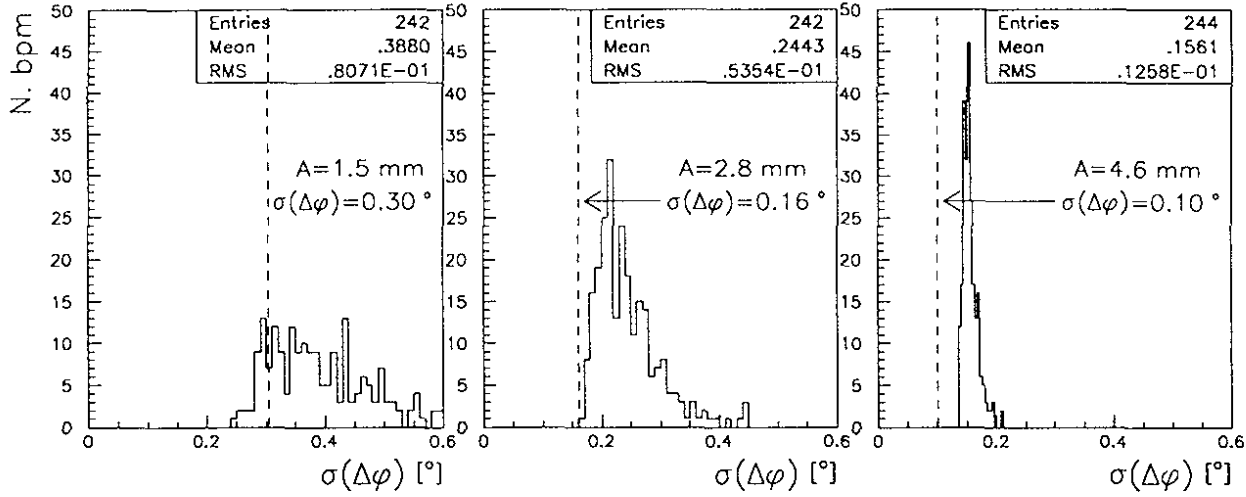


Figure 4.11: Histograms of the r.m.s. spread of the phase advances $\Delta\varphi_j = (\varphi_j)_2 - (\varphi_j)_1$ between pairs of monitors where φ_j are the phases obtained from a sliding window of 512 points. The histograms correspond to three measurements with amplitudes of 1.5 mm (left), 2.8 mm (middle) and 4.6 mm (right) taken on Sept. 3rd 1994. The vertical dashed line indicates the theoretical phase advance error of eq. (4.15) for $N = 512$.

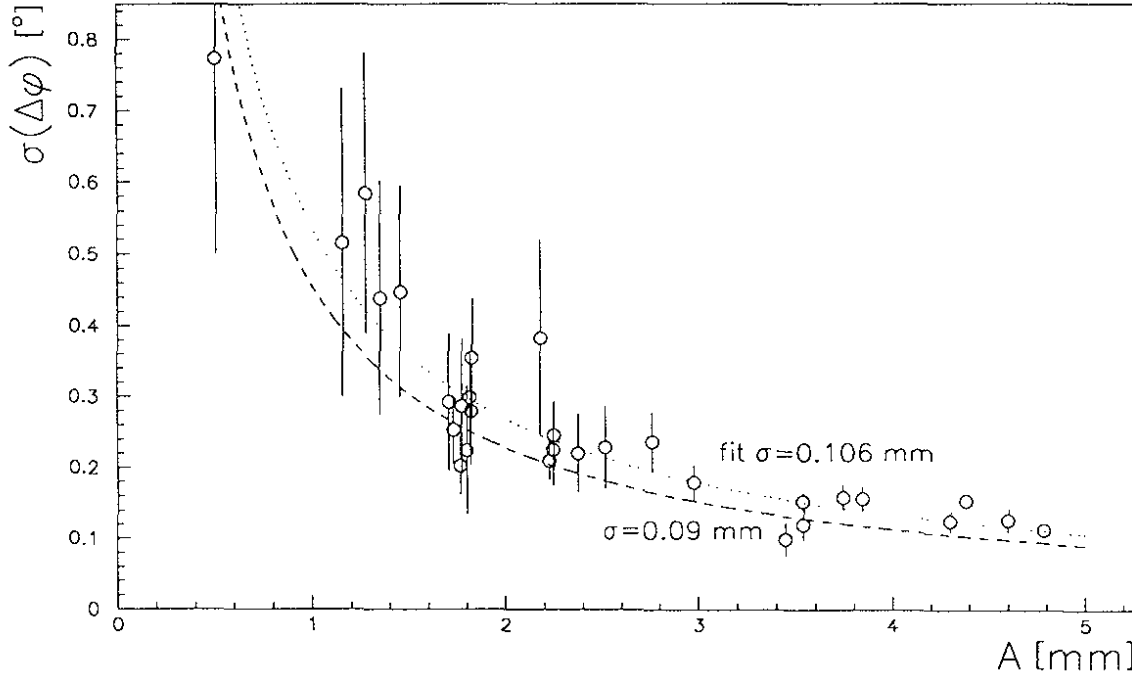


Figure 4.12: Average phase advance error of 250 monitors from sliding a window of 512 points versus the oscillation amplitude. The error bars are the r.m.s. spread of 250 monitors. The dashed line is given by eq. (4.15) for $\sigma = 0.09$ mm position error. A fit of σ to the data gives $\sigma = 0.106 \pm 0.003$ mm (dotted line).

2. The second method used to test eq. (4.14) compares the phase advance between two monitors by taking φ_o from the first segment of $N/2$ points and φ_{513} from the second segment. The difference between the phase advances $\Delta\varphi_o$ and $\Delta\varphi_{513}$ at every pair from 250 monitors gives an r.m.s. which is compared to eq. (4.15) for $N = 512$ in fig. 4.13. The error bars are calculated by $\sigma/\sqrt{2n}$, where $n = 250$ the number of monitors selected. A fit of eq. (4.15) for $N = 512$ on the results gives $\sigma = 0.111$ mm.

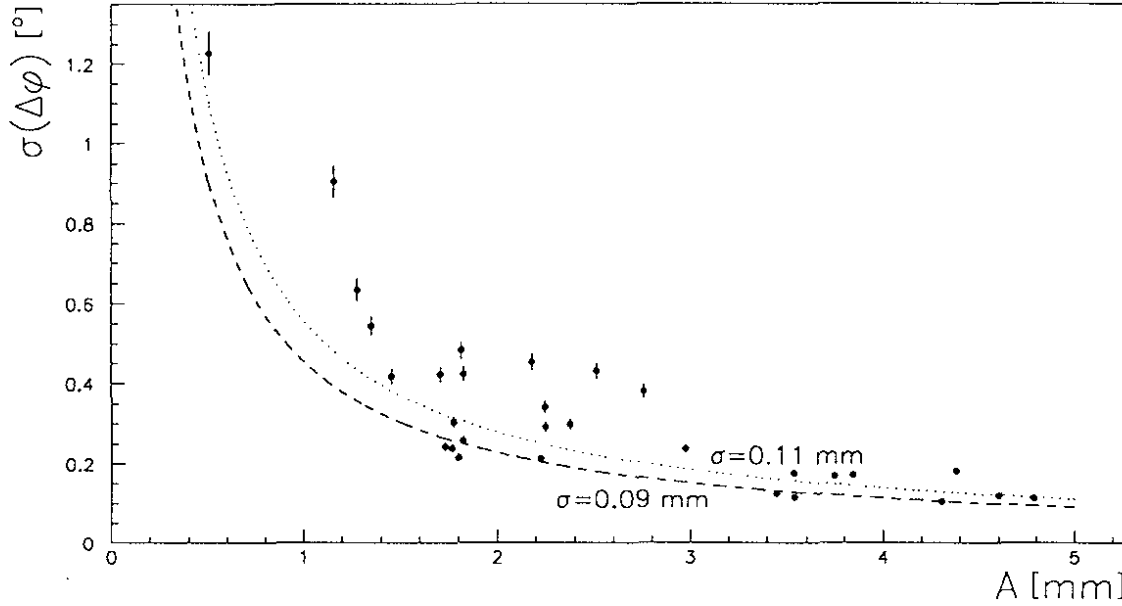


Figure 4.13: Phase advance r.m.s. between the two sets of 512 points versus the oscillation amplitude. The error bars are given by $\sigma/(2n)^{1/2}$, where $n = 250$. The dashed line is given by eq. (4.15) for $\sigma = 0.09$ mm position error and the dotted line is for $\sigma = 0.11$ mm.

The estimations of the phase error given by both methods correspond approximately to eq. (4.15) for $\sigma = 0.11$ mm. These results indicate that an oscillation amplitude of at least 2 mm (in an acquisition of 1024 points) is needed in order to reach a precision in the order of 0.14° on the phase obtained by harmonic analysis and about 0.2° on the phase advance between two monitors.

4.5 Beta function measurement error

Beta function measurement error at beam position monitors

The relative error $\varepsilon_{\beta'_1}$ of β'_1 from eq. (4.5) due to the error of the measured phase at the three beam position monitors is given by

$$\varepsilon_{\beta'_1} = \frac{1}{\beta'_1} \sqrt{\left(\frac{\partial \beta'_1}{\partial \phi'_1} \sigma_{\phi'_1}\right)^2 + \left(\frac{\partial \beta'_1}{\partial \phi'_2} \sigma_{\phi'_2}\right)^2 + \left(\frac{\partial \beta'_1}{\partial \phi'_3} \sigma_{\phi'_3}\right)^2}.$$

Since

$$\phi'_{12} = \phi'_2 - \phi'_1 \quad \text{and} \quad \phi'_{13} = \phi'_3 - \phi'_1$$

and

$$\frac{d(\cot x)}{dx} = -\frac{1}{\sin^2 x} = -(\cot^2 x + 1),$$

the partial derivatives are

$$\begin{cases} \frac{\partial \beta'_1}{\partial \phi'_1} = \frac{a_{12}c_{12}}{b_{12}} \left(\frac{1}{\sin^2 \phi'_{12}} - \frac{1}{\sin^2 \phi'_{13}} \right) , \\ \frac{\partial \beta'_1}{\partial \phi'_2} = -\frac{a_{12}c_{12}}{b_{12} \sin^2 \phi'_{12}} , \\ \frac{\partial \beta'_1}{\partial \phi'_3} = \frac{a_{12}c_{12}}{b_{12} \sin^2 \phi'_{13}} . \end{cases}$$

Dividing the expression of $\partial \beta'_1 / \partial \phi'_i$ by β'_1 we obtain

$$\frac{1}{\beta'_1} \frac{\partial \beta'_1}{\partial \phi'_1} = \frac{1}{\cot \phi'_{12} - \cot \phi'_{13}} \left(\frac{1}{\sin^2 \phi'_{12}} - \frac{1}{\sin^2 \phi'_{13}} \right)$$

which can be simplified using the trigonometric relation of eq. (4.9) to get

$$\begin{aligned} \frac{1}{\beta'_1} \frac{\partial \beta'_1}{\partial \phi'_1} &= \frac{\sin \phi'_{12} \sin \phi'_{13}}{\sin \phi'_{23}} \left(\frac{1}{\sin^2 \phi'_{12}} - \frac{1}{\sin^2 \phi'_{13}} \right) \\ &= \frac{\sin \phi'_{13}}{\sin \phi'_{12} \sin \phi'_{23}} - \frac{\sin \phi'_{12}}{\sin \phi'_{13} \sin \phi'_{23}} \\ &= (\cot \phi'_{12} + \cot \phi'_{23}) - (\cot \phi'_{23} - \cot \phi'_{13}) \\ &= \cot \phi'_{12} + \cot \phi'_{13} . \end{aligned}$$

Applying similar operations to the partial derivatives of β'_1 with respect to ϕ'_2 and ϕ'_3 , we obtain

$$\begin{cases} \frac{1}{\beta'_1} \frac{\partial \beta'_1}{\partial \phi'_1} = \cot \phi'_{12} + \cot \phi'_{13} , \\ \frac{1}{\beta'_1} \frac{\partial \beta'_1}{\partial \phi'_2} = -\cot \phi'_{12} - \cot \phi'_{23} , \\ \frac{1}{\beta'_1} \frac{\partial \beta'_1}{\partial \phi'_3} = \cot \phi'_{23} - \cot \phi'_{13} . \end{cases} \quad (4.17)$$

Thus, the relative error of β'_1 is

$$\varepsilon_{\beta'_1} = \sqrt{(\cot \phi'_{12} + \cot \phi'_{13})^2 \sigma_{\phi'_1}^2 + (\cot \phi'_{12} + \cot \phi'_{23})^2 \sigma_{\phi'_2}^2 + (\cot \phi'_{23} - \cot \phi'_{13})^2 \sigma_{\phi'_3}^2} . \quad (4.18)$$

Similarly, we deduce the relative error of β'_2 from eq. (4.6)

$$\varepsilon_{\beta'_2} = \sqrt{(\cot \phi'_{12} - \cot \phi'_{13})^2 \sigma_{\phi'_1}^2 + (\cot \phi'_{12} - \cot \phi'_{23})^2 \sigma_{\phi'_2}^2 + (\cot \phi'_{23} - \cot \phi'_{13})^2 \sigma_{\phi'_3}^2} \quad (4.19)$$

and the relative error of β'_3 from eq. (4.7)

$$\varepsilon_{\beta'_3} = \sqrt{(\cot \phi'_{12} - \cot \phi'_{13})^2 \sigma_{\phi'_1}^2 + (\cot \phi'_{12} + \cot \phi'_{23})^2 \sigma_{\phi'_2}^2 + (\cot \phi'_{23} + \cot \phi'_{13})^2 \sigma_{\phi'_3}^2} . \quad (4.20)$$

Measurement errors of the beta function depend on the phase measurement errors as well as on the phase advance between the monitors.

Dependence of the beta measurement error on the phase advance

The phase advance between beam position monitors changes around the ring and for different optics. We will now study the contribution of the phase advance between monitors to the measurement error of the beta function.

The dependence of the relative errors $\varepsilon_{\beta'_1}$, $\varepsilon_{\beta'_2}$ and $\varepsilon_{\beta'_3}$ on ϕ'_{12} and ϕ'_{23} is shown in 3 dimensional plots in fig. 4.14, assuming equal phase error at the three beam position monitors $\sigma_{\phi'_1} = \sigma_{\phi'_2} = \sigma_{\phi'_3} = 0.14^\circ$.

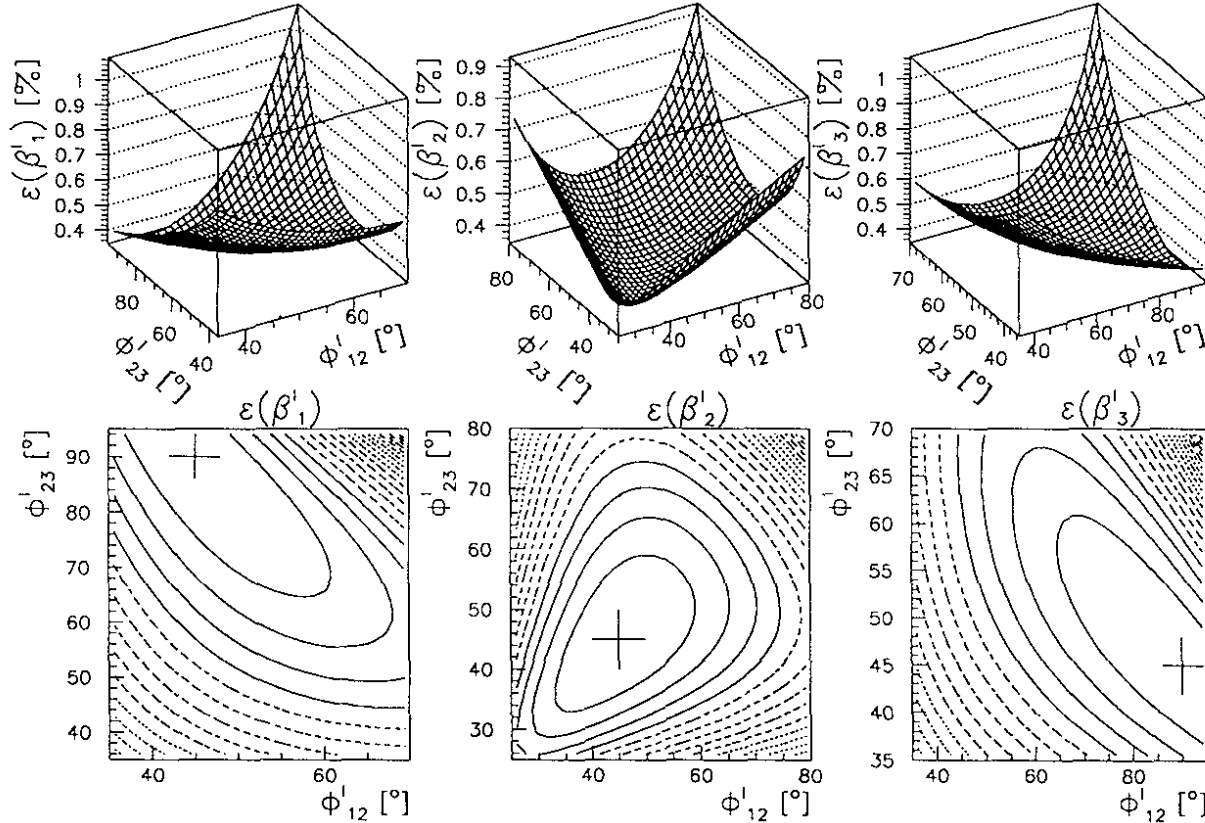


Figure 4.14: Top: 3D plots of the theoretical relative error of β' at monitor 1 (using eq. 4.18) on the left, at monitor 2 (using eq. 4.19) on the middle and at monitor 3 (using eq. 4.20) on the right as a function of the phase advances between them for phase error of 0.14° . Bottom: The contour plots corresponding to the 3D plots indicating the minimum with crosses.

When the measured phase has the same error at the three beam position monitors, eqs. (4.18), (4.19) and (4.20) have a minimum value for different phase advance values between the three monitors:

- The relative error $\varepsilon_{\beta'_1}$ has its minimum value for $\phi'_{12} = 45^\circ$ and $\phi'_{23} = 90^\circ$.
- The relative error $\varepsilon_{\beta'_2}$ has its minimum value for $\phi'_{12} = 45^\circ$ and $\phi'_{23} = 45^\circ$.
- The relative error $\varepsilon_{\beta'_3}$ has its minimum value for $\phi'_{12} = 90^\circ$ and $\phi'_{23} = 45^\circ$.

In the first case when $\phi'_{12} = 45^\circ$ and $\phi'_{23} = 90^\circ$, $\cot \phi'_{12} = 1$, $\cot \phi'_{23} = 0$ and $\cot \phi'_{13} = -1$ so eq. (4.18) gives

$$\varepsilon_{\beta'_1} = \sqrt{\sigma_{\phi'_2}^2 + \sigma_{\phi'_3}^2} = \sqrt{2} \sigma_{\phi'} \simeq 1.41 \sigma_{\phi'} .$$

However, for the same values of ϕ'_{12} and ϕ'_{23} the relative errors of β'_2 and β'_3 are higher

$$\varepsilon_{\beta'_2} = \varepsilon_{\beta'_3} = \sqrt{4\sigma_{\phi'_1}^2 + \sigma_{\phi'_2}^2 + \sigma_{\phi'_3}^2} = \sqrt{6} \sigma_{\phi'} \simeq 2.45 \sigma_{\phi'} .$$

A similar situation is found when the minimum relative error of β'_2 (or β'_3) is considered. The relative errors of the beta function at the three beam position monitors are shown in table 4.5, where all the optimum phase advance scenarios are considered.

$\min(\varepsilon_{\beta'})$	ϕ'_{12}	ϕ'_{23}	$\varepsilon_{\beta'_1}$	$\varepsilon_{\beta'_2}$	$\varepsilon_{\beta'_3}$
at monitor 1	45°	90°	$\sqrt{\sigma_{\phi'_2}^2 + \sigma_{\phi'_3}^2}$	$\sqrt{4\sigma_{\phi'_1}^2 + \sigma_{\phi'_2}^2 + \sigma_{\phi'_3}^2}$	$\sqrt{4\sigma_{\phi'_1}^2 + \sigma_{\phi'_2}^2 + \sigma_{\phi'_3}^2}$
at monitor 2	45°	45°	$\sqrt{\sigma_{\phi'_1}^2 + 4\sigma_{\phi'_2}^2 + \sigma_{\phi'_3}^2}$	$\sqrt{\sigma_{\phi'_1}^2 + \sigma_{\phi'_3}^2}$	$\sqrt{\sigma_{\phi'_1}^2 + 4\sigma_{\phi'_2}^2 + \sigma_{\phi'_3}^2}$
at monitor 3	90°	45°	$\sqrt{\sigma_{\phi'_1}^2 + \sigma_{\phi'_2}^2 + 4\sigma_{\phi'_3}^2}$	$\sqrt{\sigma_{\phi'_1}^2 + \sigma_{\phi'_2}^2 + 4\sigma_{\phi'_3}^2}$	$\sqrt{\sigma_{\phi'_1}^2 + \sigma_{\phi'_2}^2}$
at all three	60°	60°	$2\sqrt{(\sigma_{\phi'_2}^2 + \sigma_{\phi'_3}^2)/3}$	$2\sqrt{(\sigma_{\phi'_1}^2 + \sigma_{\phi'_3}^2)/3}$	$2\sqrt{(\sigma_{\phi'_1}^2 + \sigma_{\phi'_2}^2)/3}$

Table 4.5: Theoretical phase advance between beam position monitors to minimize the error of β for the same phase errors.

The relative beta measurement errors are shown in fig. 4.15 as functions of $\phi'_{12} = \phi'_{23} = \Delta\phi'$. To minimize the error of the measured beta function at the three beam position monitors at the same time, the measured phase advance must be $\phi'_{12} = \phi'_{23} = 60^\circ$. In this case, if the phase errors are the same, the relative error of β'_1 , β'_2 and β'_3 are the same

$$\varepsilon_{\beta'_1} = \varepsilon_{\beta'_2} = \varepsilon_{\beta'_3} = \sqrt{\frac{8}{3}} \sigma_{\phi'} \simeq 1.63 \sigma_{\phi'}$$

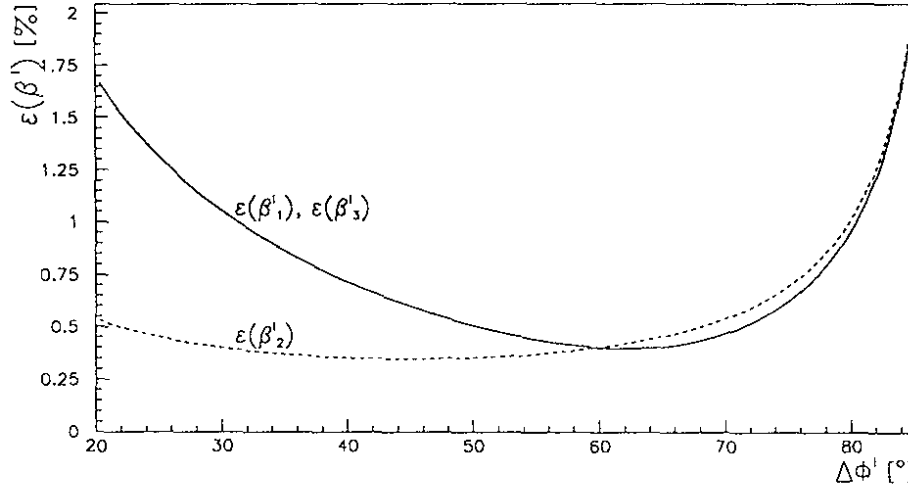


Figure 4.15: Theoretical relative error of β' at monitors 1,3 [eqs. (4.18) and (4.20)] (full line) and 2 [eq. (4.19)] (dashed line) as a function of the phase advances $\Delta\phi' = \phi'_{12} = \phi'_{23}$ for a phase error of 0.14° .

On the other hand, one must avoid getting close to either $\phi'_{12} = 0, 180^\circ, \dots$, $\phi'_{23} = 0, 180^\circ, \dots$ or $\phi'_{12} + \phi'_{23} = 180^\circ, 360^\circ, \dots$ (lines indicated in fig. 4.16), where the relative error of β'_1 , β'_2 and β'_3 diverges to infinity.

Measurement error of the beta function

The error of the beta function $\beta'(s)$ between three beam position monitors given by eq. (4.11) can be calculated from the error contribution of measured phases at the three monitors:

$$\sigma_{\beta'(s)} = \sqrt{\left(\frac{\partial\beta'(s)}{\partial\phi'_1}\sigma_{\phi'_1}\right)^2 + \left(\frac{\partial\beta'(s)}{\partial\phi'_2}\sigma_{\phi'_2}\right)^2 + \left(\frac{\partial\beta'(s)}{\partial\phi'_3}\sigma_{\phi'_3}\right)^2} \quad (4.21)$$

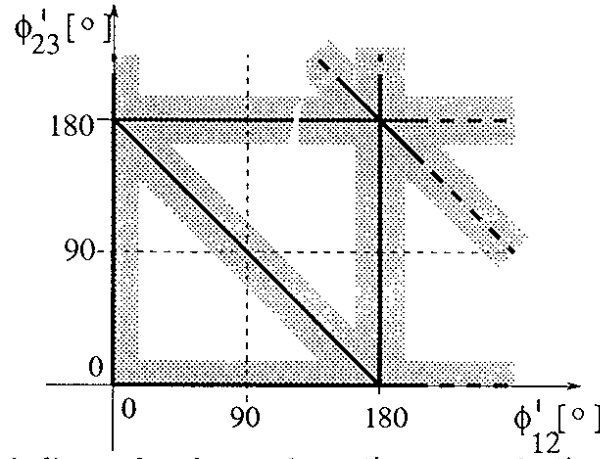


Figure 4.16: Black lines indicate the places where $\phi'_{12} = 0, 180^\circ$, $\phi'_{23} = 0, 180^\circ$ and $\phi'_{12} + \phi'_{23} = 180^\circ, 360^\circ$. Shaded areas indicate schematically where the relative beta error is too large.

where

$$\frac{\partial \beta'(s)}{\partial \phi'_i} = \beta'(s) \left[-\frac{1}{\beta'_1} \frac{\partial \beta'_1}{\partial \phi'_i} + \frac{2 \cot \phi'(s)}{1 + \cot^2 \phi'(s)} \frac{\partial \cot \phi'(s)}{\partial \phi'_i} \right] \quad i = 1, 2, 3$$

or

$$\frac{\partial \beta'(s)}{\partial \phi'_i} = \beta'(s) \left[-\frac{1}{\beta'_1} \frac{\partial \beta'_1}{\partial \phi'_i} + 2 \sin \phi'(s) \cos \phi'(s) \frac{\partial \cot \phi'(s)}{\partial \phi'_i} \right] \quad i = 1, 2, 3$$

where the partial derivatives of β'_1 are given in eq. (4.17) and the partial derivatives of $\cot \phi'(s)$ (eq. 4.10) are

$$\begin{cases} \frac{\partial \cot \phi'(s)}{\partial \phi'_1} = \frac{\cot \phi(s) - \cot \phi_{13}}{(\cot \phi_{12} - \cot \phi_{13}) \sin^2 \phi'_{12}} - \frac{\cot \phi(s) - \cot \phi_{12}}{(\cot \phi_{12} - \cot \phi_{13}) \sin^2 \phi'_{13}} , \\ \frac{\partial \cot \phi'(s)}{\partial \phi'_2} = \frac{-\cot \phi(s) + \cot \phi_{13}}{(\cot \phi_{12} - \cot \phi_{13}) \sin^2 \phi'_{12}} , \\ \frac{\partial \cot \phi'(s)}{\partial \phi'_3} = \frac{\cot \phi(s) - \cot \phi_{12}}{(\cot \phi_{12} - \cot \phi_{13}) \sin^2 \phi'_{13}} . \end{cases} \quad (4.22)$$

If s is replaced by s_1 , s_2 or s_3 , then eq. (4.21) corresponds to eqs. (4.18), (4.19) and (4.20), respectively.

When $\phi'_{12} = \phi'_{23} = 60^\circ$ and the errors of the measured phase at the three beam position monitors are equal $\sigma_{\phi'_1} = \sigma_{\phi'_2} = \sigma_{\phi'_3} = \sigma_{\phi'}$, the relative error of the beta function is constant between monitor 1 and 3

$$\varepsilon_{\beta'(s)} = \frac{\sigma_{\beta'(s)}}{\beta'(s)} = \sqrt{\frac{8}{3}} \sigma_{\phi'} \simeq 1.63 \sigma_{\phi'} \quad s \in [s_1, s_3] . \quad (4.23)$$

For instance, for phase errors of 0.14° , eq. (4.23) gives a relative beta function error of 0.4%.

Using eqs. (4.24) and (4.21), we can estimate the precision of the beta function measurements for a given setup of beam position monitors and magnetic lattice, as it is shown in fig. 4.17.

Error contribution from quadrupole fields

The method to obtain the beta and the phase functions from the phase measurement at three beam position monitors is based on the hypothesis that the magnetic fields of quadrupoles

and the layout of the magnets between the three beam position monitors are known with very good precision.

The relative gradient error of quadrupoles magnets has been measured to be about $\Delta k/k = 5 \cdot 10^{-4}$ r.m.s. [1]. The error contribution of a gradient error of $\Delta k/k$ at the quadrupole magnets between three beam position monitors in the arc on the measurement of the beta function at these monitors has been calculated using the expression:

$$\varepsilon_{\beta'_1} = \frac{\Delta k/k}{\beta'_1} \sqrt{\left(\frac{\partial \beta'_1}{\partial k_{QD1}} k_{QD1}\right)^2 + \left(\frac{\partial \beta'_1}{\partial k_{QF1}} k_{QF1}\right)^2 + \left(\frac{\partial \beta'_1}{\partial k_{QD2}} k_{QD2}\right)^2 + \left(\frac{\partial \beta'_1}{\partial k_{QF2}} k_{QF2}\right)^2},$$

where β'_1 is the expression given in eq. (4.5), $QD1$ and $QF1$ are the quadrupole magnets between monitor 1 and monitor 2 and $QD2$ and $QF2$ are the quadrupole magnets between monitor 2 and monitor 3. The derivatives terms have been calculated numerically. The relative error introduced by quadrupole gradient errors of $\Delta k/k = 5 \cdot 10^{-4}$ r.m.s is 0.2% on the measurement of the beta function at the three monitors. It is interesting to remark that the strongest contribution in the above expression is from $\partial \beta'_1 / \partial k_{QD2}$ at the three β'_1 , β'_2 and β'_3 . The smallest contribution is from $\partial \beta'_1 / \partial k_{QD1}$.

Measurement error of the phase function

The phase function $\mu'(s)$ in the area between three beam position monitors is obtained with

$$\mu'(s) = \mu'_1 + \phi'(s),$$

where μ'_1 is equal to ϕ'_1 plus a constant and the cotangent of $\phi'(s)$ is calculated in eq. (4.10):

$$\mu'(s) = \mu'_1 + \arctan\left(\frac{1}{\cot \phi'(s)}\right).$$

The error of the measured phase function $\mu'(s)$ can be calculated from the error contribution of the phases at the three beam position monitors

$$\sigma_{\mu'(s)} = \sqrt{\left(1 + \frac{\partial \phi'(s)}{\partial \phi'_1}\right)^2 \sigma_{\phi'_1}^2 + \left(\frac{\partial \phi'(s)}{\partial \phi'_2} \sigma_{\phi'_2}\right)^2 + \left(\frac{\partial \phi'(s)}{\partial \phi'_3} \sigma_{\phi'_3}\right)^2} \quad (4.24)$$

where

$$\frac{\partial \phi'(s)}{\partial \phi'_i} = \frac{-1}{1 + \cot^2 \phi'(s)} \left[\frac{\partial \cot \phi'(s)}{\partial \phi'_i} \right] = -\sin^2 \phi'(s) \left[\frac{\partial \cot \phi'(s)}{\partial \phi'_i} \right] \quad i = 1, 2, 3$$

in which the partial derivatives of $\cot \phi'(s)$ are given in eq. (4.22). If s is replaced by s_2 , i.e. the longitudinal position of monitor 2, in the above expressions, then $\sigma_{\mu'(s_2)} = \sigma_{\phi'_2}$ which corresponds to the error of the measured phase at monitor 2. And if s is replaced by s_3 , then $\sigma_{\mu'(s_3)} = \sigma_{\phi'_3}$. Finally, if s is replaced by s_1 , then $\sin^2 \phi'(s)$ is zero and $\sigma_{\mu'(s_1)} = \sigma_{\phi'_1}$.

In the case that $\sigma_{\phi'_1} = \sigma_{\phi'_2} = \sigma_{\phi'_3} = \sigma_{\phi'}$ and $\phi'_{12} = \phi'_{23} = 60^\circ$, the error of the phase function is constant:

$$\sigma_{\mu'(s)} = \sigma_{\phi'} \quad s \in [s_1, s_3].$$

Minimum measurement error of the phase function at LEP

The phase advance between beam position monitors determines the ratio between the measurement error of the phase of the oscillations $\sigma_{\phi'}$ and the relative error of the values of the beta function $\varepsilon_{\beta'}$. As result of the previous sections, we conclude that the most precise results of this method are obtained in the following conditions:

- When the beam position monitors are located at a local maximum of $\beta(s)$. Then the oscillation amplitude is high and therefore the signal to noise ratio is high, which leads to a small $\sigma_{\phi'}$ (see eq. 4.14).
- When the phase advance between the beam position monitors is 60° , so the ratio $\varepsilon_{\beta'}/\sigma_{\phi'}$ is minimum.

At LEP, both conditions are fulfilled at the beam position monitors in the arcs for the vertical plane, where the vertical phase advance per FODO cell is 60° . Since the beam position monitors are located near the defocusing (QD) quadrupoles, the phase advance between beam position monitors is also 60° and the beta function is maximum. The vertical beta function in the arcs can be obtained with a precision of less than 1% for oscillation amplitudes between 1 and 2 mm.

In the optics introduced in 1992, the horizontal phase advance per FODO cell was changed from 60° to 90° in order to reduce the horizontal beam emittance. This makes the measurement of the horizontal beta function in the arcs impossible with this method, because the error is too large (see previous section).

In the straight sections, the phase advance between beam position monitors has not a regular structure. Beta function measurement errors are calculated and presented in fig. 4.17 around interaction point 2. The relative error of β is calculated using eq. (4.21) and the phase function error is calculated using eq. (4.24), where the initial phase error at each beam position monitor is taken from eq. (4.14) assuming $N = 1024$ and an oscillation of maximum amplitude 3 mm, which corresponds to amplitudes of 2 mm (vertical) at the beam position monitors in the arcs.

Example

In the example of measured beta function given in section 4.3, the amplitude of the oscillations is about 4 mm (see table 4.1) and the estimated error for the phase is $\sigma_{\phi'} = 0.07^\circ$. The values given in table 4.2 are presented together with their errors in table 4.6. The errors of the beta function at monitors 1, 2 and 3 are obtained using eq. (4.18), (4.19) and (4.20) and the errors of the measured phase function are calculated using eq. (D.5), (D.6) and (D.7).

monitor	$\phi' (^\circ)$	$\beta' (m)$	α'
1	148.05 ± 0.05	159.3 ± 0.3	-2.201 ± 0.005
2	209.59 ± 0.07	137.6 ± 0.3	-1.949 ± 0.005
3	272.32 ± 0.07	155.8 ± 0.3	-2.305 ± 0.005

Table 4.6: Measured phase, beta and alpha functions at three beam position monitors.

The difference between measured and calculated phase functions and the ratio between measured and calculated beta functions are plotted in fig. 4.18. Errors are calculated using eqs. (4.24) and (4.21).

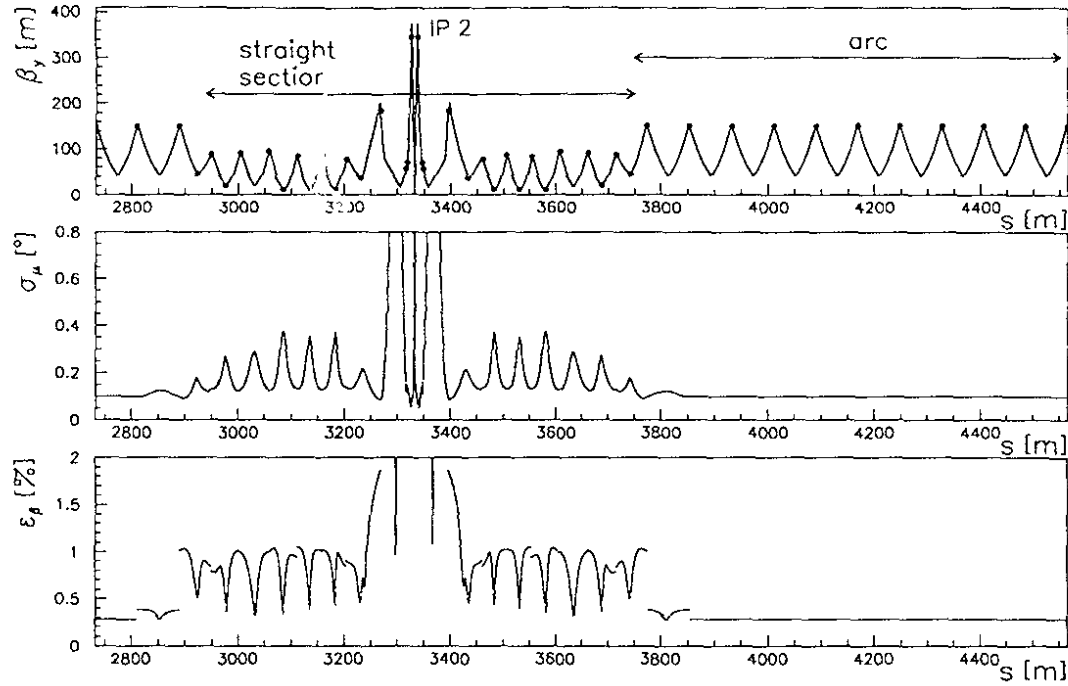


Figure 4.17: Vertical beta function around interaction point 2 of optics k05p46v3 (top). The dots indicate the location of the beam position monitors. The theoretical phase function measurement errors (middle) and relative beta function measurement errors (bottom) are calculated for an oscillation of 2 mm amplitude at the beam position monitors in the arc. As explained later, the average of the measurements gives an error smaller by a factor square root of two.

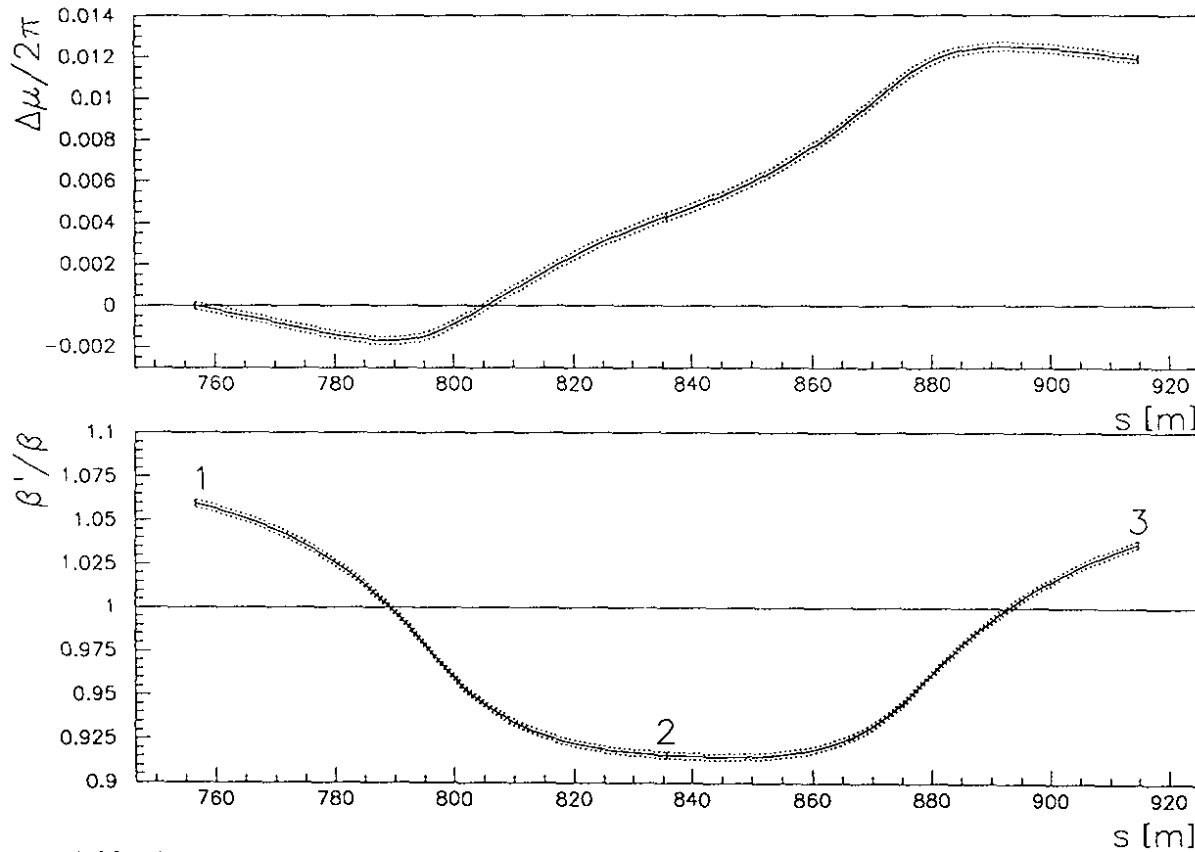
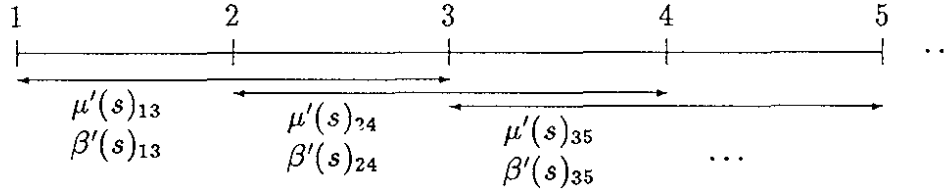


Figure 4.18: The difference between the measured and calculated phase function (top) and the ratio of measured over calculated beta function (bottom) in the interval between three beam position monitors are shown with full lines. The dashed lines indicate $\pm 1\sigma$ error of the measured value.

When all beam position monitors around the storage ring are considered, the beta and the phase function measurement method described above provides values between three beam position monitors which overlap with the functions obtained from the set of three beam position monitors on the right and on the left. The reason is that the beta function $\beta'(s)_{13}$ measured from the phases of, e.g. monitors 1, 2 and 3, overlaps between monitors 2 and 3 the beta function $\beta'(s)_{24}$ obtained from the phases of monitors 2, 3 and 4 and so on:



As a result of this, we have two values of the beta function for each point in the storage ring and three values at each beam position monitor.

An example is shown in fig. 4.19, where the beta and the phase functions calculated from the phase between monitors 1, 2, and 3 of the previous example and other contiguous sets of three monitors on the left and on the right are plotted together.

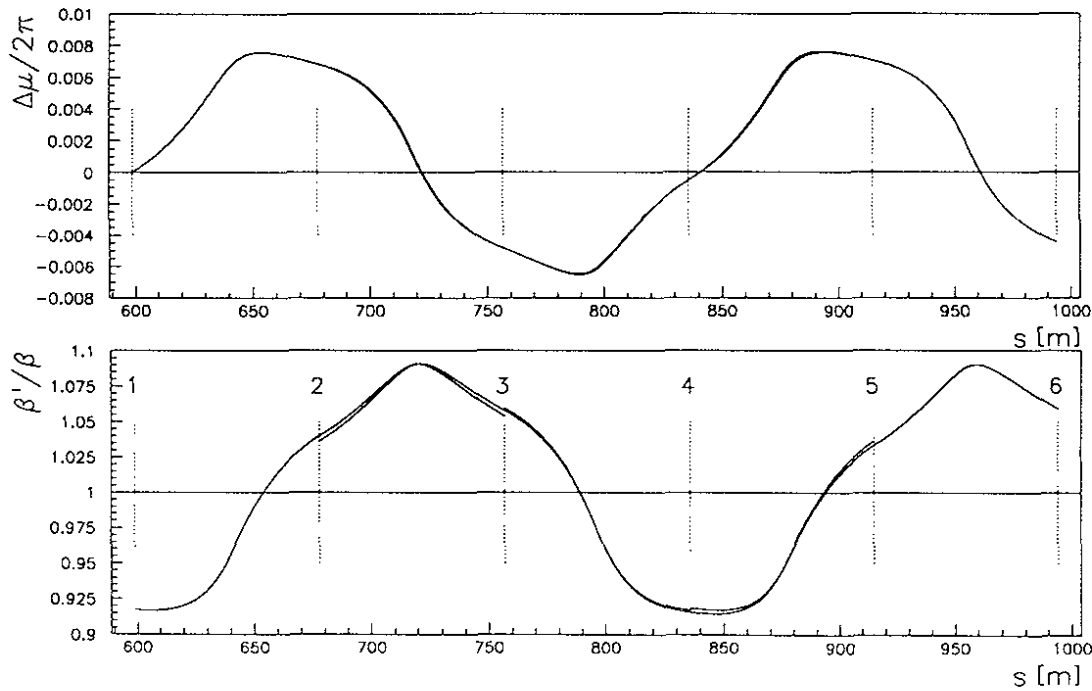


Figure 4.19: The difference $\mu' - \mu$ (top) and the ratio β'/β (bottom) obtained from the phase at a series of three beam position monitors are shown. Vertical dashed lines mark the location of the beam position monitors.

The results of beta and phase functions shown in the following are the weighted average between the two measurements, and the errors are the weighting of each measurement errors.

Experimental check of the beta and phase function measurement errors

To test the reliability and precision of the beta function measurement, two measurements of the vertical phase function carried out consecutively are selected. Betatron oscillations of about 3 mm amplitude were excited on the positron beam at 20 GeV. The optics functions β , α and μ are taken from the results of a simulation using MAD with the optics file

k21p20hv3. The measured phase function from both measurements are plotted in fig. 4.20 between interaction points 1 and 2. The difference between the measured vertical phase functions at each interval between two monitors gives between 0.04 and 0.07° r.m.s., which is twice less than the predicted sigma of 0.13° calculated as $\sigma = \sqrt{2}\sigma_{\phi'}$ where $\sigma_{\phi'}$ is given by eq. (4.14) for $N = 1024$, $A = 3$ mm and $\sigma = 0.11$ mm.

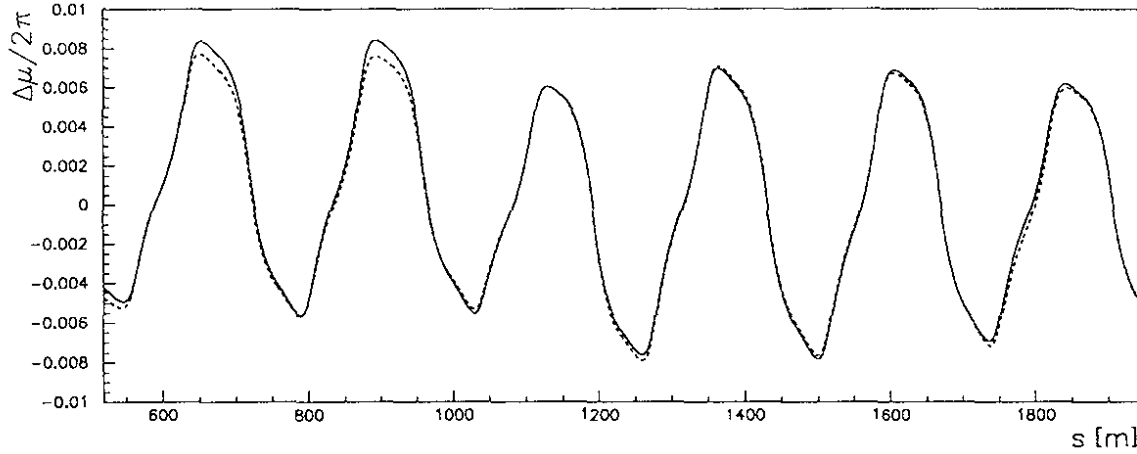


Figure 4.20: Measured vertical phase function in the arc between interaction points 1 and 2 from measurements done at 10:40 (full line) and at 10:45 (dashed line) on June 4th 1994. The lines represent the measured phase function using eq. (4.10) minus the phase function calculated with MAD. It is assumed $\mu'(s_1) = \mu(s_1)$ at the first beam position monitor.

The measured beta functions from both measurements are shown in fig. 4.21. The difference $(\beta'_1 - \beta'_2)/\beta$ at each interval between two monitors is about 0.15-0.25% r.m.s. , which is smaller than the predicted r.m.s. of 0.37% using eq. (4.23) for $\sigma_{\phi'} = 0.09^\circ$.

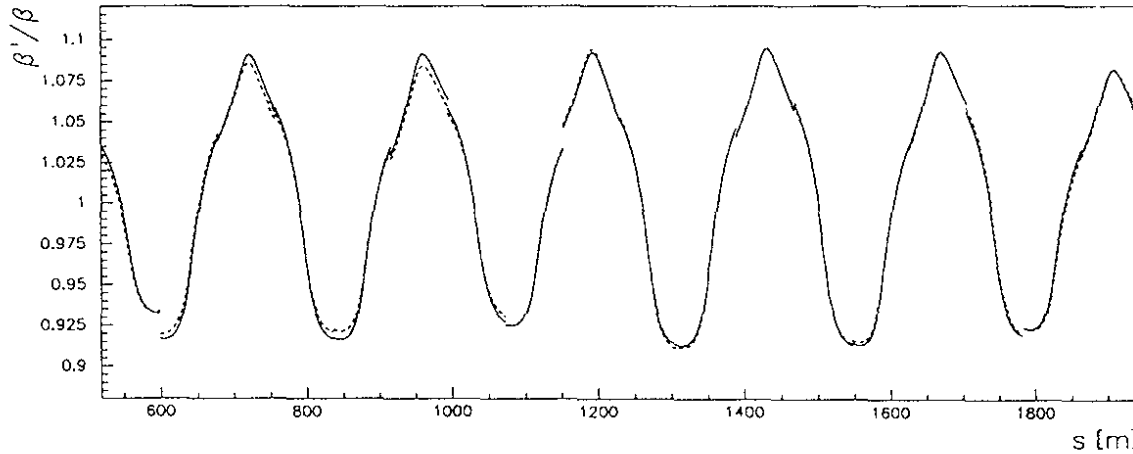


Figure 4.21: Measured vertical beta function from a measurement taken at 10:40 (full line) and another at 10:45 (dashed line) on June 4th 1994. The lines are the ratios of measured beta over calculated beta with MAD. The oscillation amplitude of the positron bunch was about 3 mm and the optics was k21p20hv3 with pretzel separators off.

The $(\beta' - \beta)/\beta$ ratio observed at LEP oscillates between $\pm 5\%$ and $\pm 15\%$ and is measured consistently on both measurements with small statistical error.

4.6 Experimental observation of beta-beating at LEP

As it is mentioned in section 2.1.2 the mismatch of the optics functions μ , β and α due to a quadrupole field error propagates along the storage ring as a wave whose phase is twice the phase function. The perturbation observed on the beta function is called *beta-beating*, and the perturbation of the phase function is also called *phase-beating*. If $\mu' - \mu$ and β'/β are plotted against the unperturbed phase function (instead of the longitudinal coordinate s), the perturbation on the phase and the beta functions can be observed as a sine function oscillation in a region where quadrupole gradient errors are negligible.

In this section, results of the beta and the phase functions obtained from phase measurements at beam position monitors are shown with respect to results of the beta and the phase functions from simulations using MAD in order to observe the optics mismatch as a beating oscillation around the storage ring.

4.6.1 Measurement of beta-beating due to a quadrupole field error

The effect of a single quadrupole gradient error on the vertical beta-beating has been measured from beta function measurements and compared to results of a simulation with MAD. The measurements were done on Sept. 4th 1994 [52] with the electron beam (4 bunches of about 100 μA each) at 45.6 GeV with the optics k05p46v3 ($\beta_y^* = 5$ cm). The field strength of the superconducting quadrupole QS0.R4 located at 4.7 m on the right of interaction point 4 was changed by $\Delta k = +0.0003$ m⁻² and vertical betatron oscillations were measured with an amplitude of 2 mm. Then, the field strength was changed by $\Delta k = -0.0006$ m⁻² ($\sim 3.7\%$) and the phase was measured again. The measured vertical tune shift is 0.034 ± 0.001 and the expected tune shift using eq. (2.13) for the nominal $\beta_y(Q) = 370$ m is 0.035. The differences between both measured phase and beta functions around interaction point 4 are shown in fig. 4.22 against the phase function calculated with MAD for the nominal field strengths. These differences show a phase-beating with an amplitude of 15° peak-to-peak and a beta-beating with an amplitude between $\pm 25\%$.

The change of the beta and of the phase functions due to a change of $\Delta k = -0.0006$ m⁻² of the superconducting quadrupole QS0.R4 field has been computed using MAD. The results $\Delta\mu$ and $\Delta\beta/\beta$ are shown in fig. 4.23 together with the difference in measured phase and beta functions, and the agreement is good.

4.6.2 Effect of QS0 calibration on vertical beta-beating

Most of the beta-beating observed with (non-colliding) beams at 20 or 45.6 GeV at LEP can be explained by the optics mismatch created from gradient errors in quadrupoles. Simulations on the effect of random quadrupole field errors on the beta function [53, 54, 55] show that calibration errors of superconducting quadrupoles have the strongest effect on the vertical beta-beating.

Results of a simulation of the effect of random errors on quadrupole gradients using MAD are given in table 4.7 for each group of quadrupoles: the MQC group (8 superconducting quadrupoles), the MQA group (288 quadrupoles located in the straight sections) and the MQ group (520 quadrupoles in the bending sections forming the FODO structure).

The simulations indicate that the superconducting quadrupoles give the strongest perturbation on the vertical beta function, because their magnetic strengths (around $k =$

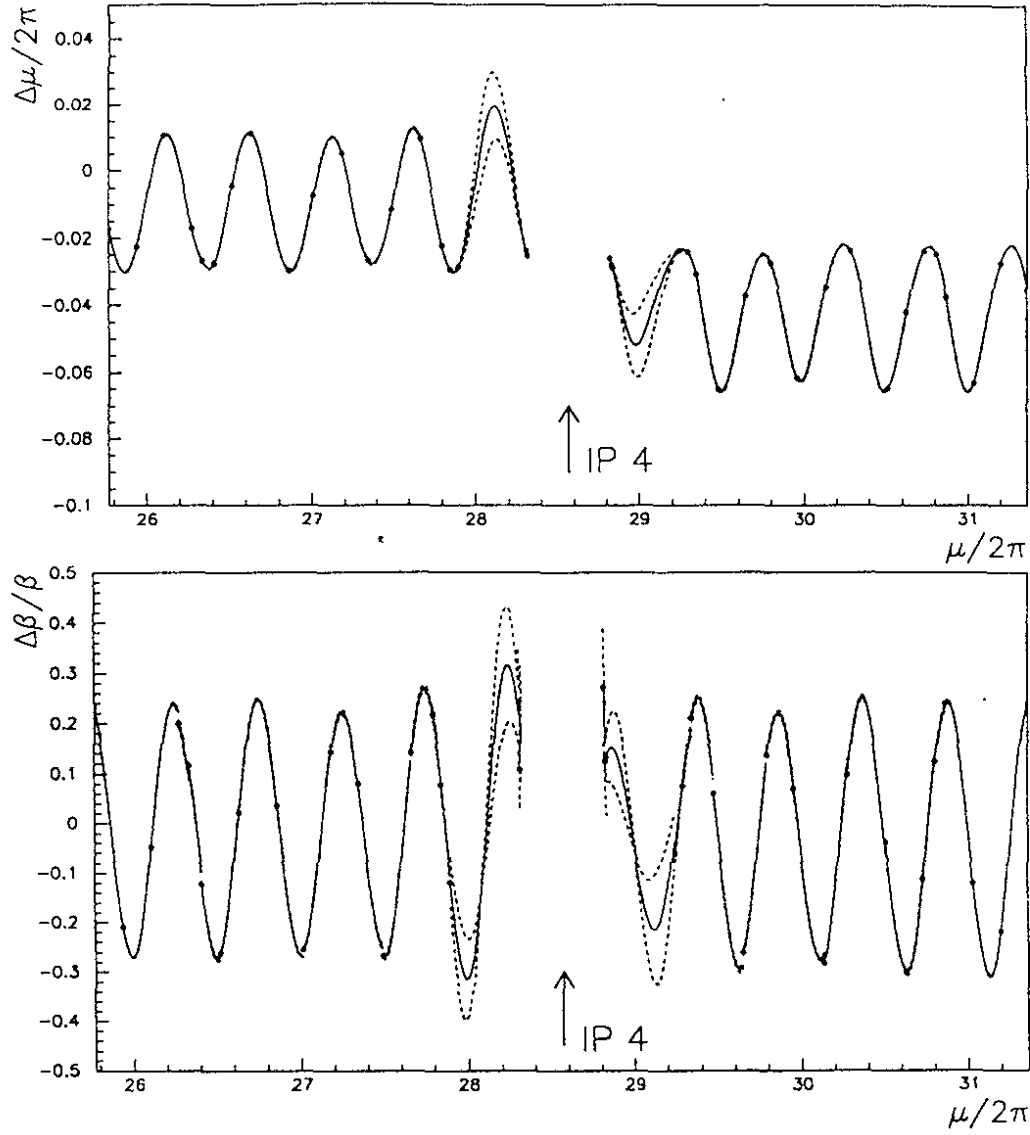


Figure 4.22: Difference in phase function (top) and beta function (bottom) between two measurements showing the effect of a field strength change of $\Delta k = -0.0006 \text{ m}^{-2}$ ($\sim 3.7\%$) applied to the quadrupole QS0.R4 located 4.7 m on the right of interaction point 4. The difference in beta function shown in the bottom plot is divided by the (unperturbed) beta function calculated with MAD. The values of the phase and beta functions at the beam position monitors are indicated with dots. Phase and beta function measurement errors ($\pm\sigma$) are indicated with a dotted line. Note that except near the interaction point, the error lines are very small and are drawn together with the measurements.

magnet group	$\Delta\beta_y/\beta_y$
MQC	15-30%
MQA	3-6%
MQ	4-7%

Table 4.7: Vertical beta function perturbation as a result of random quadrupole error ($\Delta k/k = 10^{-3}$ r.m.s.) simulation with MAD.

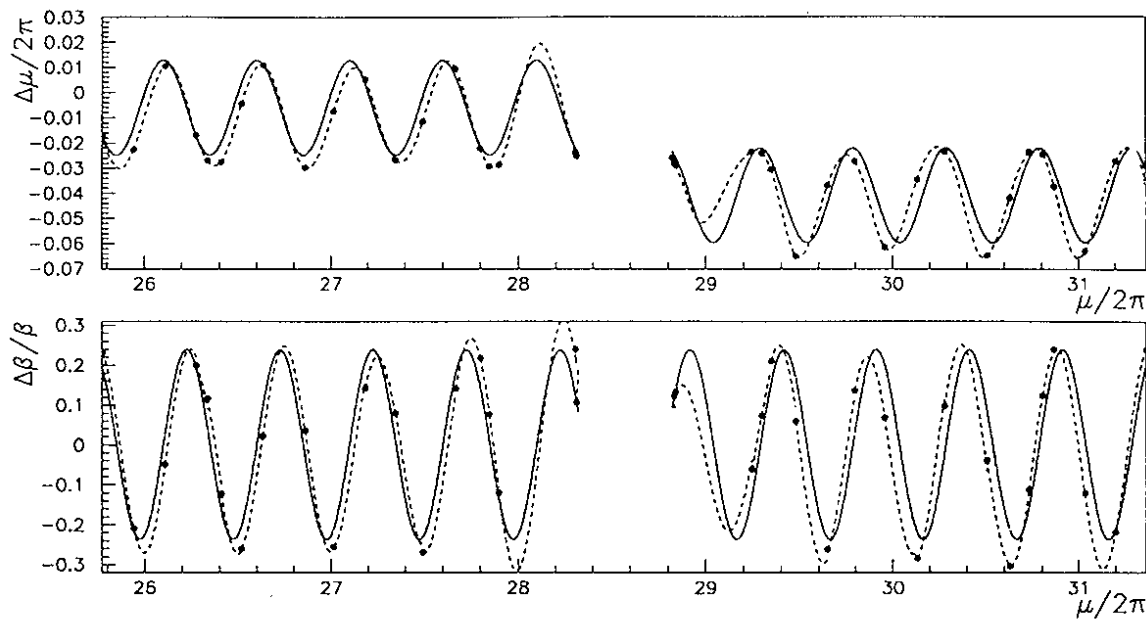


Figure 4.23: Difference in measured vertical phase function (top) and in measured vertical beta function (bottom) (divided by the nominal beta function) after a field strength change of $\Delta k = -0.0006 \text{ m}^{-2}$ ($\sim 3.7\%$) at the quadrupole QS0.R4 was applied. The results of a simulation with MAD are plotted with a full line and the measurements corresponding to fig. 4.22 are drawn with a dashed line.

-0.16 m^{-2}) are five times larger than the ones of other quadrupoles (of the order of 0.03 - 0.02 m^{-2}). In addition, the vertical beta function has its maximum value (about 400 m) inside these magnets.

To show the effect of gradient errors of superconducting quadrupoles, the beta-beating was observed before and after the re-calibration of the superconducting quadrupoles at the start-up of LEP in 1994 after the winter shutdown. The measured vertical beta function before the calibration of superconducting quadrupoles on April 28th 1994 is plotted in fig. 4.24 together with the beta function resulting from a simulation with MAD with the file k05p46v2. The measurement indicates a vertical beta-beating ($\Delta\beta/\beta$) with a maximum amplitude between 90 and 120%.

The values of the vertical beta function at the interaction point β_y^* were measured before the calibration of superconducting quadrupoles. The method consisted in measuring the tune shift created by changes on the superconducting quadrupole field strength as described in section 2.1.2. The measurements were carried out at various optics at 45.6 GeV with different nominal values of β_y^* and are shown in table 4.8. Parallel measurements of the vertical phase show that phase and beta-beating increases as the β_y^* was reduced.

optics	β_y^* (cm)					amplitude $\Delta\beta_y/\beta_y$
	nominal	IP 2	IP 4	IP 6	IP 8	
k21p46v2	21	20.4	20.3	18.8	20.1	10-20%
k09p46v2	9	7.9	7.0	7.1	7.4	40-60%
k07p46v2	7	5.6	4.5	4.2	4.7	60-80%
k05p46v2	5	4.1	2.8	2.5	3.9	90-120%

Table 4.8: Correlation between beta-beating and β^* mismatch at various 45.6 GeV optics (data from April 28th 1994).

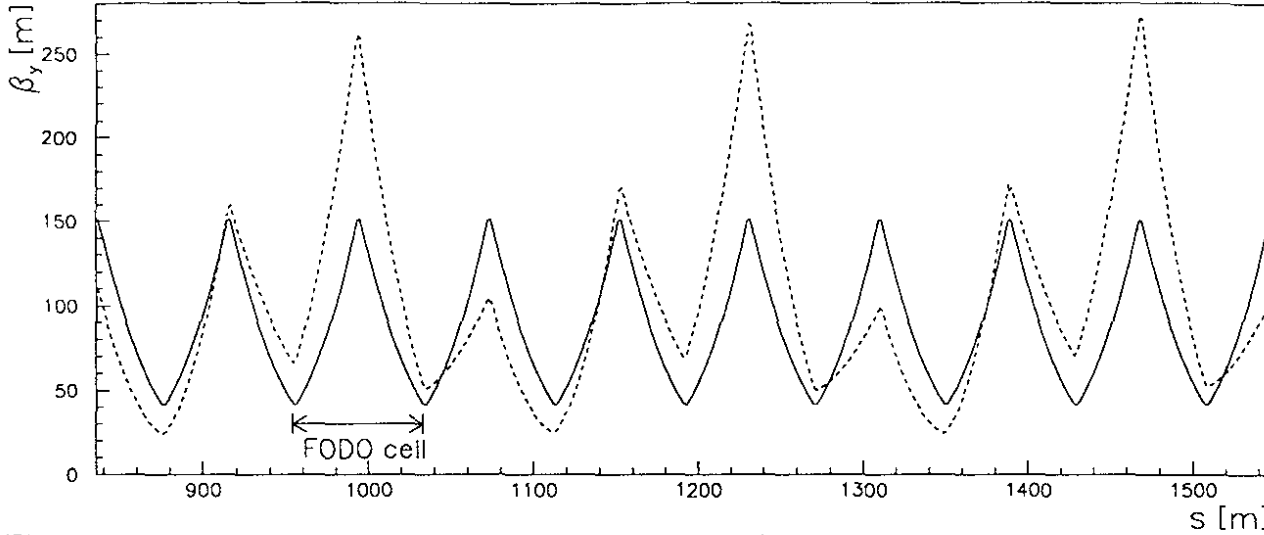


Figure 4.24: Measured vertical beta function (dashed line) at the LEP start-up in 1994 before the calibration of superconducting quadrupoles compared to the beta function calculated with MAD for the optics k05p46v2 (full line) in the arc between interaction points 1 and 2.

The values of β_y^* observed with the optics k05p46v2 were corrected by the re-calibration of the superconducting quadrupoles in interaction points 2, 4 and 8:

$$\left. \frac{\Delta k}{k} \right|_2 = 3.0 \cdot 10^{-3} \quad \left. \frac{\Delta k}{k} \right|_4 = 2.4 \cdot 10^{-3} \quad \left. \frac{\Delta k}{k} \right|_8 = 2.5 \cdot 10^{-3}$$

while in interaction point 6 the gradient of both quadrupoles remained unchanged. After correction, the β_y^* results were:

$$\beta_y^*(\text{IP } 2) = 4.8 \text{ cm} \quad \beta_y^*(\text{IP } 4) = 4.6 \text{ cm} \quad \beta_y^*(\text{IP } 6) = 4.6 \text{ cm} \quad \beta_y^*(\text{IP } 8) = 4.7 \text{ cm} .$$

The vertical beta function calculated from the phase measurement carried out on May 2nd 1994 after re-calibration of the superconducting quadrupoles gives a maximum $\Delta\beta/\beta$ amplitude between 15 and 30%.

A fine adjustment of the superconducting quadrupole calibration was made on Sept. 3rd 1994 [52] with the k05p46v3 optics to correct the β_y^* values

$$\beta_y^*(\text{IP } 2) = 5.4 \text{ cm} \quad \beta_y^*(\text{IP } 4) = 4.9 \text{ cm} \quad \beta_y^*(\text{IP } 6) = 5.3 \text{ cm} \quad \beta_y^*(\text{IP } 8) = 5.4 \text{ cm}$$

to the nominal $\beta_y^* = 5.0 \pm 0.1 \text{ cm}$ by the field strength changes:

$$\left. \frac{\Delta k}{k} \right|_2 = -2.1 \cdot 10^{-5} \quad \left. \frac{\Delta k}{k} \right|_4 = 7.6 \cdot 10^{-5} \quad \left. \frac{\Delta k}{k} \right|_6 = -2.2 \cdot 10^{-5} \quad \left. \frac{\Delta k}{k} \right|_8 = 0.3 \cdot 10^{-5}$$

which reduced the maximum beta-beating ratio $\Delta\beta/\beta$ by a factor of 2 (from 20-30% down to 10-15%).

4.6.3 Sources of opposite beta-beating for e^+ and e^- beams

Random quadrupole field errors, calibration errors and longitudinal positioning errors create in first order the same beta-beating for e^+ and e^- beams. Closed orbit deviations could produce some beta-beating which is equal for e^+ and e^- beams if their closed orbits are

the same. However, pretzel orbit separation and energy sawtooth create beta-beating with opposite sign for the positron and the electron beams [55].

When 8×8 equidistant bunches are injected in the so-called pretzel scheme (see section 1.2), electrostatic fields are applied to electron and positron beams to separate the closed orbits of the two beams in order to avoid collisions in the arcs. The electrostatic separators used for the pretzel scheme modify the closed orbits of e^+ and e^- beams and create a long bump which closes before the next even interaction point (see fig. 1.2). The amplitude of the closed orbit separation and the beta-beating depend on the optics and on the electrostatic field of the separators as listed in table 4.9.

optics	sep. field (kV)	orbit amp. (mm)	beta-beating amp.	
			$\Delta\beta_y/\beta_y$	$\Delta\beta_x/\beta_x$
g05p46h	120	4.4	20-30%	8-10%
k05p46v3	100	4.2	18-26%	6-8%

Table 4.9: Closed orbit amplitude and beta-beating amplitude for two pretzel separations and optics at 45.6 GeV. (sep.: separator, amp.: amplitude.)

The effect of pretzel bumps on the beta-beating is opposite for the electron and the positron beams. The beta-beating is due to the large excursions of the beam off-center of the sextupole magnets which act on the beam as an extra quadrupole gradient. The effect is opposite for each beam because the beams have opposite amplitudes at the sextupoles.

For a separator field of 120 kV the effect of pretzel bumps on the vertical beta and phase functions was measured the first time on Aug. 5th 1993 with a positron beam at 45.6 GeV and for optics g05p46h. In this experiment, the betatron oscillation phase of the 2nd positron bunch was measured at the beam position monitors with pretzel separators set at an electric field of 120 kV and then when their voltage were set to zero. The ratios of the measured over calculated beta functions for both situations are shown in fig. 4.25.

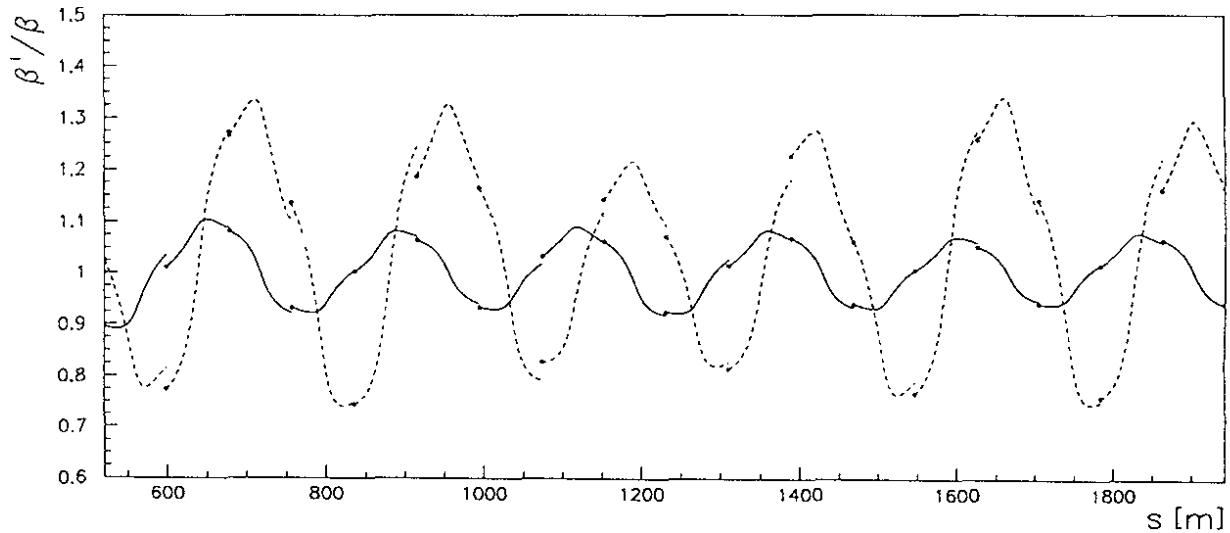


Figure 4.25: Ratio between measured and calculated vertical beta function in the arc between interaction points 1 and 2 when pretzel separators were off (full line) and on at 120 kV (dotted line).

The difference $\mu'_{\text{on}} - \mu'_{\text{off}}$ between the phase function obtained at each measurement and the difference $(\beta'_{\text{on}} - \beta'_{\text{off}})/\beta'_1$ are shown in fig. 4.26. The beta and the phase functions

have been obtained by a simulation with MAD in which the electrostatic field of 120 kV was applied to the pretzel separators ES.QS11 located at 240 m both sides of the even interaction points. The results of this simulation for the positron beam is included in fig. 4.26.

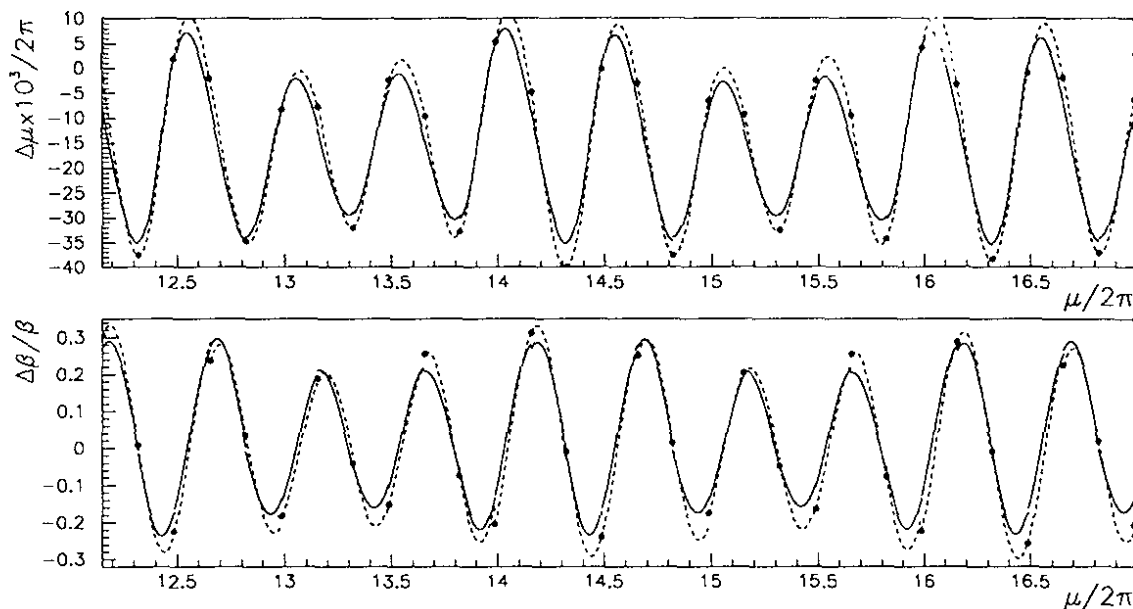


Figure 4.26: Difference of measured phase and beta functions with positron beam (dashed lines) in the arc between interaction points 1 and 2 due to pretzel orbit separation (120 kV) at 45.6 GeV and optics g05p46h. Results from a simulation with MAD are shown with full lines.

The vertical phase-beating $\Delta\mu(s)$ and the vertical beta-beating $\Delta\beta(s)/\beta(s)$ of the positron and the electron beams resulting from a simulation with MAD including pretzel separation of 120 kV for beams of 45.6 GeV and optics g05p46h are presented in fig. 4.27 from interaction point 1 to 3. In the horizontal plane the beta-beating created by the pretzel separation is about $\pm 10\%$.

Beta-beating caused by the energy sawtooth at 45.6 GeV.

At LEP, electron and positron beams lose a small part of their energy in the dipole magnets due to synchrotron radiation. The energy loss at 45.6 GeV is around 125 MeV per revolution and it increases with the fourth power of the energy of the beam (see eq. 1.1), so for beams at 90 GeV the energy loss per revolution will be about 2 GeV. This energy is lost in the bending sections and it is recovered in the radio-frequency (RF) cavities installed symmetrically around the interaction points 2 and 6. Consequently, the energy of the beam is not constant but follows a so-called *sawtooth* function as shown schematically in fig. 4.28.

A small but measurable effect on the beta-beating is due to the energy loss by electron and positron beams at 45.6 GeV. This opposite beta-beating is caused by two effects:

- The effect of quadrupole fields is stronger for a particle with lower energy and weaker for a particle with higher energy. This effect is more significant at quadrupoles located before and after the RF cavities in the straight sections 2 and 6, where the energy of electrons and positrons are about ± 25 MeV different from the average energy.
- The trajectory of particles with lower energy is bent by the dipole magnets more than the trajectory of particles with nominal energy. Consequently, the trajectories of the beams are different and the offset in the sextupoles changes the optics functions.

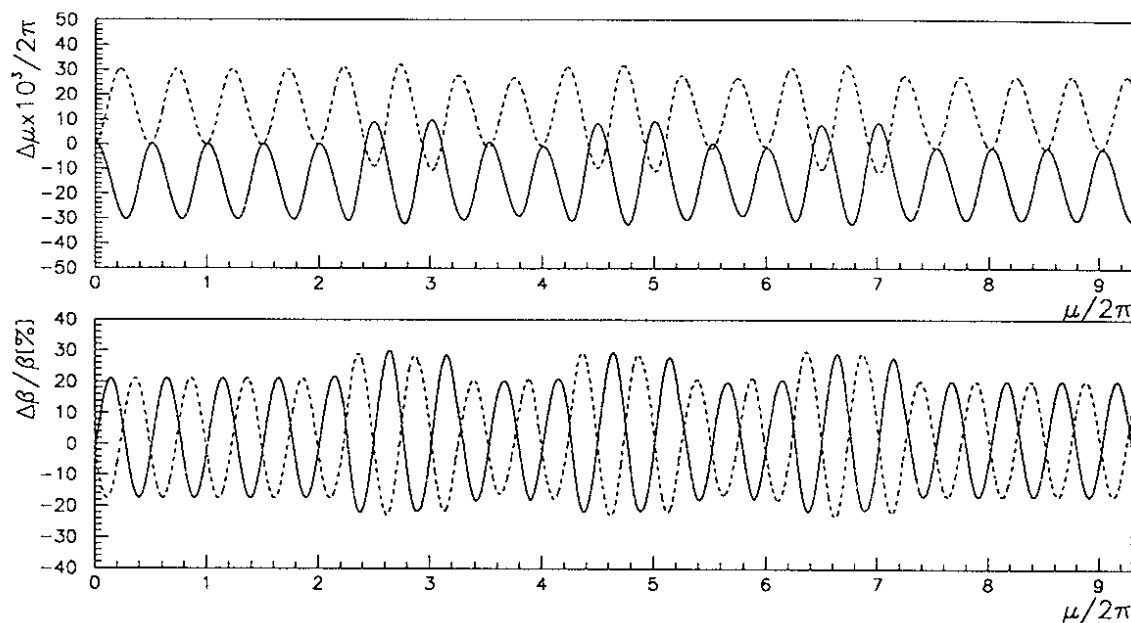


Figure 4.27: Opposite vertical phase-beating (top) and beta-beating (bottom) between interaction points 1 and 2 for positrons (full line) and electrons (dashed line) beams. The data is obtained from a simulation using MAD which includes pretzel separation of 120 kV.

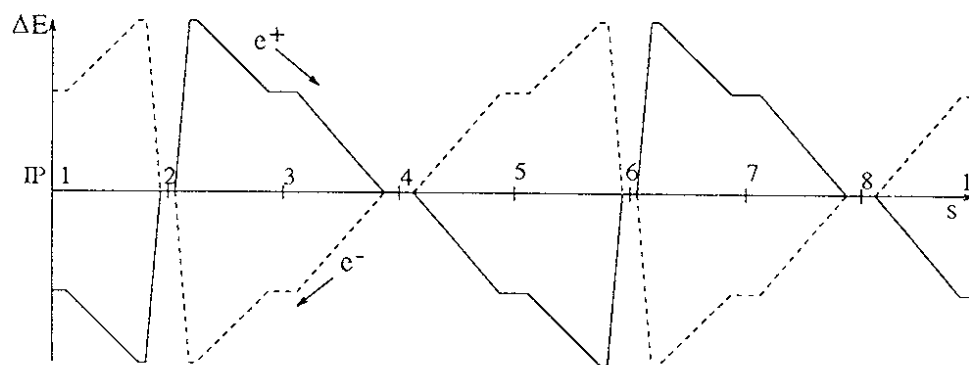


Figure 4.28: Energy change of electron and positron beams along the longitudinal coordinate representing the energy sawtooth. Acceleration cavities are located around interaction points 2 and 6.

The energy sawtooth effect on the horizontal beam orbit is clearly visible from the difference between the electron and the positron orbits measured by the Beam Orbit Measurement system (BOM) (fig. 4.29).

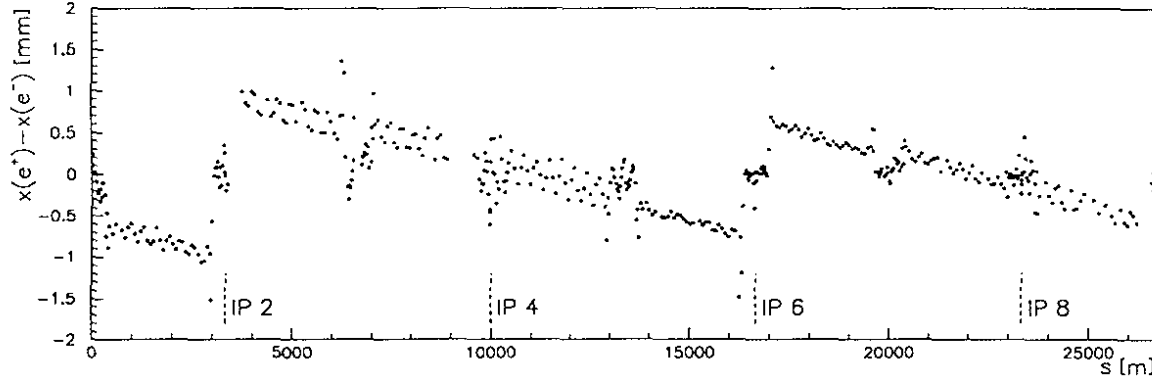


Figure 4.29: Horizontal orbit difference between electron and positron beams measured at 45.6 GeV with beam position monitors.

The effect of the energy sawtooth on the vertical beta-beating is observed in the difference between the measured beta function for the positron and electron beams. This difference is maximum in the straight sections of interaction points 2 and 6, where the amplitude of $(\beta'_{e+} - \beta'_{e-})/\beta$ is up to 12%. The measured beta functions are shown in fig. 4.30, divided by the beta function calculated using MAD.

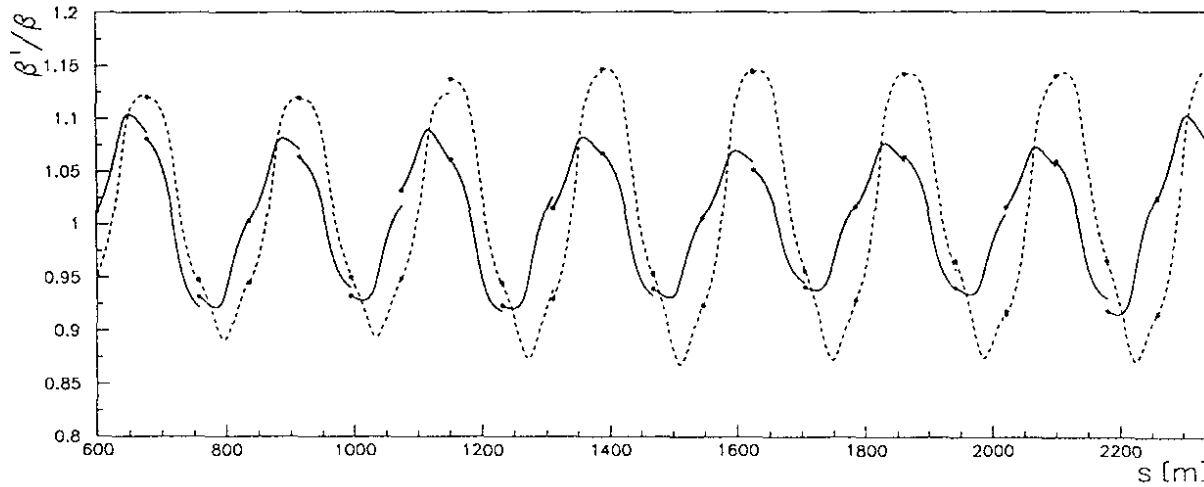


Figure 4.30: Measured vertical beta function divided by calculated beta function with MAD in the arc between interaction points 1 and 2 with the positron beam (full line) and the electron beam (dotted line). The measurements were done on Aug. 5th 1993 at 45.6 GeV with optics g05p46h.

The difference in the phase and the beta functions between positrons and electrons are plotted in fig. 4.31. The data is compared with the results of a simulation with MAD in which the effect of energy radiation loss was included.

The vertical phase-beating $\Delta\mu(s)$ and the vertical beta-beating $\Delta\beta(s)/\beta(s)$ of the positron and electron beams have been simulated with MAD including synchrotron radiation for beams of 45.6 GeV with optics g05p46h and are presented in fig. 4.32 from interaction point 1 to 2. The vertical phase-beating and beta-beating of electron and positron beams are maximum where the energy difference is the largest (at interaction points 2 and 6). In the horizontal plane the beta-beating created by energy sawtooth is about $\pm 2\%$.

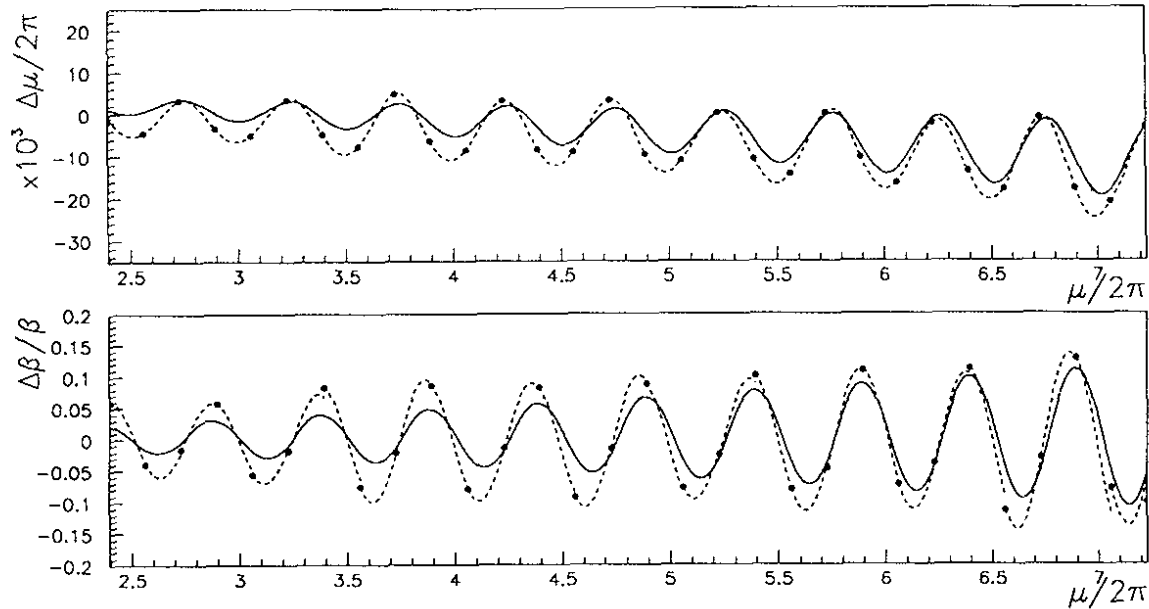


Figure 4.31: The vertical phase function difference $\mu'_{e+} - \mu'_{e-}$ (top) and the vertical beta-beating difference $(\beta'_{e+} - \beta'_{e-})/\beta$ (bottom) between electron and positron beams in the arc between interaction point 1 and 2. Results from measurements done on Aug. 5th 1993 are shown with dashed lines. Results from a simulation with MAD are shown with full lines. The beam energy is 45.6 GeV and the optics file is g05p46h.

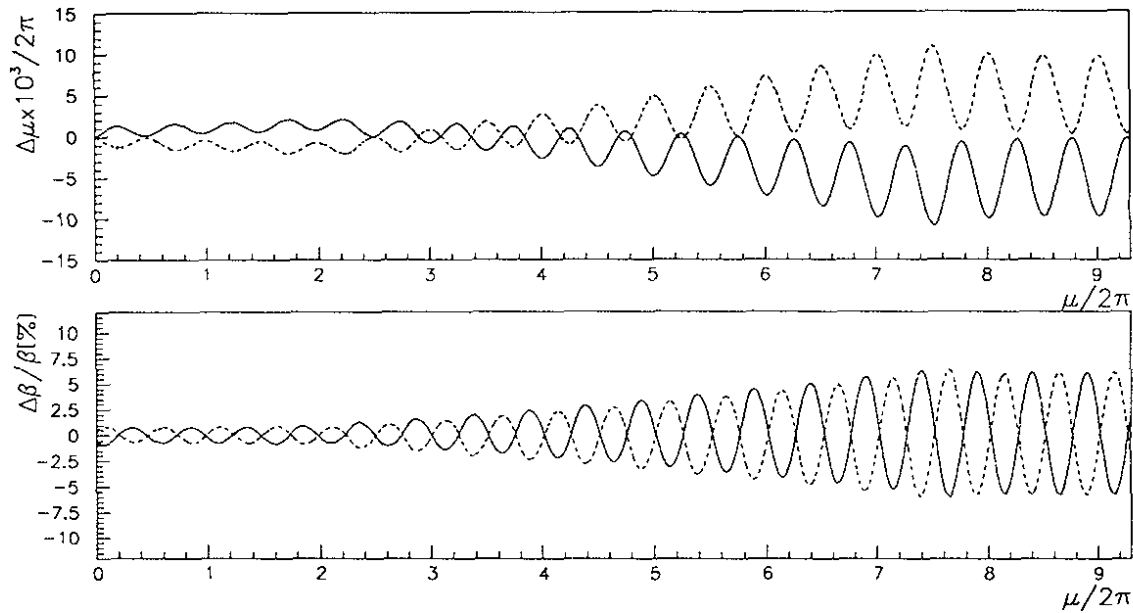


Figure 4.32: Opposite vertical phase-beating (top) and beta-beating (bottom) between interaction points 1 and 2 for positrons (full line) and electrons (dashed line) beams. The data is obtained from a simulation using MAD which takes into account the energy loss due to synchrotron radiation. The beating is symmetric around the interaction point 2 and the same pattern appears around interaction point 6.

4.7 Measurement of the chromaticity distribution at LEP

The measurement of the phase of betatron oscillations has been used to check the chromaticity correction of the magnetic lattice of LEP in an experiment reported in [3].

Definition of chromaticity

The chromaticity Q' is defined as the change of betatron tunes due to a change of the momentum (or energy since $E \cong pc$) of the beam. It is given by the expressions

$$Q'_x = \frac{dQ_x}{dp/p} \quad \text{and} \quad Q'_y = \frac{dQ_y}{dp/p} .$$

To describe locally the chromaticity, we use the *chromatic phase function* defined as the phase function dependence on the momentum deviation

$$\frac{d\mu_x}{dp/p}, \frac{d\mu_y}{dp/p} \quad \text{or normalized} \quad \frac{d\mu_x/2\pi}{dp/p}, \frac{d\mu_y/2\pi}{dp/p} . \quad (4.25)$$

The integral of the normalized chromatic phase functions over the ring circumference are Q'_x and Q'_y , respectively.

Quadrupole magnets introduce negative chromaticity since they increase the betatron phase of particles with smaller momentum ($\Delta p < 0$) and decrease the betatron phase of particles with larger momentum ($\Delta p > 0$). Stable beams are obtained when $Q' > 0$. The negative chromaticity created by the quadrupoles is compensated using higher order magnetic elements. At LEP, sextupole magnets are installed in the arcs where the horizontal position x of a particle is a function of its momentum. A particle with a momentum deviation Δp has an offset with respect to the closed orbit given by $x = D_x \Delta p/p$, where D_x is the dispersion function. The magnetic field of a sextupole is proportional to the square of the distance from its center. A particle will be focused or defocused depending on the polarity of the sextupole field. This will also lead to a change of the phase of its betatron oscillation. Applying the correct polarity to sextupole magnets, the negative chromaticity created by quadrupole magnets can be compensated to obtain stable beams at $Q' > 0$.

The experiment

The horizontal and the vertical chromatic phase functions are obtained from the difference between phase measurements taken with beams of different momenta. The beam momentum is changed by shifting the frequency f_{RF} of the accelerating RF cavities. For highly relativistic particles ($\gamma \simeq 9 \cdot 10^4$ for electrons at 45.6 GeV) the particle velocity does not change (since $\beta = v/c \cong 1$), therefore

$$\frac{\Delta f_{RF}}{f_{RF}} = -\frac{\Delta C}{C}$$

where C is the length of the beam orbit. The change in momentum Δp is related to the change of orbit length by the momentum compaction factor α_c :

$$\frac{\Delta f_{RF}}{f_{RF}} = -\frac{\Delta C}{C} = -\alpha_c \frac{\Delta p}{p} .$$

At LEP, α_c is approximately $1.86 \cdot 10^{-4}$.

In the experiment carried out on June 4th 1994 (reported in [3]), the RF-frequency was changed by $\Delta f_{RF} = -100$ Hz, which corresponds to a momentum deviation of $\Delta p = 70$ MeV/c (1.53‰). The difference $\Delta\mu(s)$ between the vertical phase functions measured at $\Delta f_{RF} = -100$ Hz and $\Delta f_{RF} = 0$ is shown in fig. 4.33 between interaction point 1 and 3.

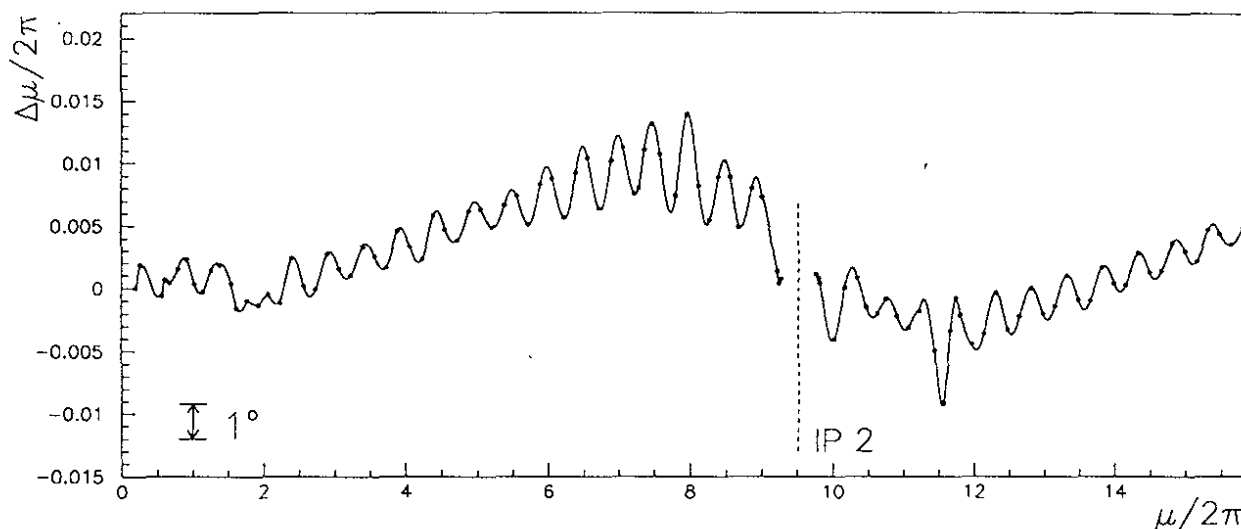


Figure 4.33: Vertical phase function difference around interaction point 2 due to beam momentum change of $\Delta p = 70$ MeV/c (1.53‰). Dots indicate the phase at beam position monitors.

The vertical chromatic phase function as defined in eq. (4.25) is obtained from the difference $\Delta\mu(s)$ between the measured vertical phase functions at $\Delta f_{RF} = -100$ Hz and $\Delta f_{RF} = 0$ divided by the relative momentum change $\Delta p/p = 1.53\text{‰}$.

The results shown in fig. 4.34 are discussed in more detail in [3]. They agree well with MAD calculations, showing that there is no strong error in the chromatic correction of the magnetic lattice of LEP.

4.8 Measurement of the impedance distribution at LEP

The distribution of the impedance of the vacuum chamber around the storage ring has been measured from the phase advance dependence on the bunch current [4]. The electromagnetic field created by a bunch of particles induces currents on the walls of the vacuum chamber. The electromagnetic field created by these currents acts on the particles of the bunch modifying their dynamical behavior and therefore the optics functions which determine the betatron oscillations. This effect depends on the intensity of the bunch and on the reactive transverse impedance of the walls of the vacuum chamber. The most important contribution to this impedance comes from the RF cavities and the vacuum chamber bellows.

The phase function is measured with positron bunches of intensities ranging from $50 \mu\text{A}$ to $500 \mu\text{A}$. The betatron tune dependence on the bunch current

$$\frac{dQ_x}{dI_b} = -0.071 \pm 0.002 \text{ mA}^{-1} \quad \frac{dQ_y}{dI_b} = -0.128 \pm 0.002 \text{ mA}^{-1}$$

is calculated from the fit to the betatron tunes measured with the Q-meter shown in fig. 4.35.

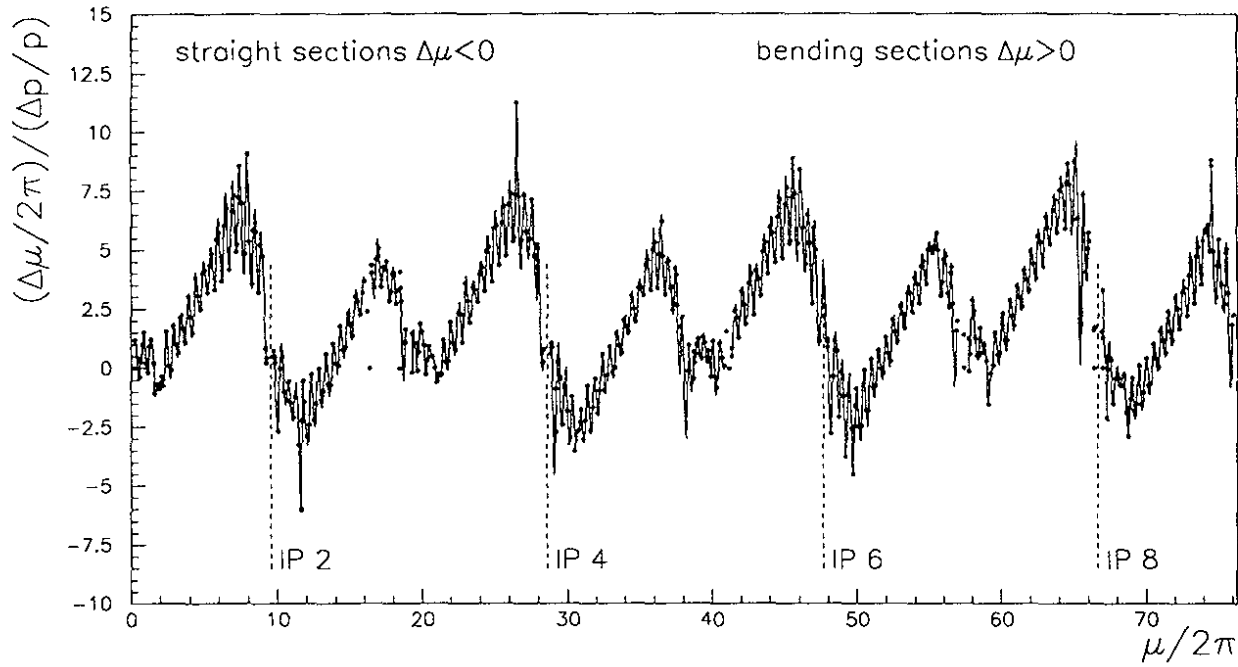


Figure 4.34: Measured vertical chromatic phase function. The dots indicate the chromatic phase function at the beam position monitors.

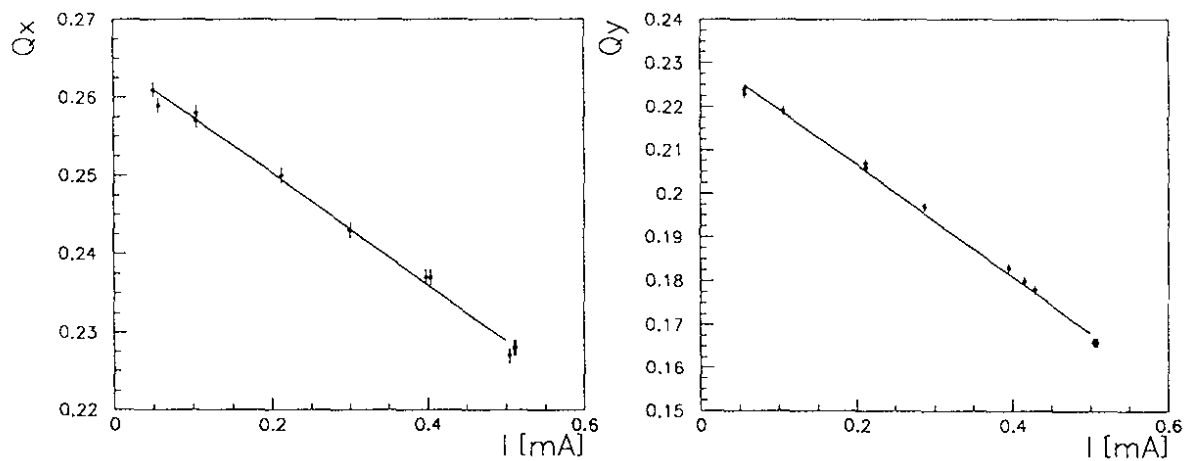


Figure 4.35: Vertical and horizontal tunes versus bunch current measured with positrons at 20 GeV (optics k21p20v3) on June 4th 1994.

To describe locally the dependence of the phase function on the bunch intensity, we define

$$\frac{d\mu_x}{dI}, \frac{d\mu_y}{dI} \quad \text{or normalized} \quad \frac{d\mu_x/2\pi}{dI}, \frac{d\mu_y/2\pi}{dI}.$$

The integral of the normalized quantities over the ring circumference is dQ_x/dI_b and dQ_y/dI_b .

The analysis has been done with phase measurements taken on June 4th and on Sept. 3rd 1994. The measured phase change due to an increase of the bunch current of $\Delta I_b = 0.275$ mA is shown in fig. 4.36 between interaction points 1 and 3.

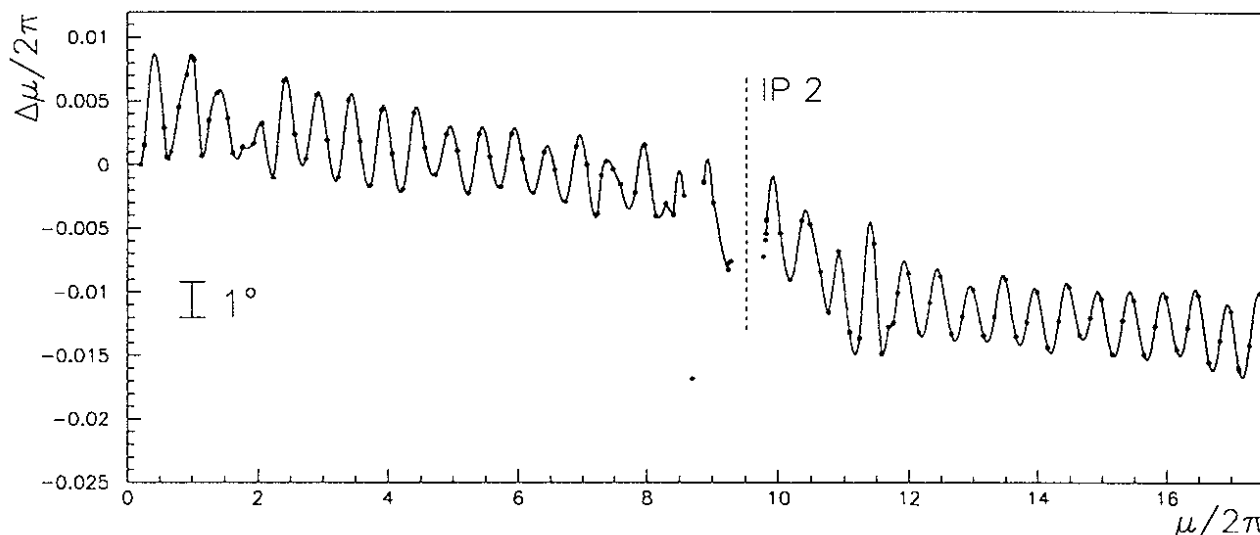


Figure 4.36: Difference of the measured vertical phase function around interaction point 2 due to a change in bunch current of $\Delta I_b = 0.275$ mA, obtained with a positron bunch at 20 GeV (optics k21p20v3) on Sept. 3rd 1994. The dots indicate the measurements at the beam position monitors.

The effect of impedance on the vertical phase function is shown in fig. 4.37, where the fraction $(d\mu_y/2\pi)/dI$ is plotted against the phase function.

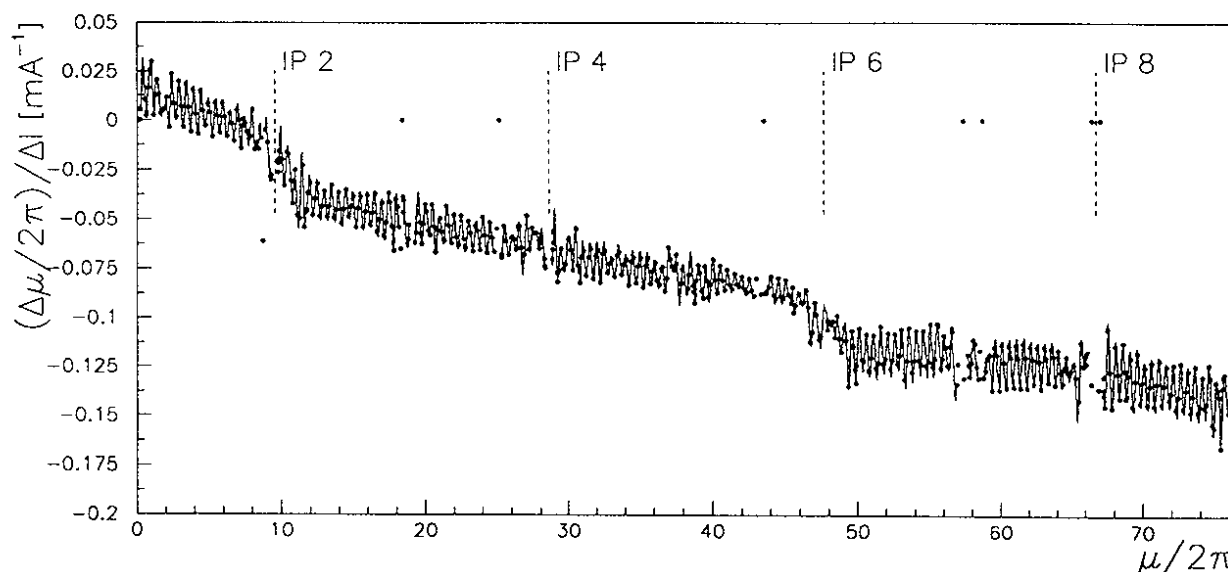


Figure 4.37: Effect of the impedance on the vertical phase function measured with positrons at 20 GeV (optics k21p20v3) on Sept. 3rd 1994. The quantity $(\Delta\mu_y/2\pi)/\Delta I$ is calculated from phase measurements with positron bunches of 0.420 and 0.145 mA.

The phase results obtained in both vertical and horizontal planes agree well with the impedance model of LEP. The tune shift per bunch current due to the impedance of the RF

cavities is approximately the same in both planes, which is about 75% of the total horizontal tune shift and about 50% of the total vertical tune shift. The measurements show a more or less uniformly distributed impedance in the rest of the machine. This correspond to the expectations since the vacuum chamber is elliptic (its width is larger than its height) and the effect of the shielded bellows is stronger on the vertical plane. A more detail discussion of these results is reported in [4].

Chapter 5

Luminosity and beam size measurements at LEP

The expression for the luminosity \mathcal{L} as a function of beam intensities and sizes given in eq. (1.2) can be rewritten in terms of the horizontal ε_x and vertical ε_y beam emittances using eq. (2.5)

$$\mathcal{L} = \frac{1}{2\pi e^2 k_b f_{rev}} \frac{I_{e+} I_{e-}}{\sqrt{\beta_x^* \beta_y^* (\varepsilon_{x_{e+}} + \varepsilon_{x_{e-}})(\varepsilon_{y_{e+}} + \varepsilon_{y_{e-}})}} \quad (5.1)$$

where:

I_{e+} and I_{e-} are the positron and electron beam currents,

e is the electron charge,

f_{rev} is the revolution frequency,

k_b is the number of bunches per beam and

β_x^* and β_y^* are the horizontal and vertical beta functions at the interaction points.

In this chapter, the effect of beta-beating on beam emittance measurement errors is discussed. Luminosity measurements are compared to the luminosity calculated with eq. (5.1) using the measured beam emittances, intensities and beta functions.

5.1 How does beta-beating affect beam size measurements?

The beam emittance ε is derived from beam profile measurements (assuming dispersion zero) using eq. (2.5):

$$\varepsilon = \frac{\sigma_{mon}^2}{\beta_{mon}} \quad (5.2)$$

where σ_{mon} is the r.m.s. of the measured beam profile and β_{mon} is the value of the beta function at the profile measurement point. The accuracy of horizontal and vertical beam emittances measurements depends on profile measurement errors and systematic errors up to 20% in ε_y can be made due to beta-beating.

Transverse beam size monitors

The transverse beam profile can be measured with good precision at LEP with two types of instruments: wire scanners and synchrotron light telescopes.

Wire scanners [56] measure the intensity of bremsstrahlung photons emitted by a thin carbon wire moved transversely through the beam in the vertical or horizontal plane. The position of the wire is measured with a high precision optical ruler. The passage of the wire through the beam can blow up the beam. This blow up can be measured by comparing the results of forward and backward scans. After the forward scan the beam is blown up and the backward scan yields an increased beam size. The measurement of the beam size can be disturbed by beam instabilities. The electromagnetic field of the beam causes heating in the carbon wire and limits the operation of this instrument to a maximum total intensity of 1.7 mA. The carbon wire has been lately replaced by a quartz one which resists beam intensities up to 7 mA.

Synchrotron light telescopes (or Beam Emittance Ultra-Violet monitors BEUV) [57] measure the image of the profile of synchrotron radiation emitted by the beam in a dipole magnet. The light image is integrated over about 20 ms. The precision of these monitors is affected by diffraction and depends on the optical setup of the instrument. These effects are taken into account in the calibration curve:

$$\epsilon = \frac{\sigma_{\text{mon}}^2 - \sigma_{\text{offset}}^2}{\beta_{\text{mon}}} \quad (5.3)$$

where σ_{mon} is the r.m.s. of the light profile at the plane of the CCD camera, σ_{offset} is the correction for diffraction and β_{mon} is the value of the beta function at the light source. A detailed description of the detector calibration can be found in [6].

Two other types of monitors provide information of the transverse shape of the beam by measuring synchrotron light turn by turn: the X-ray profile monitors [58] and the streak camera [59]. They have been extensively used to study bunch instabilities. However, their absolute scale depends on the light optics elements and hardware setup and they have to be calibrated with the other monitors.

Beta function at the beam profile monitors

The values of the beta function at beam profile monitors are calculated with MAD. Beta-beating can change these values and cause systematic errors on emittance measurements.

Several factors introduce beta-beating in LEP optics:

- The beta-beating introduced by pretzel separation can be calculated with the MAD program and a good agreement has been found with beta-beating measurements reported in section 4.6.3.
- The beta-beating introduced by energy sawtooth can also be calculated and corresponds approximately to measured values (see section 4.6.3).

The vertical and horizontal $\Delta\beta/\beta$ ratios at beam profile monitors which are shown in table 5.1 are the result of a simulation using MAD program when pretzel separation and energy sawtooth are included. Due to the symmetric location of electron and positron profile monitors (BEUV monitors near quadrupole QS12 are at 281.5 m from both sides of interaction point 8, the vertical wire scanners at 224.1 m and the horizontal wire scanners at 220.1 m from both sides of interaction point 1) the ratio $\Delta\beta/\beta$ of the e^+ beam at e^+ profile monitors is equal to the ratio $\Delta\beta/\beta$ of the e^- beam at e^- profile monitors.

Other factors which introduce beta-beating are:

profile monitor	$\Delta\beta_x/\beta_x$	ε_x correction	$\Delta\beta_y/\beta_y$	ε_y correction
BEUV (at QS12)	9%	0.92	11%	0.90
Wire-Scanner	4%	0.96	19%	0.84

Table 5.1: Theoretical systematic error in the emittance measurements due to beta-beating at the profile monitors caused by the energy sawtooth at 45.6 GeV and by the pretzel separation (Voltage=100 kV and optics k05p46v3).

- Quadrupole gradient errors create beta-beating with an amplitude of $\Delta\beta/\beta = \pm 10$ -20%. Furthermore, calibration errors of superconducting quadrupoles have a strong effect on β_y^* and on beta-beating (see section 4.6.2).
- Finally, the beta function is affected by the beam-beam interaction. The electromagnetic field generated by all particles in one bunch acts on particles of the other beam creating the effect of a focusing quadrupole in both planes at the interaction point where bunches collide. For a beam-beam tune shift of $\xi = 0.03$, the beta-beating simulated with MAD is about $\Delta\beta/\beta = 30\%$ [54, 60].

5.2 Comparison between luminosity from LEP monitors and from BEUV emittances

The average luminosity measured with LEP monitors at interaction points 2, 4, 6 and 8 and the luminosity calculated using eq. (5.1) with the beam emittances measured with BEUV monitors are plotted in fig. 5.1. Luminosities calculated from BEUV emittances are about 30% lower than measured luminosities. However, the variations of luminosity measured with LEP monitors are correlated with beam size changes observed with BEUV monitors.

These measurements were taken during the fill 2398 on Sept. 30th 1994. The average luminosity agrees within 5% with the average luminosity measured by the LEP experiments.

The values of the beta function at the interaction point used in eq. (5.1) are $\beta_x^* = 2.00$ m and $\beta_y^* = 5.0$ cm. The values of β_y^* can be measured with a precision of 2% using the method described in section 2.1.2. Beam intensities are measured with the beam current transformer [61]. Emittances are measured with the BEUV monitors near quadrupole QS12. For a slit width (part of the optical instrument) of 2.0 mm, the parameter σ_{offset} of eq. (5.3) is 335 μm for the horizontal emittance and 243 μm for the vertical emittance. The beta function values in eq. (5.3) are calculated in a simulation using MAD with the optics file k05p46v3, where the effects of the pretzel separation of 100 kV and of the energy sawtooth are taken into account.

The correction for beta-beating created by pretzel separation and energy sawtooth on the luminosity calculated from the emittances is important. The corrections on the horizontal and vertical emittances (see table 5.1) are about -8% and -10%, respectively. If these corrections are applied to eq. (5.1), the calculated luminosity increases by 10%.

More experiments are on the way in order to study the influence of dispersion and beta-beating on the emittance measurements. In a recent experiment [62] the vertical and horizontal beta functions were measured at the profile monitors using the technique described in chapter 4. Deviations of the measured beta functions from the theoretical values up to 15% have been found at the profile monitors. The luminosities calculated from BEUV emittances

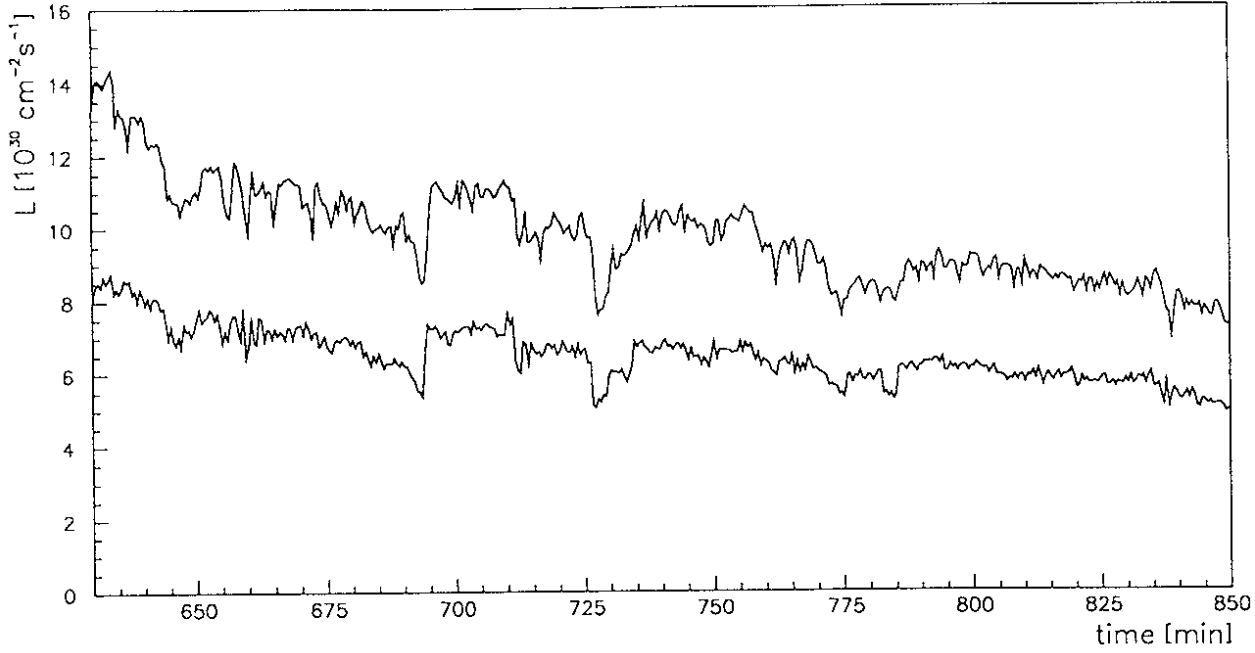


Figure 5.1: Luminosity measured with the LEP monitors (top) and with the BEUV emittances (bottom). The measurements were taken during the fill 2398 on Sept. 30th 1994.

are corrected by about 9% when the measured values of the horizontal and vertical beta functions are used. Vertical and horizontal dispersion at the profile monitors increase the size of the beam

$$\sigma = \sqrt{\beta\epsilon + \left(D\frac{\Delta E}{E}\right)^2}$$

where D is the dispersion function and ΔE is the energy spread of the particles in the beam. The relative energy spread $\Delta E/E$ at 45.6 GeV is about 0.1%. Values of the vertical dispersion between 0.10 and 0.15 m have been measured at BEUV monitors. Since the vertical emittance is around 1-2 nm, the effect of dispersion at BEUV monitors has to be considered in the emittance in order to compare the luminosity from BEUV emittances and the one from the LEP luminosity monitors.

Conclusions

Luminosity measurement. The goal of LEP luminosity monitors to provide the control room with fast luminosity measurements of the four interaction points has been successfully achieved. Their performance has been excellent, and without them the energy scan of 1995 to measure precisely the mass and the width of the Z particle could not have been done [63].

The detector acceptance \bar{N}/\mathcal{L} is $3.8 \pm 0.2 \mu\text{b}$ per monitor at $X = 32.7 \text{ mm}$, with an efficiency of 90%. A simulation showed that the beam divergence at the interaction point reduces the acceptance by 4-6%. It is believed that about 5-10% of Bhabha scattered e^+e^- pairs that hit the detectors are not detected since they hit near the inner edge and the electronic shower is not fully contained.

The number of Bhabha scattered e^+e^- pairs detected per interaction point (two monitors) during physics data taking is in the range of 40-80 Hz for typical luminosity values between 8 and $15 \cdot 10^{30} \text{ cm}^{-2}\text{s}^{-1}$.

Particle background rates received at the detectors are two or three orders higher than the Bhabha scattering rate. The protection provided by collimators at the arcs is very effective and leads to a reduction factor of 6-7 for internal detectors and a factor of 4 for external detectors. The longitudinal position of these collimators must be adapted to the optics, i.e. to the phase advance between them and the detectors.

The measured Bhabha scattering rate is affected by accidental background coincidences in the same bunch crossing. The accidental coincidence rate is calculated from internal and external background rates. A second order probability calculation takes care of the situation with high background rates to avoid systematic errors in the subtraction of the accidental coincidence rate. It has been shown that this procedure is more accurate than the measurement of delayed coincidences.

Particle background affects the luminosity measurements by increasing the statistical error. Its contribution has been calculated and applied to the data obtaining a very good error estimate.

The use of DSPs (Digital Signal Processor) makes the determination of signal thresholds easier by taking the detector signal histograms to produce the Bhabha scattering rate and its error as functions of the threshold values.

An automatic procedure has been developed to determine the electrostatic separator voltage required to collide the electron and the positron beams head-on (procedure known as the Vernier scan) using the LEP luminosity monitors. This procedure synchronizes the change of voltage of the electrostatic separators and the reading of luminosity monitors in order to obtain results within 3-5 minutes.

In the second phase of LEP, at energies of 90 GeV, the detector acceptance will decrease by a factor of about 5 to 8 and particle background rates will increase by a factor of 2. This affects the statistical precision of luminosity measurements and the acquisition time is increased. Still, the monitors will provide the most accurate luminosity measurements in short intervals of time.

Beam size monitoring. The variations of luminosity measurements and beam size measurements have been shown to be correlated. Various experiments on the cross-calibration of the beam profile monitors, where beta function measurements were used, have provided a better knowledge on the absolute calibration of the ultraviolet telescopes which is affected by both residual vertical dispersion and beta-beating.

Phase and beta functions measurement. A precise method to measure the phase and the beta functions was developed. This method uses the betatron phase of coherent beam oscillations measured at 504 beam position monitors by sampling the beam position for 1024 turns. For beam oscillations of 2-3 mm, the phase obtained by harmonic analysis has an accuracy of 0.14° . The expressions to extract the phase and the beta functions from phase measurements at three beam position monitors are derived and examples are shown. The expression of the error of measured phase and beta functions are derived from the phase errors at the three monitors. The equations show that the beta function measurement error is related to the phase advance between the beam position monitors. The minimum error contribution from the phase error can be obtained if this phase advance is $\Delta\phi = 60^\circ$. At LEP, vertical beta function measurements were obtained with a precision of 0.4% in the arcs.

The method allows to measure the beta mismatch between the beta function for the real machine and the beta function of the model of the perfect machine. At LEP, for squeezed optics at 45.6 GeV, a beta-beating amplitude about 15-25% has been found.

The method has been used to measure the effect of quadrupole gradient errors, pretzel separation and energy sawtooth on the phase and the beta functions. The results agree well with the simulations made with MAD program.

The method to measure the phase and the beta functions has been used at LEP to check the optics. It also permits to check the beta function at beam position monitors for calibration of their scaling factors, at collimators to check their distance relative to the beam size, and at beam profile monitors to correlate their emittance measurements.

The accuracy of the phase measurements has allowed precise measurements of:

- The beam energy dependence of the phase function due to the chromaticity. The measurements show in detail the chromaticity correction by the sextupoles in the arcs.
- The bunch current dependence of the phase function due to the impedance of the vacuum chamber. The results were used to check the impedance model of LEP.

The application of measured beta function in order to correct quadrupole gradient errors is under study. Some tests were carried out to match the beta measurements with MAD and to use a modified version of the closed orbit correction program COCU [64] (with the MICADO algorithm) adapted to this purpose [52]. More studies are under way.

An important outcome of the measurement error analysis is the dependence of beta function measurements on the phase advance between beam position monitors. In future accelerators where beta function measurements are required, the design of the phase advance between monitors should be as close to 60° or 120° as possible, to obtain the best ratio beta measurement error over phase measurement error. Phase advance between position monitors of 90° makes beta function measurements impossible. It can also slightly deteriorate the closed orbit correction, which could decrease the performance in a storage ring.

Appendix A

Overlap of two Gaussian distributions

The event rate for a given process with cross section σ in the collision of two beams is given by

$$\dot{N} = \mathcal{L} \sigma .$$

If the beams have uniform particle distribution over the area A with N_b being the number of particles, the probability that a particle from the first beam hits a particle (with cross section σ for this process) of the other beam is $N_b \sigma / A$. Multiplying by N_b we have the number of events in one collision (head-on)

$$N = \frac{N_b^2}{A} \sigma .$$

If each beam has k_b bunches and the revolution frequency is f_{rev} , the event rate is given by

$$\dot{N} = k_b f_{rev} \frac{N_b^2}{A} \sigma .$$

The luminosity is

$$\mathcal{L} = k_b f_{rev} \frac{N_b^2}{A} ,$$

which can be rewritten in terms of the transverse particle density $\rho = N_b / A$ as

$$\mathcal{L} = k_b f_{rev} \rho^2 A .$$

When the particle density distribution is not uniform, the collision area A can be divided in elementary surfaces $dx dy$ which contribute with a differential luminosity

$$d\mathcal{L} = k_b f_{rev} \rho^2(x, y) dx dy .$$

The luminosity of two beams colliding head-on with different particle distributions can be written as

$$\mathcal{L} = k_b f_{rev} \int_{-\infty}^{\infty} \int_{-\infty}^{\infty} \rho_1(x, y) \rho_2(x, y) dx dy$$

where k_b is the number of bunches per beam, f_{rev} is the revolution frequency and ρ_1, ρ_2 are the transverse particle distribution of the first and second beam. In the case of LEP, high relativistic electron and positron beams have Gaussian profiles and their transverse particle distribution can be written

$$\rho(x, y) = N_b g(x, \sigma_x) g(y, \sigma_y) ,$$

where

$$g(u, \sigma_u) = \frac{1}{\sigma_u \sqrt{2\pi}} \exp\left(-\frac{u^2}{2\sigma_u^2}\right), \quad u = x, y.$$

If beams are colliding perfectly head-on, i.e. the centers of particle distributions coincide, the luminosity can be computed using the solution of the overlap integral of the Gaussian distributions

$$\begin{aligned} \int_{-\infty}^{\infty} g(x, \sigma_1) g(x, \sigma_2) dx &= \frac{1}{2\pi\sigma_1\sigma_2} \int_{-\infty}^{\infty} \exp\left(-\frac{x^2}{2\sigma_1^2} - \frac{x^2}{2\sigma_2^2}\right) dx \\ &= \frac{1}{2\pi\sigma_1\sigma_2} \int_{-\infty}^{\infty} \exp\left(-\frac{x^2}{2\left(\frac{\sigma_1^2\sigma_2^2}{\sigma_1^2+\sigma_2^2}\right)}\right) dx \\ &= \frac{1}{\sqrt{2\pi(\sigma_1^2 + \sigma_2^2)}}. \end{aligned}$$

Integrating over x and y the luminosity is given by

$$\mathcal{L} = \frac{k_b f_{rev} N_1 N_2}{2\pi \sqrt{(\sigma_{x1}^2 + \sigma_{x2}^2)(\sigma_{y1}^2 + \sigma_{y2}^2)}}, \quad (\text{A.1})$$

where N_1 and N_2 are the number of particles per bunch at the first and the second beam, respectively. When the size of both beams are identical, the luminosity is

$$\mathcal{L} = \frac{k_b f_{rev} N_1 N_2}{4\pi \sigma_x \sigma_y}.$$

The overlap integral of two Gaussian distributions with centers separated by a distance d is

$$\int_{-\infty}^{\infty} g(x, \sigma_1) g(x-d, \sigma_2) dx dy = \frac{1}{2\pi\sigma_1\sigma_2} \int_{-\infty}^{\infty} \exp\left(-\frac{x^2}{2\sigma_1^2} - \frac{(x-d)^2}{2\sigma_2^2}\right) dx \quad (\text{A.2})$$

where the expression in the exponent can be written as

$$\begin{aligned} -\frac{x^2}{2\sigma_1^2} - \frac{(x-d)^2}{2\sigma_2^2} &= -\frac{1}{2\sigma_1^2\sigma_2^2} (\sigma_1^2 x^2 + \sigma_2^2 x^2 - 2\sigma_1^2 x d + \sigma_1^2 d^2) \\ &= -\frac{\sigma_1^2 + \sigma_2^2}{2\sigma_1^2\sigma_2^2} \left(x^2 - \frac{2\sigma_1^2 d}{\sigma_1^2 + \sigma_2^2} x + \frac{\sigma_1^2 d^2}{\sigma_1^2 + \sigma_2^2} \right) \\ &= -\frac{\sigma_1^2 + \sigma_2^2}{2\sigma_1^2\sigma_2^2} \left[\left(x - \frac{\sigma_1^2 d}{\sigma_1^2 + \sigma_2^2} \right)^2 - \frac{\sigma_1^4 d^2}{(\sigma_1^2 + \sigma_2^2)^2} + \frac{\sigma_1^2 d^2}{\sigma_1^2 + \sigma_2^2} \right] \\ &= -\frac{\sigma_1^2 + \sigma_2^2}{2\sigma_1^2\sigma_2^2} \left[\left(x - \frac{\sigma_1^2 d}{\sigma_1^2 + \sigma_2^2} \right)^2 + \frac{\sigma_1^2 \sigma_2^2 d^2}{(\sigma_1^2 + \sigma_2^2)^2} \right] \\ &= -\frac{d^2}{2(\sigma_1^2 + \sigma_2^2)} - \frac{\sigma_1^2 + \sigma_2^2}{2\sigma_1^2\sigma_2^2} \left(x - \frac{\sigma_1^2 d}{\sigma_1^2 + \sigma_2^2} \right)^2. \end{aligned}$$

The right hand side of eq. (A.2) becomes

$$\frac{1}{2\pi\sigma_1\sigma_2} \exp\left(-\frac{d^2}{2(\sigma_1^2 + \sigma_2^2)}\right) \int_{-\infty}^{\infty} \exp\left[-\frac{\sigma_1^2 + \sigma_2^2}{2\sigma_1^2\sigma_2^2} \left(x - \frac{\sigma_1^2 d}{\sigma_1^2 + \sigma_2^2} \right)^2\right] dx.$$

The solution of the integral of eq. (A.2) is

$$\int_{-\infty}^{\infty} g(x, \sigma_1) g(x - d, \sigma_2) dx = \frac{1}{\sqrt{2\pi(\sigma_1^2 + \sigma_2^2)}} \exp\left(-\frac{d^2}{2(\sigma_1^2 + \sigma_2^2)}\right) .$$

The luminosity of two beams colliding with particle distribution centers separated by a distance d_x in the horizontal plane and by a distance d_y in the vertical plane is

$$\mathcal{L} = \frac{k_b f_{rev} N_1 N_2}{2\pi \sqrt{(\sigma_{x_1}^2 + \sigma_{x_2}^2)(\sigma_{y_1}^2 + \sigma_{y_2}^2)}} \exp\left(-\frac{d_x^2}{2(\sigma_{x_1}^2 + \sigma_{x_2}^2)} - \frac{d_y^2}{2(\sigma_{y_1}^2 + \sigma_{y_2}^2)}\right) .$$

Vertical beam separation scan

With *Vernier scans* the luminosity is measured as a function of the vertical beam separation d_y

$$\mathcal{L} = \frac{k_b f_{rev} N_1 N_2}{2\pi \sqrt{(\sigma_{x_1}^2 + \sigma_{x_2}^2)(\sigma_{y_1}^2 + \sigma_{y_2}^2)}} \exp\left(-\frac{d_y^2}{2(\sigma_{y_1}^2 + \sigma_{y_2}^2)}\right) ,$$

which can be written as

$$\mathcal{L} = \frac{k_b f_{rev} N_1 N_2}{\sqrt{2\pi(\sigma_{x_1}^2 + \sigma_{x_2}^2)}} g(d_y, \sqrt{\sigma_{y_1}^2 + \sigma_{y_2}^2}) ,$$

which represents a Gaussian distribution of peak height equal to eq. (A.1) and width

$$\sigma_{\text{scan}} = \sqrt{\sigma_{y_1}^2 + \sigma_{y_2}^2} . \quad (\text{A.3})$$

If equal beam sizes are assumed

$$\mathcal{L} = \frac{k_b f_{rev} N_1 N_2}{2\sqrt{\pi}\sigma_x} g(d_y, \sqrt{2}\sigma_y)$$

and the width of the Vernier scan becomes $\sqrt{2}\sigma_y$. Examples of Vernier scans are shown in figs. 3.21 and 3.22.

Appendix B

Integral of the Bhabha scattering cross section over a rectangular detector

Since particle trajectories in the vertical and in the horizontal plane are independent and the detector area is square, the horizontal and vertical limits of the double integral in eq. (3.4) do not depend on each other and the integral can be split in two parts

$$\dot{N} = \mathcal{L} \frac{4\alpha^2}{E^2} \int_{x'_1}^{x'_2} dx' \int_{y'_1}^{y'_2} \frac{dy'}{(x'^2 + y'^2)^2} . \quad (\text{B.1})$$

The integral in y' gives

$$\int_{y'_1}^{y'_2} \frac{dy'}{(x'^2 + y'^2)^2} = \frac{1}{2} \left[\frac{y'}{x'^2(x'^2 + y'^2)} + \frac{1}{x'^3} \arctan \frac{y'}{x'} \right]_{y'_1}^{y'_2}$$

which is substituted in eq. (B.1) to give

$$\dot{N} = \mathcal{L} \frac{4\alpha^2}{E^2} \frac{1}{2} \left[y' \int_{x'_1}^{x'_2} \frac{dx'}{x'^2(x'^2 + y'^2)} + \int_{x'_1}^{x'_2} \arctan \frac{y'}{x'} \frac{dx'}{x'^3} \right]_{y'_1}^{y'_2} . \quad (\text{B.2})$$

In the case that $y' = 0$ the expression between brackets in eq. (B.2) is zero. For non-zero y' limits, the solution for the first integral in x' of eq. (B.2) is

$$\begin{aligned} \int_{x'_1}^{x'_2} \frac{dx'}{x'^2(x'^2 + y'^2)} &= \frac{1}{y'^2} \left(\int_{x'_1}^{x'_2} \frac{dx'}{x'^2} - \int_{x'_1}^{x'_2} \frac{dx'}{x'^2 + y'^2} \right) \\ &= \frac{1}{y'^2} \left[-\frac{1}{x'} - \frac{1}{y'} \arctan \frac{x'}{y'} \right]_{x'_1}^{x'_2} . \end{aligned} \quad (\text{B.3})$$

The second integral in x' of eq. (B.2) is solved substituting y'/x' by v

$$dv = -\frac{y'}{x'^2} dx'$$

thus

$$\int_{x'_1}^{x'_2} \arctan \frac{y'}{x'} \frac{dx'}{x'^3} = -\frac{1}{y'^2} \int_{v_1}^{v_2} v \arctan v \, dv \quad (\text{B.4})$$

where

$$v_1 = \frac{y'}{x'_1} \quad \text{and} \quad v_2 = \frac{y'}{x'_2}.$$

The integral of the right hand-side of eq. (B.4) is solved by

$$\int_{v_1}^{v_2} v \arctan v \, dv = \frac{1}{2} \left[(v^2 + 1) \arctan v - v \right]_{v_1}^{v_2}.$$

Then eq. (B.4) becomes

$$\int_{x'_1}^{x'_2} \arctan \frac{y'}{x'} \frac{dx'}{x'^3} = \frac{1}{2} \left[\frac{1}{x'y'} - \left(\frac{1}{x'^2} + \frac{1}{y'^2} \right) \arctan \frac{y'}{x'} \right]_{x'_1}^{x'_2}. \quad (\text{B.5})$$

Finally, substituting eqs. (B.3) and (B.5) into eq. (B.2) and using

$$\arctan x + \arctan \frac{1}{x} = \frac{\pi}{2} \text{sign}(x)$$

yield

$$\dot{N} = \mathcal{L} \frac{4\alpha^2}{E^2} \left[\left[-\frac{1}{4} \frac{1}{x'y'} - \frac{1}{4} \left(\frac{1}{x'^2} - \frac{1}{y'^2} \right) \arctan \frac{y'}{x'} - \frac{\pi}{4} \frac{1}{y'^2} \text{sign}(x'y') \right]_{y'_1}^{y'_2} \right]_{x'_1}^{x'_2}$$

where the last factor of the right hand-side $-(\pi/4y'^2) \text{sign}(x'y')$ is constant for $x'_1, x'_2 > 0$. The integration of eq. (B.1) gives

$$\dot{N} = \mathcal{L} \frac{\alpha^2}{E^2} \left[\left[-\frac{1}{x'y'} - \left(\frac{1}{x'^2} - \frac{1}{y'^2} \right) \arctan \frac{y'}{x'} \right]_{y'_1}^{y'_2} \right]_{x'_1}^{x'_2}.$$

Appendix C

Transformation of β and α using the phase advance ϕ_{12}

We are particularly interested in the expressions of β_2 and α_2 from eq. (2.9)

$$\beta_2 = m_{11}^2 \beta_1 - 2m_{11}m_{12}\alpha_1 + m_{12}^2 \gamma_1 \quad (\text{C.1})$$

and

$$\alpha_2 = -m_{11}m_{21}\beta_1 + (1 + 2m_{12}m_{21})\alpha_1 - m_{12}m_{22}\gamma_1 \quad (\text{C.2})$$

Using eq. (2.7), we replace $m_{11}\beta_1$ by $m_{12}(\cot \phi_{12} + \alpha_1)$ in eq. (C.1)

$$\begin{aligned} \beta_2 &= m_{11}m_{12}(\cot \phi_{12} + \alpha_1) - 2m_{11}m_{12}\alpha_1 + m_{12}^2 \gamma_1 \\ &= m_{11}m_{12}(\cot \phi_{12} - \alpha_1) + m_{12}^2 \gamma_1 \quad . \end{aligned}$$

Replacing m_{11} by $m_{12}(\cot \phi_{12} + \alpha_1)/\beta_1$ and γ_1 by $(1 + \alpha_1^2)/\beta_1$ yields

$$\begin{aligned} \beta_2 &= \frac{m_{12}^2}{\beta_1}(\cot \phi_{12} + \alpha_1)(\cot \phi_{12} - \alpha_1) + m_{12}^2 \frac{1 + \alpha_1^2}{\beta_1} \\ &= \frac{m_{12}^2}{\beta_1}(\cot^2 \phi_{12} - \alpha_1^2) + m_{12}^2 \frac{1 + \alpha_1^2}{\beta_1} \\ &= \frac{m_{12}^2}{\beta_1}(\cot^2 \phi_{12} + 1) \\ &= \frac{m_{12}^2}{\beta_1 \sin^2 \phi_{12}} \end{aligned}$$

which is eq. (2.11).

The product $m_{11}\beta_1$ can be replaced by $m_{12}(\cot \phi_{12} + \alpha_1)$ in eq. (C.2) to obtain

$$\alpha_2 = -m_{12}m_{21}(\cot \phi_{12} + \alpha_1) + (1 + 2m_{12}m_{21})\alpha_1 - m_{12}m_{22}\gamma_1$$

which gives

$$\alpha_2 = \alpha_1 - m_{12}m_{21}(\cot \phi_{12} - \alpha_1) - m_{12}m_{22}\gamma_1 \quad .$$

Since the determinant of the transfer matrix is

$$\det(M) = m_{11}m_{22} - m_{12}m_{21} = 1$$

the equation for α_2 can be expressed as

$$\begin{aligned}\alpha_2 &= \alpha_1 - (m_{11}m_{22} - 1)(\cot \phi_{12} - \alpha_1) - m_{12}m_{22}\gamma_1 \\ &= \cot \phi_{12} - m_{11}m_{22}(\cot \phi_{12} - \alpha_1) - m_{12}m_{22}\gamma_1 .\end{aligned}$$

Replacing again m_{11} by $m_{12}(\cot \phi_{12} + \alpha_1)/\beta_1$ and γ_1 by $(1 + \alpha_1^2)/\beta_1$ yields

$$\begin{aligned}\alpha_2 &= \cot \phi_{12} - \frac{m_{12}m_{22}}{\beta_1}(\cot \phi_{12} + \alpha_1)(\cot \phi_{12} - \alpha_1) - m_{12}m_{22}\frac{1 + \alpha_1^2}{\beta_1} \\ &= \cot \phi_{12} - \frac{m_{12}m_{22}}{\beta_1 \sin^2 \phi_{12}} .\end{aligned}$$

Using eq. (2.11), we replace $\beta_1 \sin^2 \phi_{12}$ by m_{12}^2/β_2 to obtain

$$\alpha_2 = \cot \phi_{12} - \beta_2 \frac{m_{22}}{m_{12}} .$$

Appendix D

Measured alpha function at beam position monitors

The expressions of the function alpha corresponding to the solution of the systems of equations mentioned in section 4.2 are:

$$\begin{aligned}\alpha'_1 &= \frac{(c_{11}/c_{12}) \cot \phi'_{12} - (a_{11}/a_{12}) \cot \phi'_{13}}{(a_{11}/a_{12}) - (c_{11}/c_{12})} \\ &= \frac{a_{12}c_{11}}{b_{12}} \cot \phi'_{12} - \frac{a_{11}c_{12}}{b_{12}} \cot \phi'_{13}\end{aligned}\quad (\text{D.1})$$

$$\begin{aligned}\alpha'_2 &= \frac{(b_{11}/b_{12}) \cot \phi'_{12} - (a_{22}/a_{12}) \cot \phi'_{23}}{(a_{22}/a_{12}) + (b_{11}/b_{12})} \\ &= \frac{a_{12}b_{11}}{c_{12}} \cot \phi'_{12} - \frac{a_{22}b_{12}}{c_{12}} \cot \phi'_{23}\end{aligned}\quad (\text{D.2})$$

$$\begin{aligned}\alpha'_3 &= \frac{(b_{22}/b_{12}) \cot \phi'_{13} - (c_{22}/c_{12}) \cot \phi'_{23}}{(b_{22}/b_{12}) - (c_{22}/c_{12})} \\ &= \frac{b_{22}c_{12}}{a_{12}} \cot \phi'_{13} - \frac{b_{12}c_{22}}{a_{12}} \cot \phi'_{23}.\end{aligned}\quad (\text{D.3})$$

Replacing a_{11}/a_{12} by $(\cot \phi_{12} + \alpha_1)/\beta_1$ and c_{11}/c_{12} by $(\cot \phi_{13} + \alpha_1)/\beta_1$ in eq. (D.1), we get

$$\alpha'_1 = \frac{(\cot \phi_{13} + \alpha_1) \cot \phi'_{12} - (\cot \phi_{12} + \alpha_1) \cot \phi'_{13}}{\cot \phi_{12} - \cot \phi_{13}}, \quad (\text{D.4})$$

replacing a_{22}/a_{12} by $(\cot \phi_{12} - \alpha_2)/\beta_2$ and b_{11}/b_{12} by $(\cot \phi_{23} + \alpha_2)/\beta_2$ in eq. (D.2), we obtain

$$\alpha'_2 = \frac{(\cot \phi_{23} + \alpha_2) \cot \phi'_{12} - (\cot \phi_{12} - \alpha_2) \cot \phi'_{23}}{\cot \phi_{12} + \cot \phi_{23}}$$

and replacing c_{22}/c_{12} by $(\cot \phi_{13} - \alpha_3)/\beta_3$ and b_{22}/b_{12} by $(\cot \phi_{23} - \alpha_3)/\beta_3$, eq. (D.3) yields

$$\alpha'_3 = \frac{(\cot \phi_{23} - \alpha_3) \cot \phi'_{13} - (\cot \phi_{13} - \alpha_3) \cot \phi'_{23}}{\cot \phi_{23} - \cot \phi_{13}}.$$

Error of the function alpha at s_1 , s_2 and s_3

The error of α'_1 in eq. (D.1) is given by

$$\sigma_{\alpha'_1} = \sqrt{\left(\frac{a_{12}c_{11}}{b_{12}\sin^2 \phi'_{12}} - \frac{a_{11}c_{12}}{b_{12}\sin^2 \phi'_{13}}\right)^2 \sigma_{\phi'_1}^2 + \left(\frac{a_{12}c_{11}\sigma_{\phi'_2}}{b_{12}\sin^2 \phi'_{12}}\right)^2 + \left(\frac{a_{11}c_{12}\sigma_{\phi'_3}}{b_{12}\sin^2 \phi'_{13}}\right)^2} \quad (\text{D.5})$$

the error of α'_2 is

$$\sigma_{\alpha'_2} = \sqrt{\left(\frac{a_{12}b_{11}\sigma_{\phi'_1}}{c_{12}\sin^2\phi'_{12}}\right)^2 + \left(\frac{a_{12}b_{11}}{c_{12}\sin^2\phi'_{12}} + \frac{a_{22}b_{12}}{c_{12}\sin^2\phi'_{23}}\right)^2 \sigma_{\phi'_2}^2 + \left(\frac{a_{22}b_{12}\sigma_{\phi'_3}}{c_{12}\sin^2\phi'_{23}}\right)^2} \quad (D.6)$$

and the error of α'_3 is

$$\sigma_{\alpha'_3} = \sqrt{\left(\frac{b_{22}c_{12}\sigma_{\phi'_1}}{a_{12}\sin^2\phi'_{13}}\right)^2 + \left(\frac{b_{12}c_{22}\sigma_{\phi'_2}}{a_{12}\sin^2\phi'_{23}}\right)^2 + \left(\frac{b_{22}c_{12}}{a_{12}\sin^2\phi'_{13}} - \frac{b_{12}c_{22}}{a_{12}\sin^2\phi'_{23}}\right)^2 \sigma_{\phi'_3}^2} \quad (D.7)$$

The matrix elements in these expressions can be replaced by the optics functions of the unperturbed machine in order to obtain the errors

$$\begin{aligned} \sigma_{\alpha'_1} &= \frac{1}{E_1} \sqrt{\left[\frac{(\cot\phi_{13} + \alpha_1)}{\sin^2\phi'_{12}} - \frac{(\cot\phi_{12} + \alpha_1)}{\sin^2\phi'_{13}}\right]^2 \sigma_{\phi'_1}^2 + \left[\frac{(\cot\phi_{13} + \alpha_1)\sigma_{\phi'_2}}{\sin^2\phi'_{12}}\right]^2 + \left[\frac{(\cot\phi_{12} + \alpha_1)\sigma_{\phi'_3}}{\sin^2\phi'_{13}}\right]^2} \\ \sigma_{\alpha'_2} &= \frac{1}{E_2} \sqrt{\left[\frac{(\cot\phi_{23} + \alpha_2)\sigma_{\phi'_1}}{\sin^2\phi'_{12}}\right]^2 + \left[\frac{(\cot\phi_{23} + \alpha_2)}{\sin^2\phi'_{12}} + \frac{(\cot\phi_{12} - \alpha_2)}{\sin^2\phi'_{23}}\right]^2 \sigma_{\phi'_2}^2 + \left[\frac{(\cot\phi_{12} - \alpha_2)\sigma_{\phi'_3}}{\sin^2\phi'_{23}}\right]^2} \\ \sigma_{\alpha'_3} &= \frac{1}{E_3} \sqrt{\left[\frac{(\cot\phi_{23} - \alpha_3)\sigma_{\phi'_1}}{\sin^2\phi'_{13}}\right]^2 + \left[\frac{(\cot\phi_{13} - \alpha_3)\sigma_{\phi'_2}}{\sin^2\phi'_{23}}\right]^2 + \left[\frac{(\cot\phi_{23} - \alpha_3)}{\sin^2\phi'_{13}} - \frac{(\cot\phi_{13} - \alpha_3)}{\sin^2\phi'_{23}}\right]^2 \sigma_{\phi'_3}^2} \end{aligned}$$

where

$$\begin{aligned} E_1 &= |\cot\phi_{12} - \cot\phi_{13}| \\ E_2 &= |\cot\phi_{12} + \cot\phi_{23}| \\ E_3 &= |\cot\phi_{23} - \cot\phi_{13}| \end{aligned}$$

Appendix E

Harmonic analysis of beam oscillations

The position of an oscillating beam observed at a single point in the storage ring is described in eq. (4.2). The harmonic analysis (see section 4.3) of the transverse beam position u provides the best estimates of the amplitude A and the phase ϕ of eq. (4.2). The analysis of the harmonic $\omega = 2\pi q$ is carried out by computing the real (cosine) and the complex (sine) part of the value $\mathcal{F}(2\pi q i)$ of eq. (4.13)

$$C = \sum_{i=0}^{N-1} u_i \cos(2\pi q i) \quad (\text{E.1})$$

$$S = \sum_{i=0}^{N-1} u_i \sin(2\pi q i) . \quad (\text{E.2})$$

Replacing u_i by eq. (4.2) in the expression of C , we get

$$\begin{aligned} C &= \sum_{i=0}^{N-1} [A \cos(2\pi q i + \phi) + u_{co}] \cos(2\pi q i) \\ C &= A \sum_{i=0}^{N-1} \cos(2\pi q i + \phi) \cos(2\pi q i) + u_{co} \sum_{i=0}^{N-1} \cos(2\pi q i) . \end{aligned}$$

For a large number of samples N , the second sum of cosine terms with random phases vanishes and

$$\begin{aligned} C &= A \sum_{i=0}^{N-1} \frac{\cos(2\pi q i + \phi) \cos(2\pi q i)}{\cos(2\pi q i) \cos \phi - \sin(2\pi q i) \sin \phi} \\ &= A \sum_{i=0}^{N-1} \left[\frac{\cos^2(2\pi q i)}{\frac{1}{2} + \frac{1}{2} \cos 4\pi q i} \cos \phi - \frac{\sin(2\pi q i) \cos(2\pi q i) \sin \phi}{\frac{1}{2} \sin(4\pi q i)} \right] \\ &= A \left[\frac{N}{2} \cos \phi + \frac{1}{2} \sum_{i=0}^{N-1} [\cos(4\pi q i) \cos \phi - \sin(4\pi q i) \sin \phi] \right] \\ &= \frac{A N}{2} \left[\cos \phi + \frac{1}{N} \sum_{i=0}^{N-1} \cos(4\pi q i + \phi) \right] \\ &\approx \frac{A N \cos \phi}{2} , \end{aligned}$$

since the second sum of cosine terms vanishes for a large N . Doing similarly for S , one gets

$$\begin{aligned} S &= \frac{AN}{2} \left[-\sin \phi + \frac{1}{N} \sum_{i=0}^{N-1} \sin(4\pi q i + \phi) \right] \\ &= \frac{-AN \sin \phi}{2} . \end{aligned}$$

Neglecting second order terms which vanish for large N , the amplitude A and the phase ϕ of the complex function \mathcal{F} can be obtained by

$$A = \frac{2\sqrt{C^2 + S^2}}{N} \quad \phi = -\arctan\left(\frac{S}{C}\right) ,$$

where the quadrant of the phase ϕ can be found by the signs of S and C

sign S	sign C	quadrant of ϕ
-	+	$0 < \phi < \frac{\pi}{2}$
-	-	$\frac{\pi}{2} < \phi < \pi$
+	-	$\pi < \phi < \frac{3\pi}{2}$
+	+	$\frac{3\pi}{2} < \phi < 2\pi$

Statistical errors of the amplitude and the phase

The error on A and ϕ due to beam position noise σ can be calculated by error propagation when the statistical error of S and C are uncorrelated

$$\sigma_A = \sqrt{\left(\frac{\partial A}{\partial S}\right)^2 \sigma_S^2 + \left(\frac{\partial A}{\partial C}\right)^2 \sigma_C^2} \quad (\text{E.3})$$

$$\sigma_\phi = \sqrt{\left(\frac{\partial \phi}{\partial S}\right)^2 \sigma_S^2 + \left(\frac{\partial \phi}{\partial C}\right)^2 \sigma_C^2} \quad (\text{E.4})$$

where

$$\begin{aligned} \frac{\partial A}{\partial S} &= \frac{2S}{N\sqrt{C^2 + S^2}} , & \frac{\partial A}{\partial C} &= \frac{2C}{N\sqrt{C^2 + S^2}} , \\ \frac{\partial \phi}{\partial S} &= \frac{-S}{C^2 + S^2} , & \frac{\partial \phi}{\partial C} &= \frac{C}{C^2 + S^2} . \end{aligned}$$

The error contribution to C comes from the statistical error of the measured position σ

$$\begin{aligned} \sigma_C &= \sqrt{\sum_{i=0}^{N-1} \left[\frac{\partial(u_i \cos(2\pi q i))}{\partial u_i} \right]^2 \sigma^2} \\ &= \sigma \sqrt{\sum_{i=0}^{N-1} \cos^2(2\pi q i)} \\ &\simeq \sigma \sqrt{N \langle \cos^2 x \rangle} \end{aligned}$$

where $\langle \rangle$ indicates the average value of the function $\cos^2 x$

$$\langle \cos^2 x \rangle = \frac{1}{2\pi} \int_{-\pi}^{\pi} \cos^2 x \, dx = \frac{1}{2} .$$

Therefore

$$\sigma_C = \sqrt{\frac{N}{2}} \sigma \quad .$$

Proceeding similarly with S yields

$$\sigma_S^2 = \frac{N}{2} \sigma^2 \quad .$$

Using this result in eqs. (E.3) and (E.4) we obtain the expression of the error on the amplitude A and the phase ϕ from the position measurement noise σ

$$\sigma_A = \sqrt{\frac{2}{N}} \sigma \qquad \sigma_\phi = \frac{1}{A} \sqrt{\frac{2}{N}} \sigma$$

Appendix F

Corrections of the phase measured at beam position monitors

At LEP, the convention is that the phase and the alpha functions refer to the ones of the positron beam. The measured phase advance between two beam position monitors has to be calculated taking into account whether the acquisition was carried out with a positron bunch or an electron bunch

$$\mu'(s_{i+1}) - \mu'(s_i) = \begin{cases} \phi'_{i+1} - \phi'_i & \text{if measured with positrons} \\ \phi'_i - \phi'_{i+1} & \text{if measured with electrons} \end{cases}$$

in order to have the same sign as the reference phase function.

By definition, the phase function $\mu(s)$ is zero at interaction point 1. The phase advance $\Delta\mu_{LR}$ between a point s_L on the left of IP 1 and a point s_R on the right of IP 1 is given by

$$\Delta\mu_{LR} = \mu(s_L) - \mu(s_R) + 2\pi Q \quad ,$$

where $Q = \mu(C)/2\pi$ is the tune and C the circumference of the ring. This correction has to be applied as well on the measured phase advance between two specific beam position monitors located on both sides of the *start point* of the acquisition. The acquisition is started by the timing module which gives a trigger to all the BOM electronics at the moment when the bunch 1 of both electron and positron beams are about to cross the interaction point 1. Therefore, the acquisition of the position of each bunch starts at different locations and different monitors. The locations of the (in general) 8 bunches of positrons and 8 bunches of electrons at the start of the acquisition are shown in fig. F.1.

For example, if the bunch selected is the positron bunch 1 then the first beam position monitor which starts the acquisition is the first monitor of the L15 electronics located on the left side of interaction point 1, and the last monitor to see this bunch is the last one of the A12 electronics. So the phase advance between them must be corrected by $+2\pi q$, with q being the fractional part of the tune Q .

Due to a trigger delay, the electronics which is located at the following arc downstream the *start point* reads systematically the position of the bunch one turn later. The phase measured at the monitors controlled by this electronics have to be corrected by $-2\pi q$. In the case of the positron bunch 1, the electronics starting one turn later is the A22 (five electronics on the right of the *start point*, see fig. F.1). The locations of the *start point* of the acquisition and the delayed electronics for each bunch are listed in table F.1.

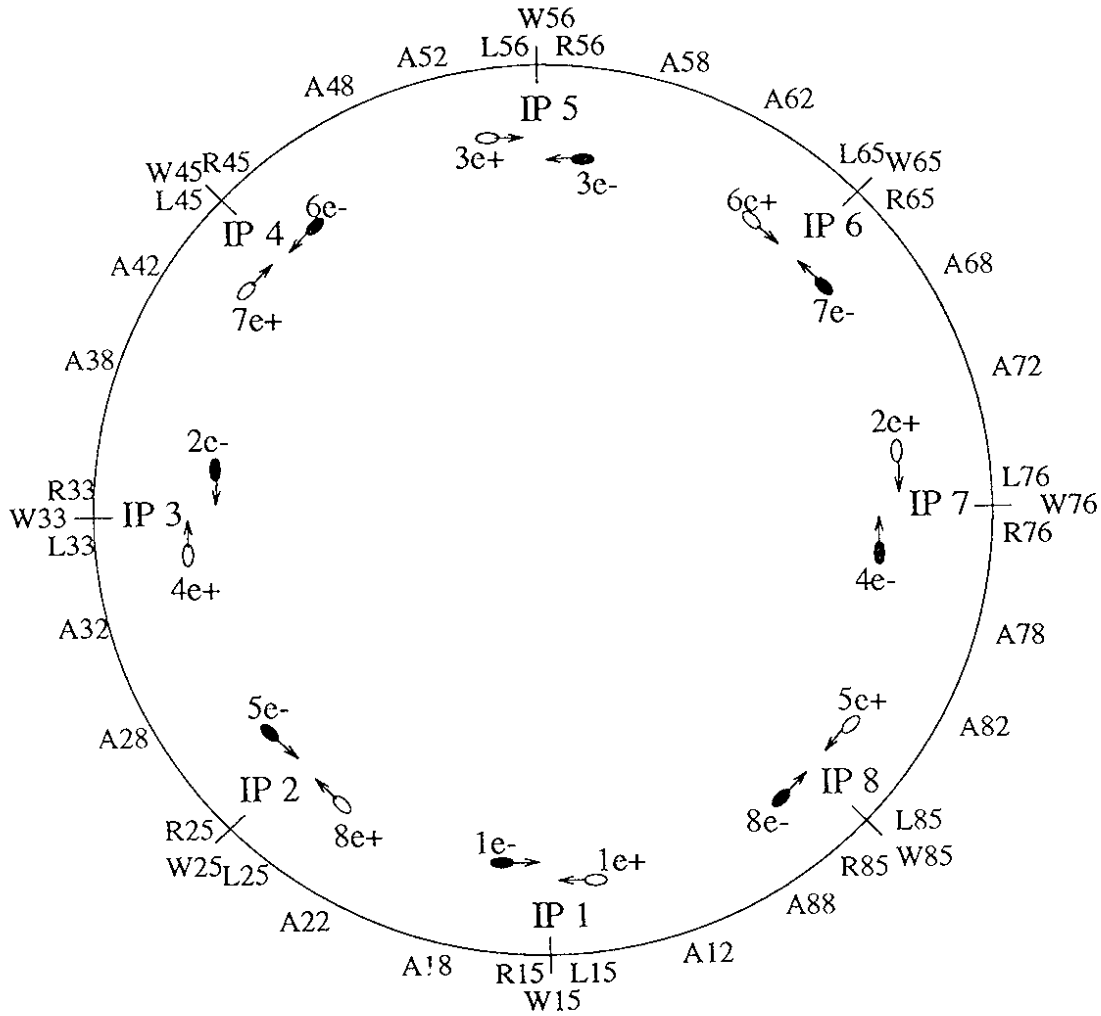


Figure F.1: Location of bunches at the start of BOM acquisition and distribution of BOM electronics (Ai,Ri,Wi,Li).

bunch	positrons		electrons	
	<i>start point</i>	electronics	<i>start point</i>	electronics
1	A12-L15 (left IP 1)	A22	R15-A18 (right IP 1)	A88
2	A72-L76 (left IP 7)	A82	R33-A38 (right IP 3)	A28
3	A52-L56 (left IP 5)	A62	R56-A58 (right IP 5)	A48
4	A32-L33 (left IP 3)	A42	R76-A78 (right IP 7)	A68
5	A82-L85 (left IP 8)	A12	R25-A28 (right IP 2)	A18
6	A62-L65 (left IP 6)	A72	R45-A48 (right IP 4)	A38
7	A42-L45 (left IP 4)	A52	R65-A68 (right IP 6)	A58
8	A22-L25 (left IP 2)	A32	R85-A88 (right IP 8)	A78

Table F.1: Acquisition *start point* and delayed electronics for each specific bunch.

Bibliography

- [1] *LEP Design Report*; CERN-LEP/84-01, Vol. I and II, 1984.
- [2] H. Grote and F.C. Iselin; *The MAD program*; CERN/SL/90-13(AP), 1991.
- [3] D. Brandt, P. Castro, K. Cornelis, A. Hofmann, G. Morpurgo, G.L. Sabbi and A. Verdier; *Measurement of Chromatic Effects in LEP*; Proceedings of the 1995 IEEE Particle Accelerator Conference, Dallas, USA, 1995.
- [4] D. Brandt, P. Castro, K. Cornelis, A. Hofmann, G. Morpurgo, G.L. Sabbi, J. Wenninger and B. Zotter; *Measurement of Impedance Distributions and Instability Thresholds in LEP*; Proceedings of the 1995 IEEE Particle Accelerator Conference, Dallas, USA, 1995.
- [5] P. Castro et al.; *Comparative Precision Emittance Measurements in LEP*; Proceedings of the Fourth European Particle Accelerator Conference, London, 1994, pp. 1637-1639.
- [6] R. Jung; *Precision Emittance Measurements in LEP with Imaging Telescopes, Comparison with Wire Scanner and X-Ray Detector Measurements*; Proceedings of the International Workshop on Particle Dynamics in Accelerators "Emittance in Circular Accelerators", Tsukuba, Japan, 1994.
- [7] P. Castro; *Measured and calculated luminosities at LEP*; CERN SL-MD note 173, 1995.
- [8] *The 300 GeV Programme*; CERN/1050, 1972.
- [9] H. Wiedemann; *Particle Accelerator Physics*; Ed. Springer-Verlag. 1993.
- [10] The LEP Collaborations ALEPH, DELPHI, L3, OPAL and the LEP Electroweak Working Group; *Combined Preliminary Data on Z Parameters from the LEP Experiments and Constraints on the Standard Model*; CERN/PPE/94-187, 1994.
- [11] T. Suzuki; *General Formulae of Luminosity for Various Types of Colliding Beam Machines*; KEK-76-3, 1976.
- [12] K. Potter; *Luminosity measurements and calculations*; CERN 94-01, Vol. I, 1994, pp. 117-129.
- [13] H.G. Hereward; *How good is the r.m.s. as a measure of the beam size?*; CERN/MPS/DL 69-15, 1969.
- [14] E. Keil; *Beam-beam Interactions in p-p storage rings*; Proceedings of the First Course of the International School of Particle Accelerators, Ed. by M.H. Blewett, CERN 77-13, 1977, pp. 314-340.

- [15] F. Amman and D. Ritson; *Space Charge Effects in Electron-Electron and Positron-Electron Colliding or Crossing Beam Rings* Proceedings of the International Conference on High Energy Accelerators, Brookhaven, 1961, p. 471.
- [16] H. Burkhardt, A. Hofmann, Y. Marti, S. Myers and J. Poole; *Comparative Precision Emittance Measurements in LEP*; Proceedings of the Third European Particle Accelerator Conference, Berlin, 1992, pp. 699-701.
- [17] F. Sacherer; *Bunch Lengthening and Microwave Instability*; IEEE Transactions on Nuclear Science Vol. NS-24, N°3, 1977, p. 1393.
- [18] R.D. Kohaupt; *Transverse Instabilities in Petra*; Proceeding of the 11th International Conference on High Energy Accelerators, CERN (1980) EXS Vol.40, Birkhäuser Verlag, p. 562.
- [19] L. Bergström et al.; *Report of the Working Group on High Luminosities at LEP*; Editors E. Blucher, J. Jowett, F. Merit, G. Mikenberg, J. Panman, F.M. Renard and D. Treille. CERN 91-02, 1991.
- [20] W. Herr; *Bunch Trains Without a Crossing Angle*; Proceedings of the Fourth Workshop on LEP Performance, CERN SL/94-6 (DI), Chamonix, 1994, pp. 323-332.
- [21] E.D. Courant and H.S. Snyder; *Theory of the Alternating-Gradient Synchrotron*; Annals of Physics, Vol. 3 (1958), pp. 1-48.
- [22] C. Bovet, R. Gouiran, I. Gumowski and K.H. Reich; *A Selection of Formulae and Data Useful for the Design of A.G. Synchrotrons*; CERN/MDS-SI/Int.DL/70/4, 1970.
- [23] E. Keil; *Single-Particle Dynamics - Linear Machine Imperfections*; Proceedings of the First Course of the International School of Particle Accelerators, Ed. by M.H. Blewett, CERN 77-13, 1977, pp. 52-62.
- [24] H.J. Bhabha; *The Scattering of Positrons and Electrons with Exchange on Dirac's Theory of the Positron*; Proceedings of the Royal Society A154, 195 (1936).
- [25] G. Altarelli, R. Kleiss and C. Verzegnassi; *Z Physics at LEP 1*; CERN Yellow report 89-08, Volume 1, 1989.
- [26] G.P. Ferri, M. Glaser, G. von Holtey and F. Lemeilleur; *Silicon Detectors Used for Beam Diagnostics in the LEP Collider*; CERN/SL 90-110 (BI) (1990) and Nuclear Physics B, Supplements Section (1990).
- [27] Eq. (10.18), p. 1254. Particle Data Group; *Review of Particle Properties*; Physical Review D50, 1173 (1994).
- [28] M.J. Berger and S.M. Seltzer; *Tables of Energy Losses and Ranges of Electrons and Positrons*; National Aeronautics and Space Administration Report NASA-SP-3021, Washington DC, 1964.
- [29] E. Longo and I. Sestili; *Monte Carlo Calculations of Photon-initiated Electromagnetic Showers in Lead Glass*; Nuclear Instruments and Methods 128, 283 (1975).
- [30] R.K. Böck et al.; *Parametrization of Longitudinal Development of Hadronic Showers in Sampling Calorimeters*; Nuclear Instruments and Methods 186, 533 (1981).

- [31] G.P. Ferri, M. Glaser, G. von Holtey and F. Lemeilleur; *Commissioning and Operating Experience with the Interaction Rate and Background Monitors of the LEP e^+e^- Collider*; Proceedings of the First European Particle Accelerator Conference, Nice, France, 1990, pp. 797-799.
- [32] E. Occelli; *Analisi del funzionamento del Calorimetro Bhabha in LEP*; Laurea Thesis at the Politecnico di Torino, 1991.
- [33] Modules DSP 8150 and ADC 8160. CES Creative Electronic Systems SA, 70 Route du Pont-Butin, P.O. Box 107. CH-1213 Petit-Lancy 1, Switzerland.
- [34] P. Castro, L. Knudsen and R. Schmidt; *The Use of Digital Signal Processors in LEP Beam Instrumentation*; Proceedings of the 3rd Annual Accelerator Instrumentation Workshop (no. 252), CEBAF, Newport News, USA, 1991, pp. 207-216.
- [35] H. Burkhardt; *Lifetime and Beam-beam Limit*; Presentation 35, Proceedings of the 4th Workshop on LEP Performance, Ed. J. Poole, CERN SL/94-06(DI), 1994, pp. 253-259.
- [36] Program RG32. F. James; *CERN Program Library V108*; Ed. G. Benassi, 1989, p. 6.464.
- [37] J.Y. Hemery, F. Lemeilleur, G. von Holtey; *An Interaction Rate Monitor for LEP*; CERN/LEP-BI/86-5, 1986.
- [38] V.I. Telnov; *Scattering of Electrons on Thermal Radiation Photons in Electron-Positron Storage Rings*; CERN Preprint 86-175, 1986.
- [39] B. Dehning, A.C. Melissinos, F. Perrone, C. Rizzo and G. von Holtey; *Scattering of High Energy Electrons off Thermal Photons*; Physics Letters B, Vol. 249-1, 145 (1990).
- [40] H. Burkhardt; *Monte Carlo Simulation of Scattering of Beam Particles and Thermal Photons*; CERN SL/Note 93-73, 1993.
- [41] H. Burkhardt, P. Castro, R. Schmidt and G. von Holtey; *Protection of Bhabha Monitors from electron/positron Background*; CERN SL-MD Note 107, 1993.
- [42] G. von Holtey; *Proposal for an Interaction Rate Monitor at LEP*; LEP Note 462, 1983.
- [43] P. Castro; *Simulation studies for Bhabha Luminosity Detectors*; CERN SL/Note 92-28 (BI), 1992.
- [44] H. Burkhardt, private communication.
- [45] G. von Holtey; *Luminosity Monitoring at LEP2*; Proceedings of the 5th Workshop on LEP Performance, Ed. J. Poole, CERN SL/95-08(DI), 1995, pp. 174-178.
- [46] J.C. Gaborit; *Doses Intégrées sur le Calorimètre Bhabha en IP2 zone L3*; CERN RSR/SL/90-30, 1993.
- [47] J. Borer, C. Bovet, A. Burns and G. Morpurgo; *Harmonic Analysis of Coherent Bunch Oscillations In LEP*; Proceedings of the Third European Particle Accelerator Conference; Berlin, Germany, 1992, pp. 1082-1084.
- [48] J. Borer; *BOM system hardware status*; Proceedings of the Third Workshop on LEP Performance, CERN SL/93-19 (DI), Chamonix, 1993, pp. 219-231.

- [49] K.D. Lohmann, M. Placidi and H. Schmickler; *Design and Functionality of the LEP Q-meter*; Proceedings of the Second European Particle Accelerator Conference, Nice, France, 1990, pp. 774-776.
- [50] A. Burns; *BOM Software*; Proceedings of the Second Workshop on LEP Performance, Chamonix, 1992, pp. 95-101.
- [51] A. Burns, P. Castro, G. Morpurgo and R. Schmidt; *Betatron Function Measurement at LEP Using the BOM 1000 Turns Facility*; Proceedings of the 1993 IEEE Particle Accelerator Conference, Washington D.C., 1993, pp. 2103-2105.
- [52] P. Castro, W. Herr, M. Lamont and G. Roy; *Betatron Function Measurements at 45.6 GeV and β -beating Correction*; CERN SL-MD Note 147, 1994.
- [53] E. Keil; *Beating, RF asymmetries, sawtooth*; CERN SL-MD Note 14, 1992.
- [54] E. Keil; *Optics Imperfections*; Proceedings of the Third Workshop on LEP Performance, CERN SL/93-19 (DI), Chamonix, 1993, pp. 167-174.
- [55] P. Castro; *β -beating: How does it Affect LEP Performance?*; Proceedings of the Fourth Workshop on LEP Performance, CERN SL/94-6 (DI), Chamonix, 1994, pp. 269-287.
- [56] J. Camas et al.; *High Resolution Measurements of Lepton Beam Transverse Distributions with LEP Wire Scanners*; Proceedings of the 1993 IEEE Particle Accelerator Conference, Washington D.C., 1993, pp. 2504-2506.
- [57] G. Burtin et al.; *Performance and Operational Experience of the LEP Synchrotron Light Telescopes*; Proceedings of the 1993 IEEE Particle Accelerator Conference, Washington D.C., 1993, pp. 2495-2497.
- [58] H. Akbari et al.; *Measurement of Vertical Emittance at LEP from Hard X-Rays*; Proceedings of the 1993 IEEE Particle Accelerator Conference, Washington D.C., 1993, pp. 2492-2494.
- [59] E. Rossa, F. Tecker and J.C. Mathae; *Performance Limits of a Streak Camera in Real Time Three-dimensional Measurement of Bunch Oscillation in LEP*; Proceedings of the 1993 IEEE Particle Accelerator Conference, Washington D.C., 1993, pp. 2432-2434.
- [60] M. Mandakovic; *Improving the Consistency between Measured Beam Sizes and Luminosities in LEP via a Simple Theoretical Model*; CERN SL-MD Note 116, 1994.
- [61] K. B. Unser; *Design and preliminary tests of a beam intensity monitor for LEP*; Proceedings of the 1989 IEEE Particle Accelerator Conference. Chicago, USA, 1989.
- [62] P. Castro et al.; *Cross-Calibration of Emittance Measuring Instruments in LEP*; CERN SL-MD Note 202, 1996.
- [63] The LEP Energy Working Group; *LEP Center-of-Mass Energies in Presence of Opposite Sign Vertical Dispersion in Bunch-Train Operation*; LEP Energy Group/95-2, CERN SL-Note 85-77(BI). 1995.
- [64] D.Brandt, W.Herr, J.Miles, R.Schmidt; *A New Closed Orbit Correction Procedure for the CERN SPS and LEP*; Nuclear Instruments and Methods, A293 (1990), p. 305.

Acknowledgements

This work has been financially supported by the Ministerio Español de Educación y Ciencia through a Ph.D. fellowship (beca FPI) in the project of High Energy Particle Physics of the Instituto de Física Corpuscular de Valencia (IFIC) and the CERN administration through the Doctorate student program.

I am specially grateful to the two directors of my thesis Prof. Antonio Ferrer (University of Valencia) and Dr. Rüdiger Schmidt (CERN) for their friendly support, encouragement, constant interest in my work and many constructive discussions. I wish to acknowledge the leader of the SPS-LEP Division Dr. L. Evans and the leader of the Beam Instrumentation Group Dr. C. Bovet for giving me the opportunity to follow a research project at CERN.

I would like to thank for many useful suggestions, interesting discussions and ideas on my work as well as on the preparation of my thesis Dr. H. Burkhardt, Dr. A. Burns, Dr. C. Bovet, Dr. B. Dehning, Dr. W. Herr, Dr. A. Hofmann, Dr. G. von Holtey, Dr. J. Jowett, Dr. E. Keil, J. Klem, G. Morpurgo, Dr. M. Placidi, Dr. P. Puzo, I. Reichel, Dr. G. Roy, Dr. H. Schmickler, F. Tecker, Dr. A. Verdier, Dr. J. Wenninger and many other colleagues from the Beam Instrumentation, Accelerator Physics and Operations Groups of the SPS-LEP Division. Specially, I am grateful to G.P. Ferri for his friendly collaboration, for his explanations and his work in the luminosity monitors and electronics.

Finally, I would like to thank my parents Pedro and Loly, my sister Beatriz and my friend Andrea for their continuous support in my studies and encouragement.